7-24-2023

Twin-solute, twin-dislocation and twin-twin interactions in magnesium

Materials Yue

Jian Wang

Jian-Feng Nie

Available online at www.sciencedirect.com
ScienceDirect
Journal of Magnesium and Alloys xxx (xxxx) xxx
www.elsevier.com/locate/jma

Review

Twin-solute, twin-dislocation and twin-twin interactions in magnesium

Yuan Yue[a], Jian Wang[b], Jian-Feng Nie[a,*]

[a] Department of Materials Science and Engineering, Monash University, Victoria 3800, Australia
[b] Department of Mechanical & Materials Engineering, University of Nebraska-Lincoln, Lincoln, NE 68583, USA

Received 1 June 2023; received in revised form 22 July 2023; accepted 24 July 2023
Available online xxx

Abstract

Magnesium alloys have received considerable research interest due to their lightweight, high specific strength and excellent castability. However, their plastic deformation is more complicated compared to cubic materials, primarily because their low-symmetry hexagonal close-packed (hcp) crystal structure. Deformation twinning is a crucial plastic deformation mechanism in magnesium, and twins can affect the evolution of microstructure by interacting with other lattice defects, thereby affecting the mechanical properties. This paper provides a review of the interactions between deformation twins and lattice defects, such as solute atoms, dislocations and twins, in magnesium and its alloys. This review starts with interactions between twin boundaries and substitutional solutes like yttrium, zinc, silver, as well as interstitial solutes like hydrogen and oxygen. This is followed by twin-dislocation interactions, which mainly involve those between $\{10\bar{1}2\}$ tension or $\{10\bar{1}1\}$ compression twins and $\langle a \rangle$, $\langle c \rangle$ or $\langle c+a \rangle$ type dislocations. The following section examines twin-twin interactions, which occur either among the six variants of the same $\{10\bar{1}2\}$ or $\{10\bar{1}1\}$ twin, or between different types of twins. The resulting structures, including twin-twin junctions or boundaries, tension-tension double twin, and compression-tension double twin, are discussed in detail. Lastly, this review highlights the remaining research issues concerning the interactions between twins and lattice defects in magnesium, and provides suggestions for future work in this area.

Keywords: Magnesium alloys; Twin-solute interactions; Twin-dislocation interactions; Twin-twin interactions; Microstructure; Mechanical properties.

1. Introduction

Magnesium (Mg) has outstanding properties such as low density, high specific strength, great castability and excellent damping capacity. These make Mg alloys attractive for application in the automotive, aerospace and portable electronic devices industries [1–4]. However, due to the limited number of independent slip systems arising from its hexagonal-close-packed (hcp) structure, Mg has little ductility and poor formability at room temperature. As a consequence, twinning plays a crucial role in the plastic deformation of Mg and its alloys. The common twinning modes in Mg are $\{10\bar{1}2\}\langle\bar{1}011\rangle$, activated by tension along the c-axis of Mg crystal, $\{10\bar{1}1\}\langle\bar{1}012\rangle$ or $\{10\bar{1}3\}\langle\bar{3}032\rangle$, activated by compression along the c-axis of the Mg crystal, termed tension and compression twinning respectively. A twinning mode in an hcp structure is usually described by the following twinning elements: the invariant (twinning) plane K_1, the shear direction η_1, the undistorted (conjugate twinning) plane K_2, and the conjugate shear direction η_2 [5]. Table 1 provides the twinning elements for some specific twinning modes, with the twinning shear magnitude s expressed by the c/a (Λ) ratio. For the range of the c/a ratio observed in hcp metals ($1.5 < \Lambda < 1.9$), $\{10\bar{1}1\}$ and $\{11\bar{2}2\}$ twins are compression twins that can be activated by uniaxial compression along the c-axis of the hcp crystal, while $\{11\bar{2}1\}$ twin is a tension twin that can be activated by uniaxial tension along the c-axis of the crystal. $\{10\bar{1}2\}$ twin is a tension twin for Mg, Ti (titanium) and Zr (zirconium) that have $\Lambda < \sqrt{3}$, and a compression twin for Cd (cadmium) and Zn (zinc) having $\Lambda > \sqrt{3}$ [5–9]. Twins reported in Mg mainly include those with twin planes on $\{10\bar{1}2\}$, $\{10\bar{1}1\}$, $\{10\bar{1}3\}$,

* Corresponding author.
E-mail address: jianfeng.nie@monash.edu (J.-F. Nie).

https://doi.org/10.1016/j.jma.2023.07.015

Table 1
Twinning elements for some twinning modes in hcp structures [5].

K_1	K_2	η_1	η_2	s	Detected in metals
$\{10\bar{1}2\}$	$\{\bar{1}012\}$	$\langle 10\bar{1}\bar{1}\rangle$	$\langle\bar{1}01\bar{1}\rangle$	$(3-\Lambda^2)/\sqrt{3}\Lambda$	Mg, Ti, Co, Zr, Zn, Bi
$\{10\bar{1}1\}$	$\{10\bar{1}\bar{3}\}$	$\langle 10\bar{1}\bar{2}\rangle$	$\langle 30\bar{3}2\rangle$	$(4\Lambda^2-9)/4\sqrt{3}\Lambda$	Mg, Ti
$\{10\bar{1}\bar{3}\}$	$\{10\bar{1}1\}$	$\langle 30\bar{3}2\rangle$	$\langle 10\bar{1}2\rangle$	$(4\Lambda^2-9)/4\sqrt{3}\Lambda$	Mg
$\{11\bar{2}1\}$	$\{0002\}$	$\langle\bar{1}\bar{1}26\rangle$	$\langle 11\bar{2}0\rangle$	$1/\Lambda$	Ti, Zr, Co, Re
$\{11\bar{2}2\}$	$\{11\bar{2}\bar{4}\}$	$\langle 11\bar{2}\bar{3}\rangle$	$\langle 22\bar{4}3\rangle$	$2(\Lambda^2-2)/3\Lambda$	Ti, Zr
$\{11\bar{2}\bar{4}\}$	$\{11\bar{2}2\}$	$\langle 22\bar{4}3\rangle$	$\langle 11\bar{2}\bar{3}\rangle$	$2(\Lambda^2-2)/3\Lambda$	Ti, Zr

$\{10\bar{1}4\}$, $\{10\bar{1}5\}$ and $\{30\bar{3}4\}$, while other types of twins, such as $\{11\bar{2}1\}$, $\{11\bar{2}2\}$ and $\{11\bar{2}4\}$, generally occur in Ti and Zr [5,7-9]. The commonly detected twins in plastically deformed Mg are $\{10\bar{1}2\}$ tension twins, $\{10\bar{1}1\}$ or $\{10\bar{1}3\}$ compression twins, with the $\{10\bar{1}2\}$ tension twin being the most frequently observed. In addition, "double-twins" have been observed in plastically deformed Mg, which include $\{10\bar{1}1\}$-$\{10\bar{1}2\}$, $\{10\bar{1}3\}$-$\{10\bar{1}2\}$ and $\{10\bar{1}2\}$-$\{10\bar{1}2\}$ modes in which secondary $\{10\bar{1}2\}$ twins form inside the primary twin [10–13]. During plastic deformation, twins frequently interact with each other, and they also interact with slip dislocations and solute atoms. These twin-solute, twin-dislocation and twin-twin interactions impact the microstructure evolution during plastic deformation, and thus affect the mechanical properties.

Twin-solute interactions cause solute segregation in coherent twin boundaries (CTBs), and this behavior has been experimentally observed in Mg alloyed with rare-earth, Zn, Ag or Bi single or multiple elements [14–18]. The periodic segregation of solute atoms reduces the local strain at CTB and pin the twin boundary (TB) motion, causing the need for an increased stress level for twin boundary migration [14]. Previous studies made by DFT calculations [19] reported that solutes at CTBs resist the glide of twinning dislocations (TDs), and a larger stress is required for the further motion of the TDs, thus contributing to strengthening. Furthermore, some solutes such as Y, Zn, Ag, Mn are reported to enhance the cohesion of twin boundaries, resulting in improved fracture toughness [20–22].

Twin-dislocation interactions occur between different types of twins and different types of dislocations, including $\langle a \rangle$, $\langle c \rangle$ and $\langle c+a \rangle$ that can move on various slip planes such as basal, prismatic and pyramidal planes. This type of interactions affects the strain hardening behavior [23–26], in which TBs can act as obstacles to dislocation slip and pre-existing dislocations can impede the growth of twins [27,28]. In addition, dislocation transmutation [29–34]can occur across the twin boundary, in which glissile $\langle a \rangle$ dislocations transform to an immobile $\langle c+a \rangle$ that is in the form of two Frank partials bounding a basal I_1 stacking fault (SF) in between [31,32], and a sessile $\langle c \rangle$ or $\langle c+a \rangle$ dislocation can transform to two mobile $\langle a \rangle$ dislocations [35–37]. The transformation between immobile and mobile dislocations refreshes the plastic deformation capability, thus affecting the strength and ductility.

Twin-twin interactions can occur between any two of the six variants of the same type of twin or between different twin types. Twin-twin interactions result in structures such as twin-twin junctions (TTJs) [38–40], tension-tension double twin and compression-tension double twin. TTJs can retard the subsequent twinning by hindering the movement of TDs or retard the detwinning by impeding the dissociation of twin-twin boundary (TTB) dislocations [39], giving rise to strain hardening. In addition, TTJs can also facilitate the basal slip band transfer between two interacting twins when the two twins share the same zone axis [39,41]. Tension-tension double twin structures are effective in refining microstructure, which is beneficial to strength enhancement [42]. Compression-tension double twin structures produce localized shear, which is closely related to the crack initiation and propagation that causes fracture and failure [10,12,43-50].

The purpose of this article is to provide a comprehensive review of twin-solute, twin-dislocation and twin-twin interactions. The content includes the interaction behaviours and mechanisms, the corresponding products, and the influence of interactions on the mechanical properties of Mg and its alloys. Following the introduction, Section 2 provides a review of twin-solute interactions with solutes being either substitutional or interstitial. Section 3 reviews the interactions between twin and $\langle a \rangle$, $\langle c \rangle$ or $\langle c+a \rangle$ dislocation, with a focus on the $\{10\bar{1}2\}$ tension twins and $\{10\bar{1}1\}$ compression twins. Section 4 provides a review of twin-twin interactions that occur between $\{10\bar{1}2\}$ and $\{10\bar{1}2\}$, or $\{10\bar{1}1\}$ and $\{10\bar{1}1\}$ twin variants, which results in TTJs and TTBs. Double twin structures, with $\{10\bar{1}2\}$ secondary twin formed inside $\{10\bar{1}2\}$ or $\{10\bar{1}1\}$ primary twin, are discussed in detail. Other twinning modes such as sequential twinning are also briefly discussed. Section 5 provides a discussion on remaining critical issues that need to be solved for the interactions between twin and lattice defects in Mg, which is followed by a summary in Section 6.

2. Twin-solute interactions

2.1. Interactions between twin boundary and substitutional solutes

2.1.1. Solute segregation in coherent twin boundaries

Interactions between twin and substitutional solutes can result in segregation of solutes along CTBs. Solute atoms with atomic sizes different from that of Mg can replace Mg atoms on CTBs that have elastic strains that are distributed alternatingly on CTB extension and compression sites [14]. It

Please cite this article as: Y. Yue, J. Wang and J.-F. Nie, Twin-solute, twin-dislocation and twin-twin interactions in magnesium, Journal of Magnesium and Alloys, https://doi.org/10.1016/j.jma.2023.07.015

is now widely accepted that solute atoms with larger atomic radii than Mg tend to segregate to extension sites, while those with smaller atomic radii prefer to segregate to compression sites [14,19,51,52]. This segregation process occurs due to the minimization of elastic strain, whereby the relocation of a larger or smaller solute atom to the CTB can reduce strain in the lattice and simultaneously minimize strain in the CTB extension or compression sites.

The segregation of solute atoms on CTBs was first observed by Nie et al. [14] in Mg alloys that had undergone a given duration of annealing heat treatment. Gd-rich columns were found on the extension sites of $\{10\bar{1}1\}$, $\{10\bar{1}2\}$ or $\{10\bar{1}3\}$ CTBs in Mg-Gd binary alloys, while Zn atoms occupied the compression sites of the $\{10\bar{1}2\}$ CTBs in Mg-Zn binary alloys. For Mg-Gd-Zn ternary alloys, both Zn and Gd atoms were observed to occupy the extension site of the $\{10\bar{1}2\}$ CTBs. Similar segregation pattern on CTBs was subsequently reported in Mg alloys with either single or multiple alloying elements. Chen et al. [18] observed the segregation of Ag atoms on compression sites of $\{10\bar{1}1\}$, $\{10\bar{1}2\}$ and $\{10\bar{1}3\}$ CTBs in a Mg-Ag alloy, while Zhou et al. [15] showed significant segregation of Gd and Ag atoms on both $\{10\bar{1}1\}$ and $\{10\bar{1}2\}$ CTBs in Mg-Gd-Y-Ag alloy; Zhao et al. [17] observed the co-segregation of Nd and Ag atoms on both $\{10\bar{1}1\}$ and $\{10\bar{1}2\}$ CTBs in a Mg-Nd-Ag alloy, with Nd segregating to the extension sites and Ag to the compression sites, and He et al. [53] showed the segregation of Bi atoms on compression sites of $\{10\bar{1}1\}$ CTB in a Mg-Bi alloy. Apart from the above segregation patterns, some unique segregation patterns were also reported. For example, a spinal-shaped segregation structure on the $\{10\bar{1}2\}$ CTB was observed by Zhou et al. [15] in a Mg-Gd-Y-Ag alloy, in which Ag atoms are distributed uniformly between three Gd-rich columns. A mixture segregation pattern with Ag atoms segregated on two substitutional columns and one interstitial column at the $\{10\bar{1}3\}$ CTB was observed by Chen et al. [18] in Mg-Ag binary alloy. A double-segregation-layer with two mutually parallel $\{10\bar{1}1\}$ layers decorated by Gd-rich columns was observed by Zhu et al. [16] in Mg-Gd alloy.

The ability of solutes to segregate to CTBs is largely determined by their segregation energy (E_{seg}), which is the energy difference before and after the segregation in an alloy system. A more negative value of E_{seg} indicates a higher tendency for segregation [51]. According to previous DFT calculations [51,52,54,55], solutes such as Ag, Al, Ge, Ga, Li, Mn, Sn and Zn can be substituted into the compression site on CTBs due to their smaller size than Mg; while solutes such as Ca, Ce, Dy, Er, Gd, Ho, La, Lu, Nd, Pb, Pr, Sc, Sm, Y, Yb, Zr can segregate into the extension sites on CTBs since they are larger than Mg. In addition to the segregation energy, the solute-diffusion activation enthalpies (E_{Act}) need to be considered because solute atoms have to migrate to the twin boundaries before segregation can occur, as suggested by Zhang et al. [51]. A higher value of E_{Ac} means more energy is required in order to activate a diffusion process, making it more difficult for the solute to migrate to the CTBs. Therefore, only alloying elements with E_{Ac} equal to or lower than that of pure Mg, such as Ce, Dy, Gd, Li, Nd, Pb, Sm, Yb and Zn, are expected to migrate easily to the CTBs for the subsequent segregation process. Furthermore, Kumar et al. [52] suggested that a good solute for doping Mg should be soluble in both bulk and CTBs, with higher solubility in CTBs. For example, Ge, Zn, Ce and La are good candidates as they have high solubility in bulk and are more soluble in CTBs.

The criterion that attributes the negative segregation energy to elastic strain minimization has successfully explained most of the twin boundary segregation behaviours. However, it fails to explain the segregation phenomenon observed by He et al. [53]. In their work, Bi atoms, which have larger atomic size than Mg, segregate to the compression site of $\{10\bar{1}1\}$ and not to any type of site in $\{10\bar{1}2\}$, disobeying the conventional rule that larger solutes should occupy the extension site of CTBs. According to He et al. [53], although the segregation of Bi to the compression sites of $\{10\bar{1}1\}$ intensifies the local compression strain, a strong chemical bond between Bi and Mg atoms could effectively stabilize the CTBs and overcome the destabilizing effect from the increased strain field. In contrast, although the segregation of Bi to the extension sites of $\{10\bar{1}2\}$ can relieve strains, there is much less incentive to form a chemical bond between Mg and Bi on the twin boundary than that in the matrix. Neither local strain relief nor the formation of stronger chemical bonds can be achieved for the segregation of Bi to the compression sites of $\{10\bar{1}2\}$. These explanations rationalize the segregation behavior of Bi only to the compression sites of $\{10\bar{1}1\}$, and He et al. [53] further illustrated that elements with the same valence electron orbital type and similar electronegativity to Bi (such as Pb, Tl and In) also exhibit the same segregation manner. Therefore, the chemical bonding effect should be combined with elastic strain minimization to account for the negative values in the segregation energy, and this combination could give a more comprehensive understanding for solute segregation behavior on CTBs. It should be further noted that chemical bonding effect has a close relationship with the coordination geometry of the sites on CTBs, which is different for different types of sites (extension and compression) and for different types of CTBs [53]. For example, the geometry of the compression site in $\{10\bar{1}1\}$ CTBs suits solutes whose valence electrons occupy *p*-type orbitals (like Bi), while the geometry of the extension site in the $\{10\bar{1}1\}$ CTBs, or the geometry of the compression or extension site on other types of CTBs is not. However, regarding strain energy minimization, the segregation of solutes only relates to the types of the sites but is independent of the types of CTBs [22].

2.1.2. Effect of twin boundary segregation on mechanical properties of Mg

Periodic segregation of solutes on CTBs can significantly strengthen materials by pinning the migration of twin boundary. This phenomenon was first observed by Nie et al. [14], who found that samples with solute segregation on $\{10\bar{1}2\}$ CTBs exhibited limited twin growth and increased yield strength compared to identical samples without solute segregations. A subsequent study by Ghazisaeidi et al.

Please cite this article as: Y. Yue, J. Wang and J.-F. Nie, Twin-solute, twin-dislocation and twin-twin interactions in magnesium, Journal of Magnesium and Alloys, https://doi.org/10.1016/j.jma.2023.07.015

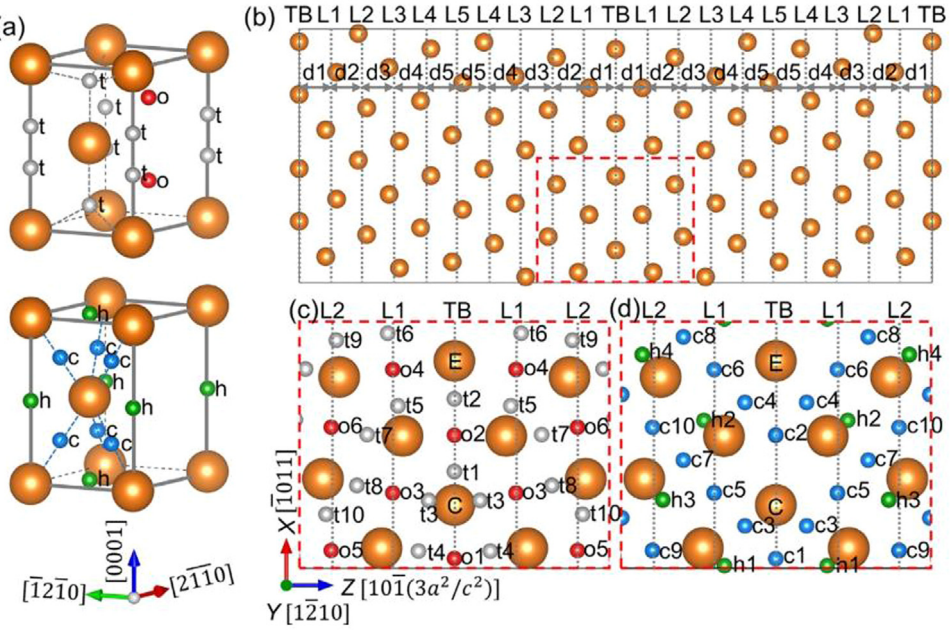

Fig. 1. (a) Possible interstitial sites for H atoms in a Mg unit cell. (b) Schematic illustration of the supercell of a {10$\bar{1}$2} twin boundary in Mg, with L1-L5 labelled the atomic planes from the plane closest to the TB to the plane in the bulk-like Mg region along the Z direction, and d1-d5 denoted the inter-planar spacings. (c and d) Enlarged views indicating the positions of the interstitial sites for H. Letters C and E denote the compression and extension sites in the TB plane. Letter t (gray), o (red), h (green), c (blue) denote the tetrahedral, octahedral, hexahedral, and crowdion interstitial sites for H, respectively, and numbers behind these letters increase with increasing the distance of the interstitial site away from the TB plane [55].

[19] used DFT calculations to examine the interactions between solutes and {10$\bar{1}$2} TDs and suggested that alloying elements could resist the glide of TDs, providing a significant contribution to strengthening (around 10 MPa) larger than the apparent "Peierls barrier" in pure Mg (around 3 MPa). Cui et al. [56] investigated the effect of annealing on the {10$\bar{1}$2} twin boundary mobility in different Mg alloys and found that longer annealing times or higher solute concentrations resulted in enhanced solute segregation on CTBs, leading to lower mobility of the twin boundary and stronger strengthening effect. Additionally, Wang et al. [57] also studied the relationship between solute concentration and strengthening effect and found that higher solute concentrations resulted in larger increase in the critical resolved shear stress for both the nucleation and growth of a {10$\bar{1}$2} twin.

The segregation of solutes on twin boundaries has been found to have a significant impact on the fracture toughness of Mg alloys. Somekawa et al. [58] reported that the frequent occurrence of dislocation pile-up on the {10$\bar{1}$2} twin boundaries could lead to strain accumulation, which could in turn cause the easy propagation of cracks along the twin boundaries. However, solute atoms such as Mn, Zn, Al, Ag can form strong adhesion with Mg atoms at the twin boundaries through either closed-shell (Mn and Zn) or covalent-like (Al and Ag) bonding. This impedes the crack propagation along the matrix-twin interface and results in high fracture toughness [20]. This enhancement of fracture toughness by solutes segregation on {10$\bar{1}$2} CTBs was also reported by Huang and Nie [55], who showed that the twin boundary cohesion is enhanced through the electronic interactions between solutes and Mg atoms. The most significant enhancement is observed when the solute atom is Zr, Mn or rate-earth element such as Y, La, Pr, Nd, Sm, Gd, Tb, Dy, Ho, and the enhancement is less significant for Al. On the other hand, Huang and Nie [55] also suggested that segregation of Li, Ca, Sn and Bi can reduce fracture toughness, as the weak Mg-solute interaction weakens the twin boundary cohesion.

Solute segregation on CTBs can also decrease the damping capacity of Mg alloys. It has been reported that an alternate shrinkage and growth of a deformation twin can effectively absorb the vibration energy and thus enhance damping capacity [59–62]. However, solute atoms that segregate to the twin boundaries, for example, Y on {10$\bar{1}$2} CTBs, could effectively stabilize the twin boundary and thus inhibit the shrinkage and growth of deformation twin, causing the loss of the damping capacity [21].

2.2. Interactions between twin boundary and interstitial solutes

Interstitial solutes such as hydrogen (H) and oxygen (O) can also interact with twin boundary. In a DFT study made by Huang et al. [55], segregation energy of H in tetrahedral, octahedral, hexahedral and crowdion sites were calculated. It was found that the segregation energy corresponding to a H atom located at one of the ten tetrahedral sites, which is on the {10$\bar{1}$2} twin boundary and labeled as t2 in Fig.1c, is much lower than that at any other site, indicating the preferable occupancy of H at a specific tetrahedral site of the twin

boundary rather than in the Mg matrix. Huang et al. [55] also investigated the interactions between H and solute atoms on the $\{10\bar{1}2\}$ twin boundary and found that Li, Ca, Mn, Zr, Y or Nd can promote H atoms to form solute-hydrogen clusters. The gathering of H atoms around a solute atom causes hydrogen embrittlement, which weakens the twin boundary and makes it susceptible to fracture. The weakening effect caused by Mn, Zr, Y or Nd is much more significant than that caused by Li or Ca.

Although interactions between interstitial O and the twin boundary in Mg have not been extensively studied, research conducted in Ti may provide some guidance. Ghazisaeidi and Trinkle [63] compared the energetics of four octahedral interstitial sites for O in the $\{10\bar{1}2\}$ twin geometry with that in the bulk and found that two of these sites, which were located at the twin boundary, were more attractive to O than the bulk and therefore likely to be occupied. Subsequent study conducted by Joost et al. [64] also showed the preferable occupancy of O atoms on two octahedral vacancies at the $\{10\bar{1}2\}$ twin boundary. They further demonstrated that the formation energies of the octahedral, hexahedral and crowdion O interstitials could be all modified by a nearby twin. Additionally, their work suggested that diffusion of O across the twin boundary was much easier than that in the bulk, which is consistent with that reported by Hooshmand et al. [65] Hooshmand and Ghazisaeidi [66] proposed that interaction between O and the $\{10\bar{1}2\}$ twin boundary could give rise to the dynamic strain aging effect based on serrated stress-strain curves obtained from tensile tests on single crystal Ti with O as the main interstitial content [67]. In this case, twin boundaries grow individually at a low plastic shear strain and are later pinned due to the fast diffusion of O atoms from the repulsive sites to the attractive sites within the twin boundary region. With the application of larger stress, the twin boundary grows faster until it is further pinned, and this process can manifest macroscopically as dynamic strain aging or serrated flow. The mechanism of dynamic strain aging caused by solute-twin interaction is also applicable to substitutional solutes, and the underlying features are the same as those for interstitial solutes.

3. Twin-dislocation interactions

The most commonly twinning mode in Mg is $\{10\bar{1}2\}\langle\bar{1}011\rangle$ extension and $\{10\bar{1}1\}\langle\bar{1}012\rangle$ contraction twinning, which cause misorientations of $\sim 86.3°$ and $\sim 56°$ between the basal planes of the parent and the twin around $\langle 1\bar{2}10\rangle$, respectively. According to the classical twinning theory, the growth of a twin involves lattice reorientation, which is equivalent to a simple shear, with the shear character carried by twinning dislocations or twinning disconnection (TDs) that glide along the twinning plane [5,68-70]. This process leads to a fully coherent twin boundary, i.e., K_1 plane, between the resultant twin and the parent crystal. An alternative growth mechanism for $\{10\bar{1}2\}$ twin was proposed by Li and Ma [71]. They suggested, based on their MD simulations, that $\{10\bar{1}2\}$ twin grew through pure atomic shuffling without the glide of TDs on the $\{10\bar{1}2\}$ twinning plane. This proposal stemmed from experimental observations of a deviation of the $\{10\bar{1}2\}$ twin boundary from the crystallographic twinning plane K_1 [72–75]. The actual misorientation angle between the basal planes of the parent and twin were found to range from 84° to 97°, differing from the theoretical value of 86.3°. However, this small inclination of the $\{10\bar{1}2\}$ twin boundary from the invariant K_1 plane can be ascribed to the coexistence of CTBs and basal-prismatic (BP, with the basal plane of the parent lying parallel or nearly parallel to the prismatic plane of the twin) or prismatic-basal (PB, with the prismatic plane of the parent lying parallel or nearly parallel to the basal plane of the twin) interfaces [76–78], where the BP/PB interfaces may arise from a pile-up of multiple TDs [78] or interactions between the CTBs and lattice dislocations [76]. While the simulation results of Li and Ma [71] contradict those of Wang et al. [76] and Ostapovets et al. [79], where the migration of the $\{10\bar{1}2\}$ twin boundary involves the glide of TDs on the $\{10\bar{1}2\}$ twin boundary, the difference between these results can be attributed to the different boundary conditions set in the simulations. Li and Ma applied free surface boundary, whereas Wang and Ostapovets et al. used periodic boundary condition along the twinning shear direction $\langle\bar{1}011\rangle$. In other words, the model of Li and Ma represents a nanoscale sample, while the models adopted by Wang and Ostapovets et al. represent a bulk sample. The in-situ TEM observation of twinning-like lattice reorientation in the work of Liu et al. [80] is consistent with nanoscale sample having free surfaces. A more detailed discussion can be found in [81–83]. The authors of this review paper adopted the same simulation setting as Ostapovets et al. [79] and observed that the twin growth occurred through nucleation and glide of TDs. Hence, it is concluded that the $\{10\bar{1}2\}$ twinning growth mechanism can be still accounted for by the classical TD theory, and that the existence of specific BP/PB segments within $\{10\bar{1}2\}$ CTBs accounts for the deviation of $\{10\bar{1}2\}$ TB from the theoretical twinning plane.

Macroscopically long BP/PB interface, composed of a large number of BP and PB segments with varying lengths, was experimentally observed in submicron-sized Mg single crystals compressed under a strain rate of $10^{-3}s^{-1}$ [80]. These macroscopic BP/PB interfaces cause a misorientation angle close to 90° between the parent and the "twin" region. There is no orientational mirror symmetry across such interfaces. The migration of the macroscopic BP/PB interface occurs through the nucleation and lateral gliding of interfacial defects on the coherent part of the interface that is defined by two adjacent misfit dislocations on the otherwise coherent BP/PB interface [80,84]. The motion of such interfacial defect changes the parent basal/prismatic to "twin" prismatic/basal and concomitantly gives rise to uniaxial deformation along the two orthogonal directions lying perpendicular and parallel to the *c*-axis of the parent. This process, named basal-prismatic "unit cell reconstruction", involves pure shuffling for the atomic rearrangement [80]. It is thus concluded that the migration of the macroscopic long BP/PB interface and the $\{10\bar{1}2\}$ CTB may occur through different mechanisms, leading to different

Please cite this article as: Y. Yue, J. Wang and J.-F. Nie, Twin-solute, twin-dislocation and twin-twin interactions in magnesium, Journal of Magnesium and Alloys, https://doi.org/10.1016/j.jma.2023.07.015

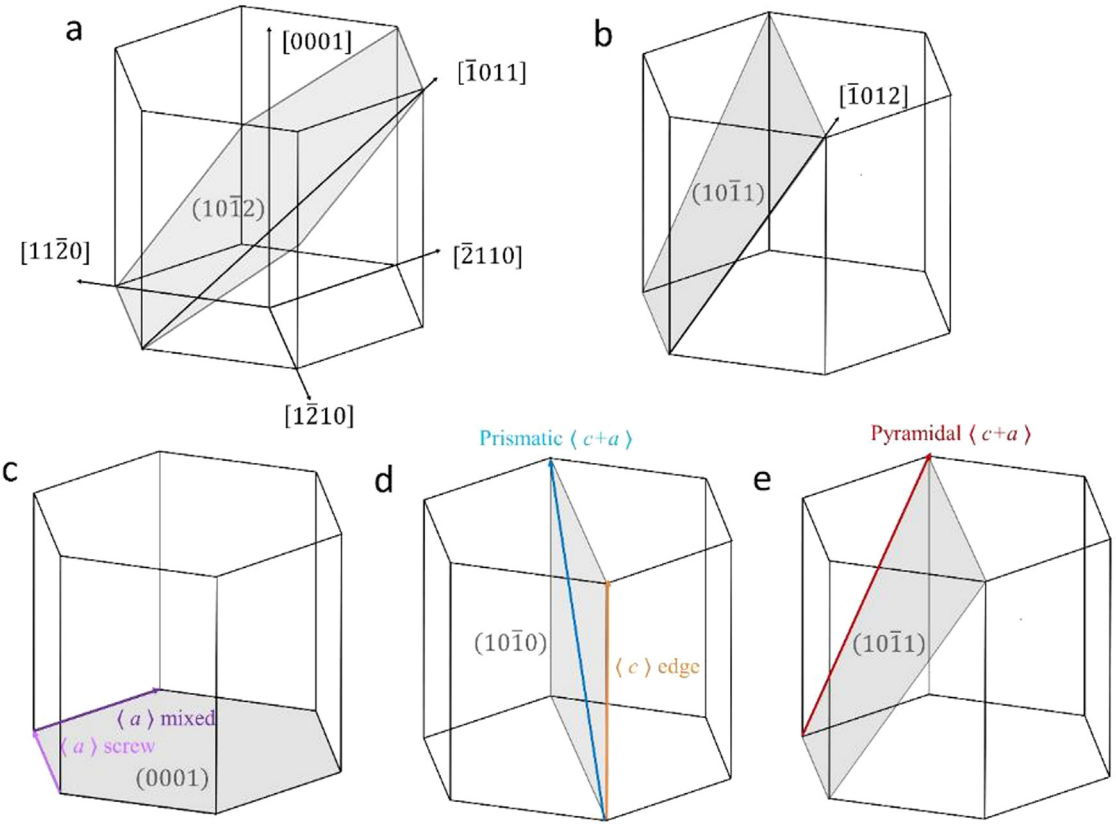

Fig. 2. Schematic illustration for (a) (10$\bar{1}$2)[$\bar{1}$011] extension twinning, (b) (10$\bar{1}$1)[$\bar{1}$012] contraction twinning, (c) (0001) basal ⟨ a ⟩ screw and mixed dislocations, (d) (10$\bar{1}$0) prismatic ⟨ c ⟩ edge and ⟨ $c+a$ ⟩ mixed dislocations, and (e) (10$\bar{1}$1) pyramidal ⟨ $c+a$ ⟩ mixed dislocation in Mg. The twin planes and dislocation slip planes are marked in gray color.

product orientations. This review paper only considers twin and dislocation interactions between CTBs and various lattice dislocations, and the growth mechanism of the {10$\bar{1}$2} twin is fully consistent with the classical theory of twinning. The {10$\bar{1}$2} extension and {10$\bar{1}$1} contraction twins are indexed as (10$\bar{1}$2) and (10$\bar{1}$1). They are viewed along the common axis [1$\bar{2}$10] of the matrix and twin, and shown in Figs. 2a and b, respectively.

⟨ a ⟩ type dislocations gliding on (0001) basal plane is called basal ⟨ a ⟩ dislocations. Basal ⟨ a ⟩ dislocation with Burgers vector of $\frac{1}{3}$[1$\bar{2}$10] that is parallel to the (10$\bar{1}$2) or (10$\bar{1}$1) twin plane, is called basal ⟨ a ⟩ screw dislocation. Basal ⟨ a ⟩ dislocation with Burgers vector of $\frac{1}{3}$[11$\bar{2}$0] or $\frac{1}{3}$[$\bar{2}$110] that is at 60° to the intersection line between the basal plane and twin plane, is called basal ⟨ a ⟩ mixed dislocation. ⟨ c ⟩ and ⟨ $c+a$ ⟩ dislocations focused on this work glide respectively on (10$\bar{1}$0) prismatic and (10$\bar{1}$1) pyramidal plane, these two planes share the common axis [1$\bar{2}$10] of the matrix and twin crystal. ⟨ c ⟩ dislocation with Burgers vector of [0001], is called prismatic ⟨ c ⟩ edge dislocation. ⟨ $c+a$ ⟩ dislocation with Burgers vector being the sum of basal ⟨ a ⟩ screw and prismatic ⟨ c ⟩ edge, or basal ⟨ a ⟩ mixed and prismatic ⟨ c ⟩ edge dislocations, is called prismatic or pyramidal ⟨ $c+a$ ⟩ mixed dislocation, respectively. Different types of dislocations and their glide planes are shown in Figs. 2c-e.

In the matrix crystal, basal ⟨ a ⟩ mixed dislocation $\frac{1}{3}[2\bar{1}\bar{1}0]_m$ or $\frac{1}{3}[\bar{2}110]_m$ (subscript m represent matrix), prismatic ⟨ c ⟩ edge dislocation $[0001]_m$ or $[000\bar{1}]_m$, prismatic ⟨ $c+a$ ⟩ mixed dislocation $\frac{1}{3}[\bar{1}2\bar{1}3]_m$ or $\frac{1}{3}[1\bar{2}\bar{1}3]_m$, and pyramidal ⟨ $c+a$ ⟩ dislocation $\frac{1}{3}[2\bar{1}\bar{1}3]_m$ or $\frac{1}{3}[\bar{2}11\bar{3}]_m$, is defined positive or negative, respectively. In the twin crystal, basal ⟨ a ⟩ mixed dislocation with an edge component of $\frac{1}{2}[10\bar{1}0]_t$ or $\frac{1}{2}[\bar{1}010]_t$, is defined positive or negative. A basal ⟨ a ⟩ mixed dislocation tends to dissociate into a 90° and a 30° Shockley partials bounding an I_2 basal SF in between, where 90° and 30° Shockley in the matrix or twin are designated $\mathbf{b}_\mathbf{m}^\mathbf{90}$ and $\mathbf{b}_\mathbf{m}^\mathbf{30}$ or $\mathbf{b}_\mathbf{t}^\mathbf{90}$ and $\mathbf{b}_\mathbf{t}^\mathbf{30}$, respectively. The ⟨ c ⟩ or ⟨ $c+a$ ⟩ type dislocation is inclined to dissociate into two $\frac{1}{2}$⟨ c ⟩ or two Frank partials, with an extrinsitc or I_1 basal SF bounding in between [85–87]. Dissociation of a positive or negative prismatic ⟨ $c+a$ ⟩ produces Frank partials of $\frac{1}{6}[\bar{2}203]_m$ and $\frac{1}{6}[02\bar{2}3]_m$, or $\frac{1}{6}[2\bar{2}0\bar{3}]_m$ and $\frac{1}{6}[0\bar{2}2\bar{3}]_m$. Dissociation of a positive or negative pyramidal ⟨ $c+a$ ⟩ produces Frank partials of $\frac{1}{6}[20\bar{2}3]_m$ and $\frac{1}{6}[02\bar{2}3]_m$, or $\frac{1}{6}[\bar{2}023]_m$ and $\frac{1}{6}[0\bar{2}2\bar{3}]_m$.

Disconnections on the (10$\bar{1}$2) or (10$\bar{1}$1) twin boundary are represented by $\mathbf{b}_{\pm\mathbf{p}/\pm\mathbf{q}}$ [88–94], where the superscript "+" or "-" indicates the step 'up' or 'down' with respect to the matrix, with "p" or "q" indicating the number of inter-planar spacing of the twinning planes corresponding to the step height in the matrix or twin. For a $\mathbf{b}_{\mathbf{1/1}}$ or $\mathbf{b}_{\mathbf{-1/-1}}$ single-atomic-layer-height (SALH) disconnection, it always connects with

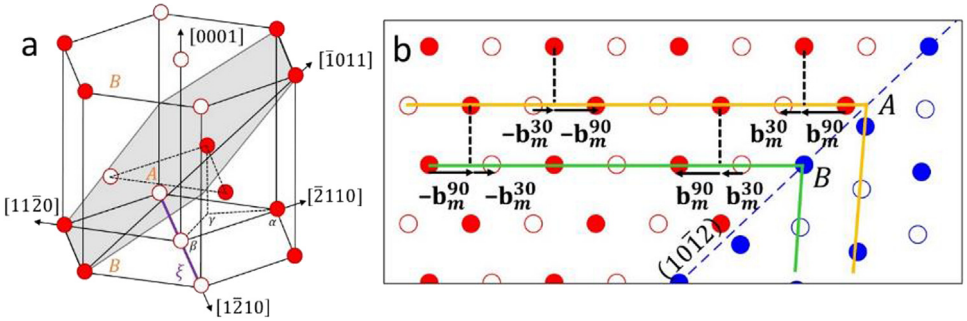

Fig. 3. (a) Schematic diagram showing Mg lattice comprising alternating basal planes A and B. Basal ⟨ *a* ⟩ mixed dislocation is defined as positive or negative when its Burgers vector is $\frac{1}{3}[2\bar{1}\bar{1}0]$ (***αβ***) or $\frac{1}{3}[\bar{2}110]$ (***βα***). (b) Dissociation of a basal ⟨ *a* ⟩ mixed dislocation in plane A (orange straight line) and in plane B (green straight line) leads to the 90° and 30° leading partial, respectively. Atoms in the matrix and twin lattices are indicated by red and blue circles, and their positions in two adjacent (1$\bar{2}$10) planes are indicated by solid and hollow circles, respectively.

an I_1 SF to produce a step-SF intersection, giving rise to a disconnection that can be designated $\mathbf{b}^{SF}_{1/1}$ or $\mathbf{b}^{SF}_{-1/-1}$. Notation of $\mathbf{b}_{\pm p/\pm q}$ can also represent the lattice dislocation [92,93], with q or p equal to zero for a dislocation in the matrix or twin. It should be noted that screw component along [1$\bar{2}$10] is not represented in this notation, and has q or p always equal to zero. As a result, basal ⟨ *a* ⟩ screw dislocation is represented as $\mathbf{b}_{0/0}$. Positive or negative basal ⟨ *a* ⟩ mixed dislocation is designated $\mathbf{b}_{1/0}$ or $\mathbf{b}_{-1/0}$ in the matrix, and $\mathbf{b}_{0/1}$ and $\mathbf{b}_{0/-1}$ in the twin. Matrix prismatic ⟨ *c* ⟩ or ⟨ *c* + *a* ⟩ dislocation is desigated $\mathbf{b}_{2/0}$ or $\mathbf{b}_{-2/0}$, and matrix pyramidal ⟨ *c* + *a* ⟩ mixed dislocation is desigated $\mathbf{b}_{3/0}$ or $\mathbf{b}_{-3/0}$.

3.1. Interaction between {10$\bar{1}$2} *extension twin and different types of dislocations*

3.1.1. {10$\bar{1}$2} *extension twin and* ⟨ *a* ⟩ *type dislocations*

3.1.1.1. Interaction with basal ⟨ *a* ⟩ *screw dislocation*

.

Previous studies in Mg [95–100] suggests that a basal ⟨ *a* ⟩ screw dislocation that has a Burgers vector parallel to the (10$\bar{1}$2) twin plane can directly transmit across the twin boundary. This process involves the cross slip of the dislocation from the basal plane in the matrix onto the basal or prismatic plane in the twin, and no residual dislocations are left in the boundary. Similar interaction behavior has been reported in titanium (Ti) [97], zirconium (Zr) [101] and zinc (Zn) [102,103].

3.1.1.2. Interaction with basal ⟨ *a* ⟩ *mixed dislocation*

.

Computational simulations conducted on Mg suggested that a basal ⟨ *a* ⟩ mixed dislocation gliding onto the (10$\bar{1}$2) twin boundary will be absorbed by the twin boundary, modifying the initially flat coherent twin boundary by forming a basal-prismatic (BP, with the basal plane of the matrix parallel to the prismatic plane of the twin) or prismatic-basal (PB, with the prismatic plane of the matrix parallel to the basal plane of the twin) disconnection of a relatively large height, with simultaneous emission of two-atomic-layer-height TDs [100,104-107]. Such absorption was also observed in simulations in Ti [69,92] and Zr [93]. Apart from being absorbed by the twin boundary, a matrix basal ⟨ *a* ⟩ mixed dislocation can transmute across the (10$\bar{1}$2) twin boundary. The concept of the transmutation refers to the change of slip plane and the Burgers vector of a dislocation when incorporate into the twin. Based on the crystallographic analysis, a Burgers vector of a basal ⟨ *a* ⟩ mixed dislocation in the matrix corresponds to the Burgers vector of a $\frac{1}{2}$⟨ *c* + *a* ⟩ dislocation in the twin, thus a unit ⟨ *c* + *a* ⟩ dislocation is possibly produced by incorporting two ⟨ *a* ⟩ dislocations [108,109]. Such transmutation reaction was confirmed in the molecular dynamics (MD) simulation conducted by Wang et al. [31], in which an ⟨ *a* ⟩ dislocation transmuted into a Frank partial dislocation inside the twin and a SALH disconnection on the twin boundary, with an I_1 SF linking them. Wang et al. [32] further proposed that two basal ⟨ *a* ⟩ mixed dislocations can transmute into a pair of Frank partial dislocations, and these two partials have a total Burgers vector equal to that of a prismatic ⟨ *c* + *a* ⟩ dislocation. Transmutation of matrix basal ⟨ *a* ⟩ dislocations was also observed in the MD simulation conducted by Barrett et al. [29], in which a prismatic ⟨ *c* + *a* ⟩ dislocation was produced after two ⟨ *a* ⟩ dislocations crossed a (10$\bar{1}$2) twin boundary.

The different interaction products are thought to be related to the loading condition and the geometric relationship between the (10$\bar{1}$2) twin and basal ⟨ *a* ⟩ mixed dislocations. Here the geometric relationship refers to the sign of the dislocation (the Burges vector direction of the dislocation with respect to the twinning shear direction), the positions of the two Shockley partials (resulting from dissociation of the ⟨ *a* ⟩ dislocation) relative to the twin boundary, and the type of the intersection point (extension or compression site) between the twin boundary and the slip plane of the ⟨ *a* ⟩ dislocation. Based on crystallographic analysis, an ⟨ *a* ⟩ dissociating in the plane A or B that intersects at the extension or compression site of the (10$\bar{1}$2) twin boundary, must have 90° or 30° Shockley leading partial, irrespective of its sign, as illustrated in Fig. 3. The interaction between (10$\bar{1}$2) twin and basal ⟨ *a* ⟩ mixed

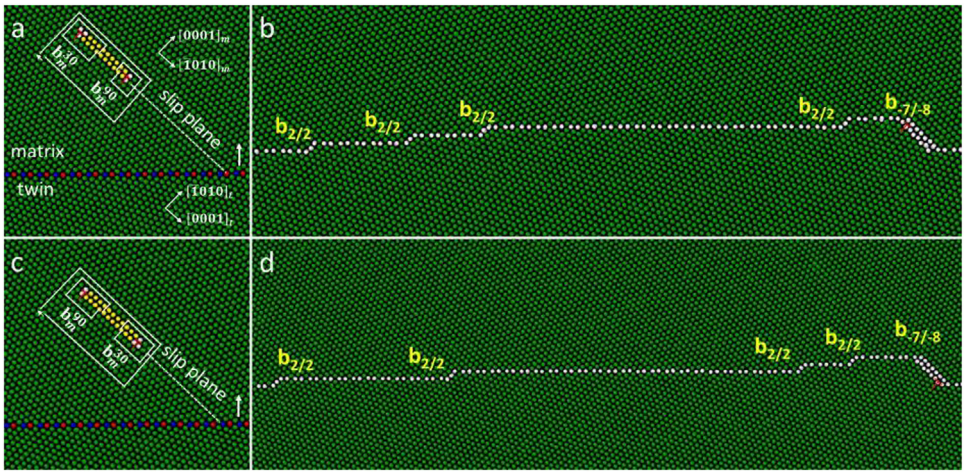

Fig. 4. Interaction between a positive basal ⟨ *a* ⟩ mixed dislocation $\mathbf{b_{1/0}}$ and a $(10\bar{1}2)$ twin under 200 MPa shear stress along $[\bar{1}011]$ at 300 K, showing full absorption of $\mathbf{b_{1/0}}$, irrespective of the types of leading partials, which results in the formation of a BP $\mathbf{b_{-7/-8}}$ disconnection and four $\mathbf{b_{2/2}}$ s. (a-b) $\mathbf{b_{1/0}}$ with $\mathbf{b_m^{90}}$ leading partial. (c-d) $\mathbf{b_{1/0}}$ with $\mathbf{b_m^{30}}$ leading partial. Atoms located at tension and compression sites of the twin boundary at (a, c) are coloured in red and blue, respectively. In (a, c), the slip plane of ⟨ *a* ⟩ is indicated by white dashed line, and the migration direction of the twin boundary is indicated by white arrow.

dislocations under different conditions are shown in detail as following.

• *Positive ⟨ a ⟩ mixed dislocation*

The interaction process between a positive basal ⟨ *a* ⟩ mixed dislocation $\mathbf{b_{1/0}}$ and a $(10\bar{1}2)$ twin boundary is shown in Fig. 4, with $\mathbf{b_{1/0}}$ having $\mathbf{b_m^{90}}$ (Figs. 4a and b) or $\mathbf{b_m^{30}}$ (Figs. 4c and d) as the leading partial. In both cases, the applied shear stress is 200 MPa along $[\bar{1}011]$, and $\mathbf{b_{1/0}}$ is fully absorbed by the twin boundary. The absorption of $\mathbf{b_{1/0}}$ results in a $\mathbf{b_{-7/-8}}$ disconnection and four $\mathbf{b_{2/2}}$ TDs. The riser plane of the $\mathbf{b_{-7/-8}}$ is parallel to the BP interface. The decomposition of a positive basal ⟨ *a* ⟩ mixed dislocation can be described by the equation developed by Serra et al. [69], which is

$$\mathbf{b_{1/0}} = \mathbf{b_{-(2n-1)/-2n}} + n\mathbf{b_{2/2}} \tag{1}$$

When the shear stress is increased to 700–800 MPa, transmutation of $\mathbf{b_{1/0}}$ occurs. The transmutation of $\mathbf{b_{1/0}}$, either with $\mathbf{b_m^{90}}$ or $\mathbf{b_m^{30}}$ leading partial, produces a Frank partial dislocation inside the twin and a SALH disconnection on the twin boundary, with an I_1 fault in between, Figs. 5c and d. This reaction can be described by

$$\mathbf{b_{1/0}} = \mathbf{b_{1/1}^{SF}} + \frac{1}{6}\left[2\bar{2}0\bar{3}\right]_t \tag{2}$$

or

$$\mathbf{b_{1/0}} = \mathbf{b_{-2/-2}} + \frac{1}{6}\left[0\bar{2}2\bar{3}\right]_t + \mathbf{b_{-1/-1}^{SF}} \tag{3}$$

as illustrated in Figs. 5e or f, respectively.

• *Negative ⟨ a ⟩ mixed dislocation*

The interaction between a negative basal ⟨ *a* ⟩ mixed dislocation $\mathbf{b_{-1/0}}$ with $-\mathbf{b_m^{90}}$ leading partial and a $(10\bar{1}2)$ twin boundary under a shear stress of 200 MPa along $[\bar{1}011]$, causes $\mathbf{b_{-1/0}}$ to connect with a $\mathbf{b_{2/2}}$ disconnection on the $(10\bar{1}2)$ twin boundary through $-\mathbf{b_m^{90}}$, with $-\mathbf{b_m^{30}}$ separated from the twin boundary by an I_2 fault, and this process is accompanied with the emission of a $\mathbf{b_{-2/-2}}$ TD, Figs. 6a-b. The riser plane of the $\mathbf{b_{2/2}}$ that connects with the $-\mathbf{b_m^{90}}$, is parallel to the PB interface. This reaction can be described by the equation following Serra et al. [69], which is

$$\mathbf{b_{-1/0}} = -\mathbf{b_m^{30}} + \left(-\mathbf{b_m^{90}} + \mathbf{b_{2n/2n}}\right) + n\mathbf{b_{-2/-2}} \tag{4}$$

Under the same shear stress of 200 MPa, a $\mathbf{b_{-1/0}}$ with $-\mathbf{b_m^{30}}$ leading partial cannot interact with a $(10\bar{1}2)$ twin boundary. This dislocation, when gliding towards and tending to contact with the twin boundary, is always repelled back by the twin boundary, Figs. 6c-d.

Transmutation of $\mathbf{b_{-1/0}}$ with $-\mathbf{b_m^{90}}$ leading partial occurs when the shear stress is increased to around 800 MPa. And transmutation of $\mathbf{b_{-1/0}}$ with $-\mathbf{b_m^{30}}$ leading partial is observed when the shear stress is larger than 470 MPa. The transmutation of $\mathbf{b_{-1/0}}$, either with $-\mathbf{b_m^{90}}$ or $-\mathbf{b_m^{30}}$ leading partial, generates a Frank partial dislocation inside the twin and a SALH disconnection on the twin boundary, with an I_1 fault in between, Figs. 7c and d. This reaction can be described by

$$\mathbf{b_{-1/0}} = \mathbf{b_{1/1}^{SF}} + \frac{1}{6}\left[0\bar{2}\bar{2}3\right]_t + \mathbf{b_{2/2}} \tag{5}$$

or

$$\mathbf{b_{-1/0}} = \mathbf{b_{-1/-1}^{SF}} + \frac{1}{6}\left[\bar{2}203\right]_t \tag{6}$$

as illustrated in Figs. 7e or f, respectively.

Please cite this article as: Y. Yue, J. Wang and J.-F. Nie, Twin-solute, twin-dislocation and twin-twin interactions in magnesium, Journal of Magnesium and Alloys, https://doi.org/10.1016/j.jma.2023.07.015

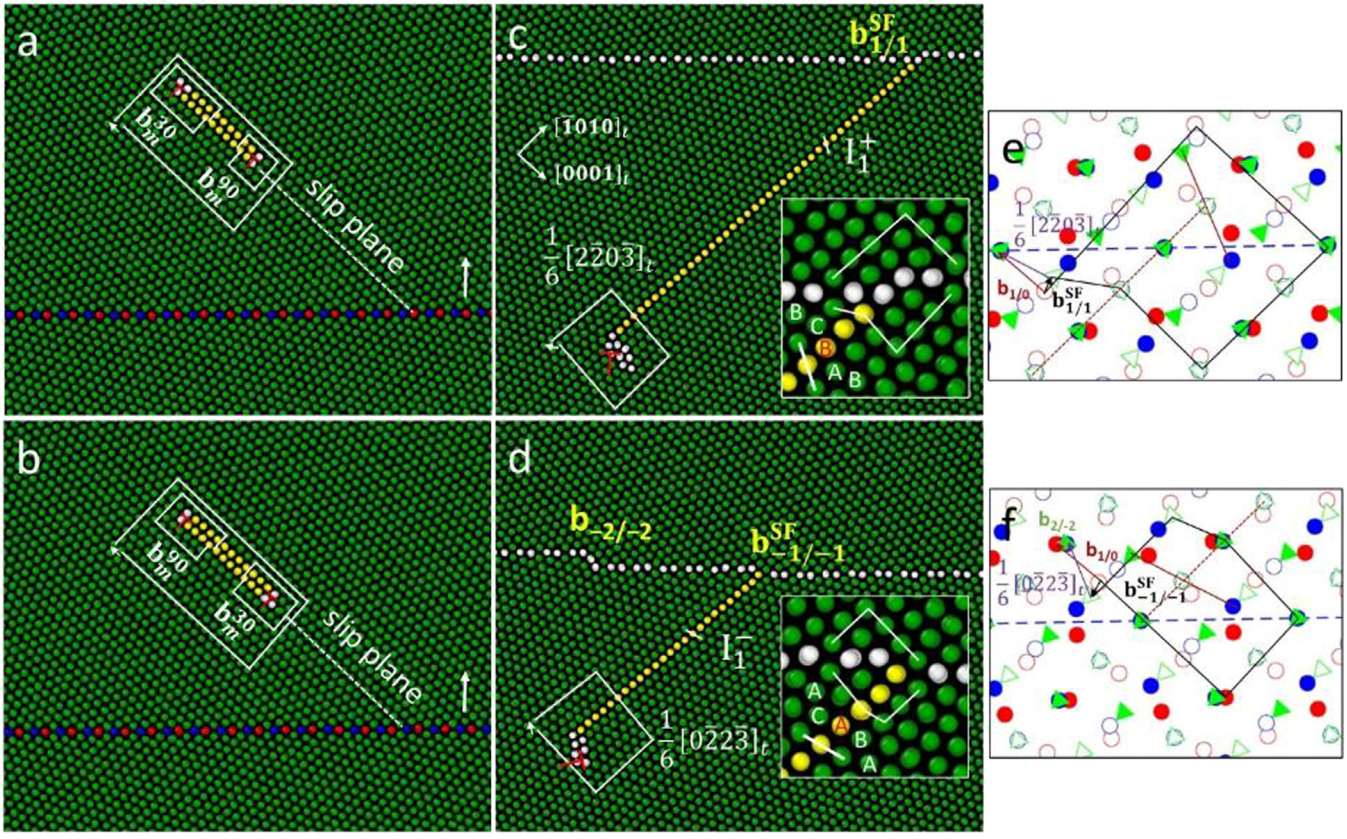

Fig. 5. Interaction between $\mathbf{b_{1/0}}$ and a $(10\bar{1}2)$ twin under a shear stress of 700 MPa along $[\bar{1}011]$ at 300 K in (a) or (b) gives rise to (c) a $\mathbf{b}_{1/1}^{SF}$ disconnection and $\frac{1}{6}[2\bar{2}0\bar{3}]_t$ Frank partial dislocation with an I_1^+ fault in between or (d) a $\mathbf{b}_{-1/-1}^{SF}$ disconnection and $\frac{1}{6}[0\bar{2}2\bar{3}]_t$Frank partial dislocation with an I_1^- fault in between, together with a $\mathbf{b_{-2/-2}}$ TD. Burgers vectors of the $\mathbf{b_{1/1}}$ and $\mathbf{b_{-1/-1}}$ are determined by reproducing the circuits in the insert of (c) and (d) in the trichromatic complex in (e) and (f). respectively. Relationship among Burgers vectors of lattice dislocations and disconnections on the twin boundary for the reaction of (a or b-c) and (a or b-d) are illustrated in (e) and (f) respectively. In the trichromatic complex, the red, blue, and green lattices represent respectively matrix, twin and the crystal having same orientation as the twin crystal, but with the stacking sequence changed by the I_1 fault. In symbol $I_1^{+(-)}$, the superscript "+" or "-" indicates the shear direction $[10\bar{1}0]_t$ or $[\bar{1}010]_t$ that generates the I_1 fault in the twin lattice.

• *Interaction with two ⟨ a ⟩ mixed dislocations*

When Eqs. (2) and (3) are added together, there is

$$2\mathbf{b_{1/0}} = \frac{1}{6}[2\bar{2}0\bar{3}]_t + \frac{1}{6}[0\bar{2}2\bar{3}]_t + \mathbf{b_{-2/-2}} = \frac{1}{3}[1\bar{2}1\bar{3}]_t + \mathbf{b_{-2/-2}} \quad (7)$$

and combination of Eqs. (5) and (6) leads to

$$2\mathbf{b_{-1/0}} = \frac{1}{6}[02\bar{2}3]_t + \frac{1}{6}[\bar{2}203]_t + \mathbf{b_{2/2}} = \frac{1}{3}[\bar{1}2\bar{1}3]_t + \mathbf{b_{2/2}} \quad (8)$$

This means that transmutation of two same-signed basal ⟨ *a* ⟩ mixed dislocations can produce conjugate Frank partials that have a sum of Burgers vector equal to a prismatic ⟨ $c + a$ ⟩ dislocation. Such a process is verified in the present MD simulation. As shown in Fig. 8, transmutation of the first $\mathbf{b_{-1/0}}$ has produced an I_1 fault connected with a $\mathbf{b}_{1/1}^{SF}$ and bounded by a $\frac{1}{6}[02\bar{2}3]_t$. When the second $\mathbf{b_{-1/0}}$ glides towards and transmutes at the intersection point between the twin boundary and the I_1 fault, the I_1 detaches from the twin boundary and bounded by $\frac{1}{6}[02\bar{2}3]_t$ and $\frac{1}{6}[\bar{2}203]_t$ Frank partials at its two ends, leaving behind a $\mathbf{b_{2/2}}$ TD on the twin boundary.

3.1.1.3. Twin boundary migration after twin and ⟨ a ⟩ dislocation interactions.

Interaction between a twin and a basal ⟨ *a* ⟩ screw dislocation does not change the configuration of the twin boundary. Such interaction would not affect the migration of the twin boundary as no TDs are involved and the ⟨ *a* ⟩ simply cross-slips [98,99,102].

Absorption of a positive basal ⟨ *a* ⟩ mixed dislocation produces a BP $\mathbf{b_{-(2n-1)/-2n}}$ disconnection on the otherwise planer twin boundary and $n\mathbf{b_{2/2}}$ TDs. Migration of a BP $\mathbf{b_{-(2n-1)/-2n}}$ disconnection was first investigated by Serra and Bacon [69]. As shown in their simulations, a pair of TDs with opposite sign will be nucleated at each end of the BP riser under applied shear stress, these TDs move in opposite directions and cause the BP disconnection to migrate along the BP riser plane. The essence of this process was subsequently suggested by Pond et al. [89] to be equivalent to the interactive motion of a TD from one side to the other side of the BP riser, which was called compensated climb. This process was recently confirmed as disconnection transformation by El Kadiri and co-workers [106]. The description is: a TD nucleated at or gliding onto one end of the BP riser becomes a part of the

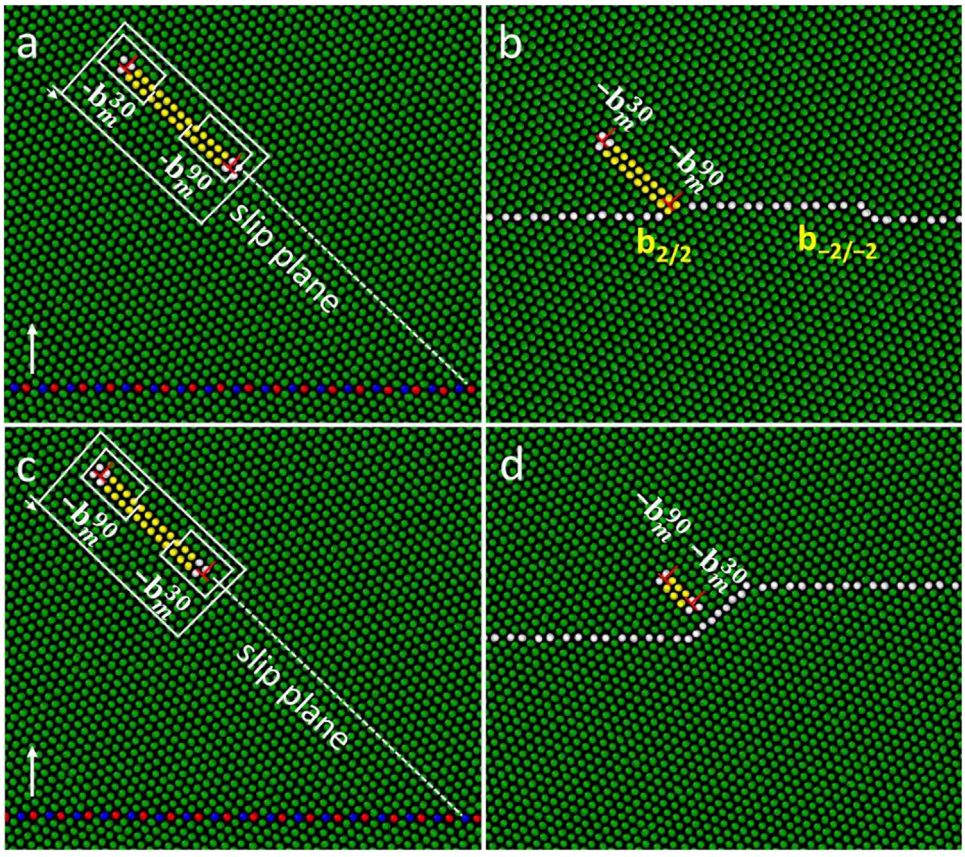

Fig. 6. (a-b) Interaction between a negative basal ⟨ *a* ⟩ mixed dislocation $\mathbf{b}_{-1/0}$ with $-\mathbf{b}_m^{90}$ leading partial and a $(10\bar{1}2)$ twin under a shear stress of 200 MPa along $[\bar{1}011]$ at 300 K, causes the $\mathbf{b}_{-1/0}$ to connect to a PB $\mathbf{b}_{2/2}$ disconnection on the twin boundary through the $-\mathbf{b}_m^{90}$, with the $-\mathbf{b}_m^{30}$ trailing partial separated from the twin boundary by the I_2 fault, accompanied with the emission of a $\mathbf{b}_{-2/-2}$ TD. (c-d) A $\mathbf{b}_{-1/0}$ with $-\mathbf{b}_m^{30}$ leading partial is repelled by the $(10\bar{1}2)$ twin boundary under a shear stress of 200 MPa at 300 K.

riser, then another specific part of the BP riser transforms to a same-signed TD that glides away from the other end of the riser. The disappearance-reappearance of TDs permits the BP disconnection to move along the riser plane in a cooperative manner.

A negative basal ⟨ *a* ⟩ mixed dislocation can connect to a PB $\mathbf{b}_{2n/2n}$ disconnection on the twin boundary, accompanied with the formation of $n\mathbf{b}_{-2/-2}$ TDs. Such a PB $\mathbf{b}_{2n/2n}$ disconnection migrates when a TD glides across the PB riser, together with the migration of the connected ⟨ *a* ⟩ dislocation. The migration direction of the PB disconnection is parallel to the basal glide plane of the ⟨ *a* ⟩ dislocation, and is normal to the PB riser plane [69].

Transmutation of either a positive or negative basal ⟨ *a* ⟩ mixed dislocation occurs under a stress state larger than that for absorption or connection of a same dislocation. The transmutation reaction generates either a BP $\mathbf{b}^{SF}_{-1/-1}$ or PB $\mathbf{b}^{SF}_{1/1}$ disconnection that connects with an I_1 fault. Such disconnection is reported to be sessile [110,111]. It was shown in a recent MD work [111] that a BP $\mathbf{b}^{SF}_{-1/-1}$ disconnection has its position changed only along the normal direction of the BP riser plane, while a PB $\mathbf{b}^{SF}_{1/1}$ disconnection has its position changed only along the PB riser plane.

3.1.2. Interaction with ⟨ *c* ⟩ or ⟨ *c* + *a* ⟩ type dislocations

3.1.2.1. Interaction with prismatic ⟨ *c* ⟩ edge dislocation.

Theoretical analysis [35,36] based on the crystallographic relationship between the matrix and a $(10\bar{1}2)$ twin, suggests that the interaction between the twin and a matrix prismatic ⟨ *c* ⟩ edge dislocation can produce two basal ⟨ *a* ⟩ mixed dislocations in the twin crystal. This was confirmed by a recent MD simulation [37], Fig. 9, which showed that interaction between the twin and each of the $\frac{1}{2}$⟨ *c* ⟩ partial of a ⟨ *c* ⟩ dislocation produced a basal ⟨ *a* ⟩ mixed dislocation under sole shear stress along $[\bar{1}011]$. The transmutation of a matrix ⟨ *c* ⟩ to two ⟨ *a* ⟩ dislocations in the twin could be described by

$$\mathbf{b}_{-2/0} = 2\mathbf{b}_{0/1} + \mathbf{b}_{-2/-2} \tag{9}$$

or

$$\mathbf{b}_{2/0} = 2\mathbf{b}_{0/-1} + \mathbf{b}_{2/2} \tag{10}$$

The resultant ⟨ *a* ⟩ dislocation tends to connect with the twin boundary when its 90° Shockley located at the end close to the twin boundary, giving a configuration comprising an interfacial defect connecting an I_2 fault that is bounded by a 30° Shockley inside the twin, under a low shear stress along

Please cite this article as: Y. Yue, J. Wang and J.-F. Nie, Twin-solute, twin-dislocation and twin-twin interactions in magnesium, Journal of Magnesium and Alloys, https://doi.org/10.1016/j.jma.2023.07.015

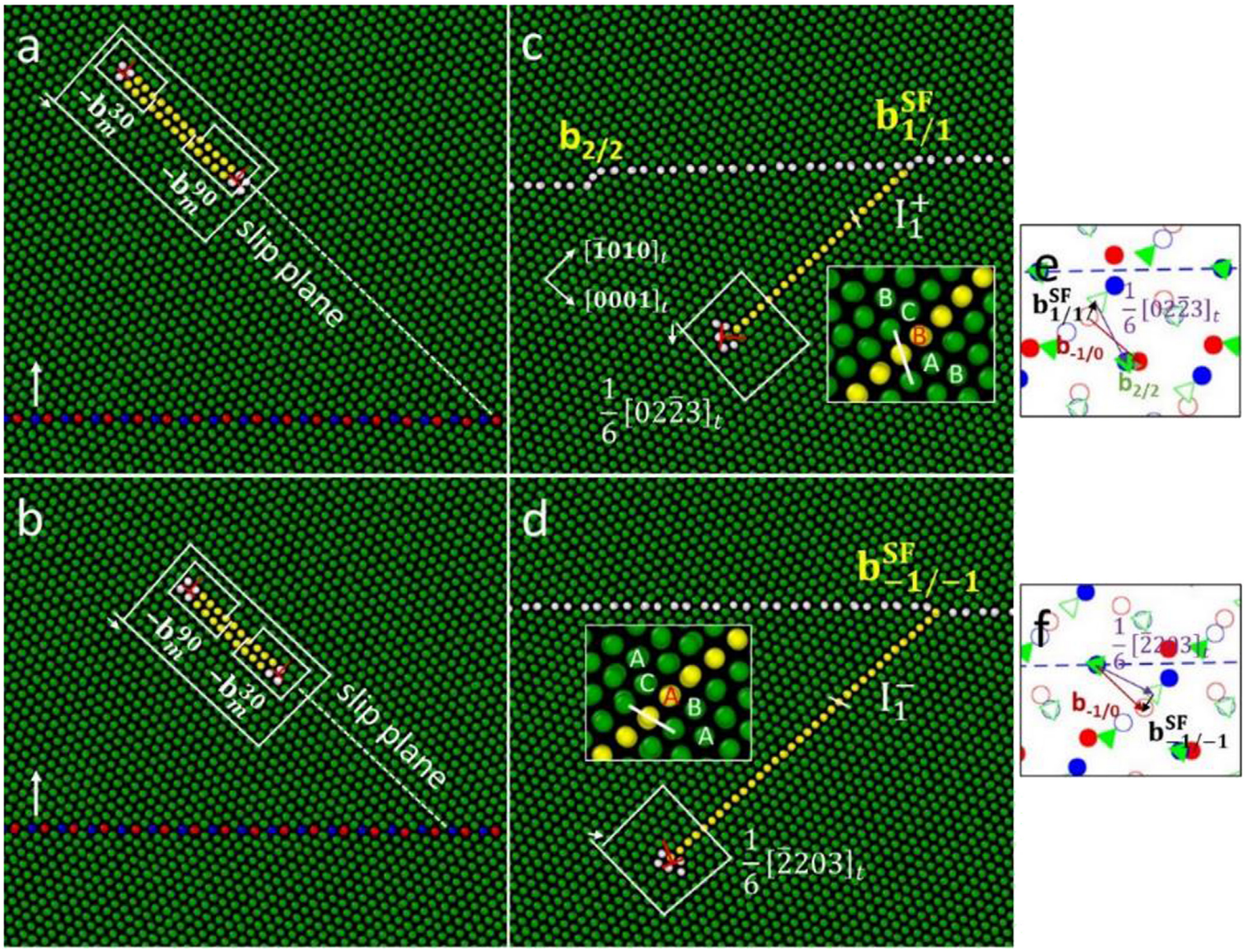

Fig. 7. Interaction between $\mathbf{b}_{-1/0}$ and a $(10\bar{1}2)$ twin in (a) or (b) produces a $\mathbf{b}_{1/1}^{SF}$ disconnection and $\frac{1}{6}[02\bar{2}3]_t$ Frank partial dislocation with an I_1^+ fault in between, together with a $\mathbf{b}_{2/2}$ TD or (c) a $\mathbf{b}_{-1/-1}^{SF}$ disconnection and $\frac{1}{6}[\bar{2}203]_t$ Frank partial dislocation with an I_1^- fault in between. The configurations in (c) and (d) are obtained under a shear stress of 800 MPa and 470 MPa along $[\bar{1}011]$,respectively, at 300 K. Relationship among Burgers vectors of lattice dislocations and disconnections on the twin boundary for reaction of (a or b-c) and (a or b-d) are illustrated in (e) and (f).

$[\bar{1}011]$. This interfacical defect can be BP $\mathbf{b}_{-2n/-2n}$ or PB $\mathbf{b}_{2n/2n}$ when the connected "$\langle a \rangle$" has a positve or negative sign [37]. For example, as shown in Fig. 10, two I_2 fault both connected with the twin boundary can be produced from the twin and a $\langle c \rangle$ dislocation interaction under a shear stress of 200 MPa, with such reaction described by

$$\mathbf{b}_{-2/0} = 2\mathbf{b}_t^{30} + 2\left(\mathbf{b}_t^{90} + \mathbf{b}_{-2n/-2n}\right) + (2n-1)\mathbf{b}_{2/2} \tag{11}$$

or

$$\mathbf{b}_{2/0} = 2\left(-\mathbf{b}_t^{30}\right) + 2\left(-\mathbf{b}_t^{90} + \mathbf{b}_{2n/2n}\right) + (2n-1)\mathbf{b}_{-2/-2}. \tag{12}$$

The I_2 fault that connects with the interfacial defect tends to detach from the twin boundary under a high shear stress (~1.5 GPa) [37] or under simultaneous application of shear and tensile stresses [112], giving rise to a glissle $\langle a \rangle$ dislocation in the twin crystal.

Apart from producing a positive basal $\langle a \rangle$ mixed dislocation, a negative $\frac{1}{2}\langle c \rangle$ dislocation can also give rise to an unusual structure after its interaction with the $(10\bar{1}2)$ twin under sole shear stress. The unusual structure comprises two I_1 faults that are separated by two basal layers, which has been briefly introduced in a previous DFT work [113] and designated F_3 fault. The two I_1 of a F_3 fault have their upper ends connected to two separate BP $\mathbf{b}_{-1/-1}^{SF}$ disconnections and their lower ends bounded by a complex defect inside twin, and this complex defect has a Burgers vector identical to that of a $\mathbf{b}^{30}$ Shockley partial dislocation, Fig. 11b. Reaction for formation of a F_3 and a positive $\langle a \rangle$ or two F_3 faults from twin and a negative $\langle c \rangle$ interaction under a shear stress of 200 MPa is shown in Fig. 11a-b or c-d, respectively, which can be described by

$$\mathbf{b}_{-2/0} = \mathbf{b}_{0/1} + 2\mathbf{b}_{-1/-1}^{SF} + \mathbf{b}_t^{30} \tag{13}$$

or

$$\mathbf{b}_{-2/0} = 4\mathbf{b}_{-1/-1}^{SF} + 4\mathbf{b}_t^{30} + \mathbf{b}_{2/2} \tag{14}$$

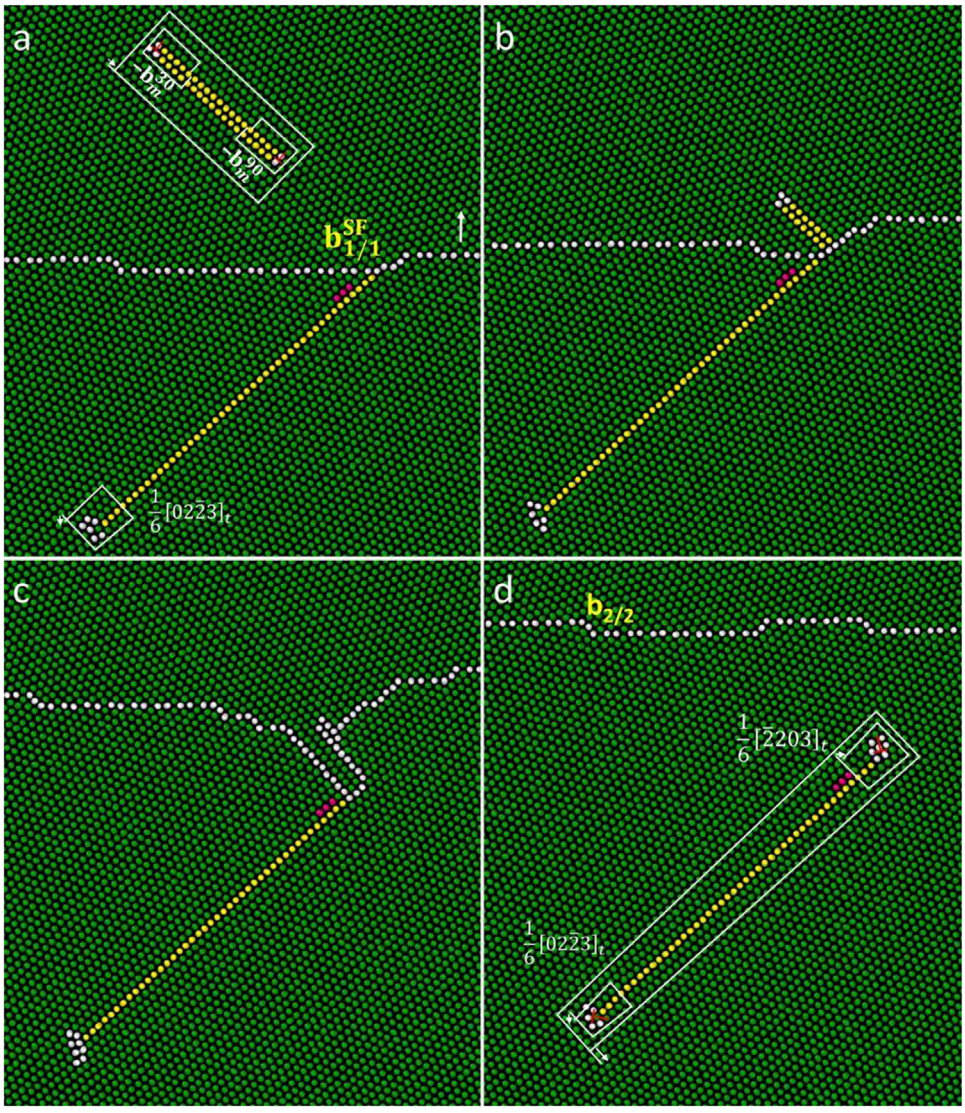

Fig. 8. (a) After the transmutation of the first $\mathbf{b}_{-1/0}$, a second $\mathbf{b}_{-1/0}$ is gliding toward the twin boundary. (b-c) When the transmutation of this second $\mathbf{b}_{-1/0}$ takes place at the intersection point between the I_1 fault and the twin boundary, (d) the I_1 fault that initially connects with the twin boundary detaches away, becomes isolated inside the twin and bounded by the conjugate Frank partials of $\frac{1}{6}[02\bar{2}3]_t$ and $\frac{1}{6}[\bar{2}203]_t$.

In addition to generating a negative basal $\langle\ a\ \rangle$ mixed dislocation, a positive $\frac{1}{2}\langle\ c\ \rangle$ dislocation can also produce a PB $\mathbf{b}_{8/7}$ disconnection after interacting with a $(10\bar{1}2)$ twin under sole shear stress. Reaction for formation of two PB $\mathbf{b}_{8/7}$ from twin and a positive $\langle\ c\ \rangle$ interaction under a shear stress of 200 MPa is shown in Fig.12, and can be described by

$$\mathbf{b}_{2/0} = 2\mathbf{b}_{2n/(2n-1)} + (2n-1)\mathbf{b}_{-2/-2} \tag{15}$$

It was further observed by Zhou et al. [112] that twin and a positive $\langle\ c\ \rangle$ interaction could produce multiple products in both the twin and matrix crystal, under simultaneous application of shear and compressive stresses. The interaction products included two basal $\langle\ a\ \rangle$ mixed dislocation gliding respectively on the matrix and twin crystal, and an I_1 fault in the twin that has one end connected with a $\mathbf{b}^{SF}_{-1/-1}$ disconnection and the other end bounded by a Frank partial dislocation.

3.1.2.2. Interaction with prismatic $\langle\ c+a\ \rangle$ mixed dislocation.

Interaction between a $(10\bar{1}2)$ twin and two partials of a positive or nagative prismatic $\langle\ c+a\ \rangle$ mixed dislocation under sole shear stress along $[\bar{1}011]$, is similar to the interaction between the twin and two partials of a positive or negative $\langle\ c\ \rangle$ dislocation, and these reactions can be described by equations (9–15). It should be noted that the products generated from the twin and a prismatic $\langle\ c+a\ \rangle$ interaction have sum of their screw components equal to the Burgers vector of an $\langle\ a\ \rangle$ screw dislocation, while the products generated from the twin and a $\langle\ c\ \rangle$ interaction have sum of their screw components equal to zero.

Apart from F_3 fault comprising two I_1 faults separated by two basal layers, twin and a Frank partial of a negative prismatic $\langle\ c+a\ \rangle$ interaction could also generate a pair of I_1 faults separated by other even number (e.g., four, six or even

Please cite this article as: Y. Yue, J. Wang and J.-F. Nie, Twin-solute, twin-dislocation and twin-twin interactions in magnesium, Journal of Magnesium and Alloys, https://doi.org/10.1016/j.jma.2023.07.015

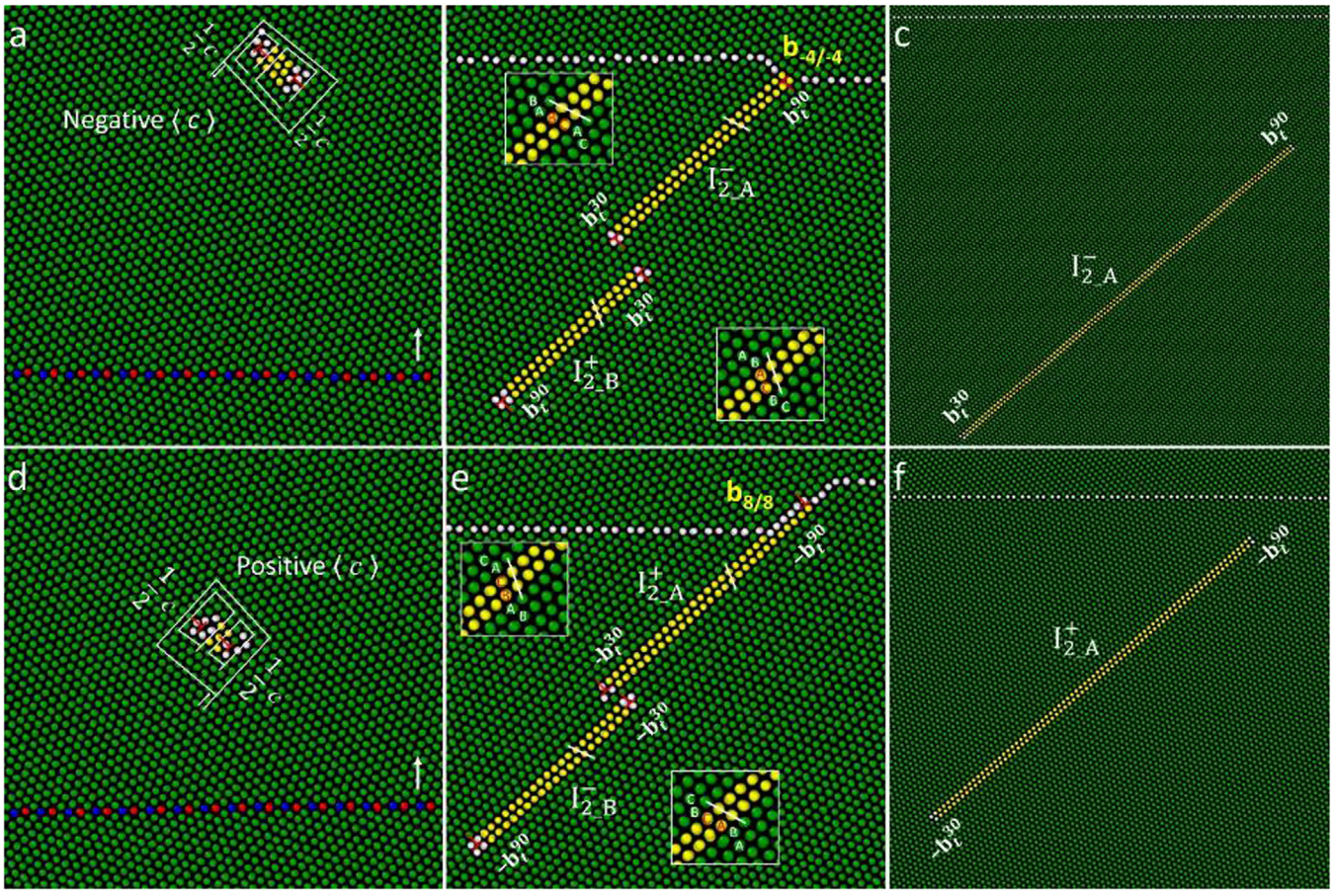

Fig. 9. Interaction between a migrating $(10\bar{1}2)$ twin boundary and a (a-c) negative and (d-f) positive prismatic ⟨ c ⟩ edge dislocations in the matrix lattice. The ⟨ c ⟩ dislocation comprises two $\frac{1}{2}$⟨ c ⟩ partials with an extrinsitc fault in between. Under a shear stress of 200 MPa along $[\bar{1}011]$ at 300 K, (b) the two negative $\frac{1}{2}$⟨ c ⟩ partials give rise to an $I^{-}_{2\_A}$ fault that is connected to a BP $\mathbf{b_{-4/-4}}$ disconnection on the twin boundary and a positive basal ⟨ a ⟩ mixed dislocation in the twin lattice, (e) the two positive $\frac{1}{2}$⟨ c ⟩ partials cause the formation of an $I^{+}_{2\_A}$ fault connected to a PB $\mathbf{b_{8/8}}$ disconnection and a negative basal ⟨ a ⟩ mixed dislocation in the twin lattice. The $I^{-}_{2\_A}$ and $I^{+}_{2\_A}$ faults detach from the twin boundary when the shear stress reaches 1.5 GPa and 1.7 GPa respectively, giving rise to another (c) positive and (f) negative ⟨ a ⟩ dislocations. Symbol $I^{+(-)}_{2\_A(B)}$ is used to describe the configuration of an I_2 fault in the twin lattice, where the superscript "+" or "-" indicates the shear direction $[10\bar{1}0]_t$ or $[\bar{1}010]_t$ that generates the I_2 fault, and the subscript A or B indicates that the change of the stacking sequence starts from the basal plane A or B in the twin lattice, in which the plane A or B intersects the extension or compression site of the twin boundary, respectively.

twelve) of basal layers, under sole shear stress. Such a pair of I_1 faults connect with two separate $\mathbf{b}^{SF}_{-1/-1}$and are bounded by a defect with a Burgers vector equal to $\mathbf{b^{30}}$. In this case, the Frank partial dislocation decomposes before crossing the twin boundary, and the interaction between the twin and the decomposed dislocations produces a pair of I_1 faults. Since decomposition requires sufficient driving force, a pair of I_1 faults can only form under a high shear stress larger than ~500 MPa, in comparison to F_3 that can be produced under a low shear stress even at 50 MPa. The process to form paired I_1 faults with a large even number of separation distances is illustrated in Fig. 13a-c or d-F, which can be described by Eq. (13) or (14), respectively.

Zhou et al. [112] also observed a paired of I_1 faults separated by one or three basal layers, which were produced when a Frank partial of a positive prismatic ⟨ $c + a$ ⟩ interacted with the twin under simultneous application of shear and compressive stresses. Paired of I_1 faults separated by odd number of basal layers connects with a BP $\mathbf{b}^{SF}_{-1/-1}$ and a PB $\mathbf{b}^{SF}_{1/1}$ disconnection on the twin boundary at one end, and an I_2 fault in the twin at the other end. This I_2 fault is bounded by a 30° and a 90° Shockley that are located at the close and the far end towards the twin boundary, these two Shockley partials have a total Burgers vector equal to that of a negative basal ⟨ a ⟩ mixed dislocation in the twin crystal.

3.1.2.3. Interaction with pyramidal ⟨ $c + a$ ⟩ mixed dislocation.

A previous simulation for Ti under zero applied stress [92], showed that a pyramidal ⟨ $c + a$ ⟩ mixed dislocation will decompose into a large height disconnection on a still $(10\bar{1}2)$ twin boundary, with emission of multiple TDs. The decomposition reaction of a pyramidal ⟨ $c + a$ ⟩ dislocation can be described by superposing equations for the decomposition reaction of a basal ⟨ a ⟩ mixed dislocation and the decomposition reaction of a prismatic ⟨ c ⟩ edge dislocation. On

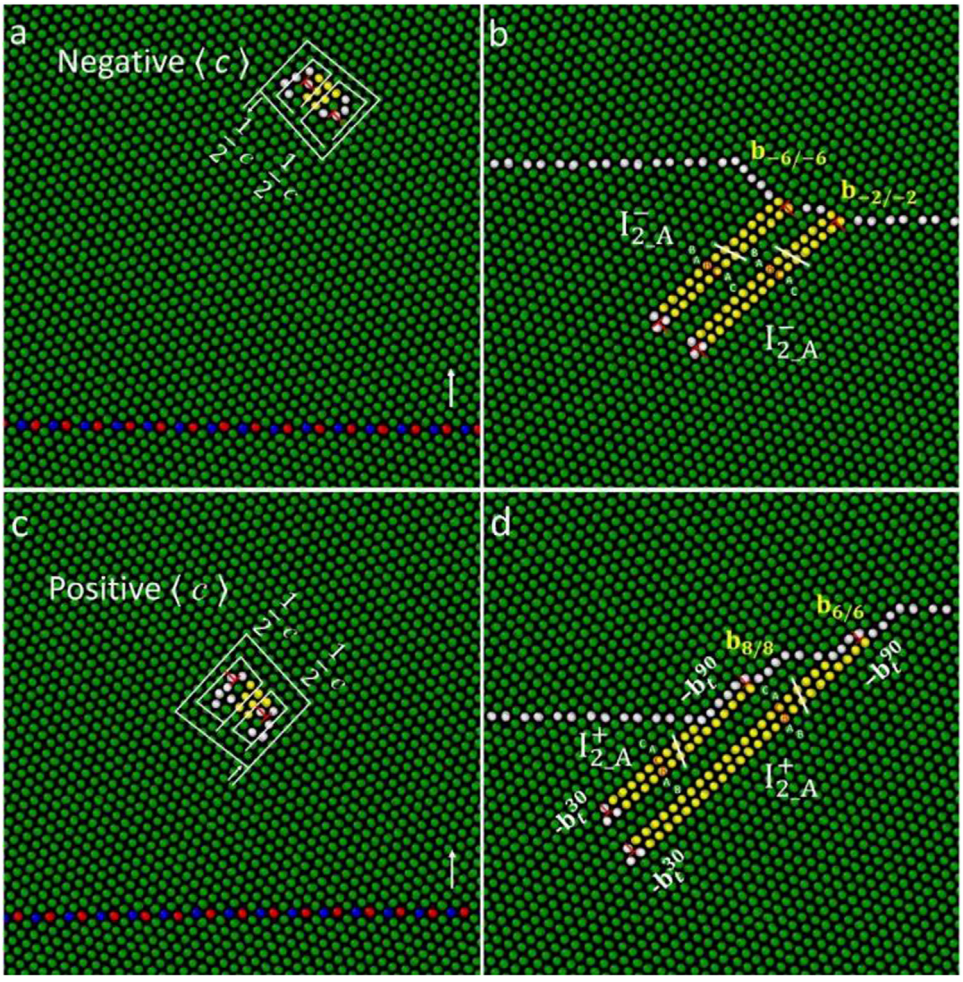

Fig. 10. Interaction between a migrating $(10\bar{1}2)$ twin boundary and (a-b) negative and (c-d) positive prismatic ⟨ *c* ⟩ edge dislocations in the matrix lattice. Under a shear stress of 200 MPa along $[\bar{1}011]$ at 300 K, (b) the two negative $\frac{1}{2}\langle c \rangle$ partials give rise to two $I^{-}_{2\_A}$ faults connected respectively to a BP $\mathbf{b_{-6/-6}}$ and a BP $\mathbf{b_{-2/-2}}$ disconnection, (d) the two positive $\frac{1}{2}\langle c \rangle$ partials cause the formation of two $I^{+}_{2\_A}$ faults connected respectively to a PB $\mathbf{b_{8/8}}$ and a PB $\mathbf{b_{6/6}}$ disconnection on the twin boundary.

this basis, the interaction between a pyramidal ⟨ *c* + *a* ⟩ mixed dislocation and a migrating $(10\bar{1}2)$ twin boundary in Mg under external applied stress, can be possibly predicted by incorporating the reaction between the twin and a basal ⟨ *a* ⟩ mixed dislocation and the reaction between the twin and a prismatic ⟨ *c* ⟩ edge dislocation.

For a negative pyramidal ⟨ *c* + *a* ⟩ dislocation, Figs. 14a-b, it can give rise to two I_2 faults in the twin and one I_2 fault in the matrix, after interacting with the $(10\bar{1}2)$ twin under sole shear stress of 200 MPa along $[\bar{1}011]$. Each of the I_2 fault connects with a BP $\mathbf{b_{-2n/-2n}}$ disconnection on the twin boundary through a 90° Shockley, and bounded by a 30° Shockley inside twin. Such a reaction can be described by

$$\mathbf{b_{-3/0}} = -\mathbf{b_m^{30}} + \left(-\mathbf{b_m^{90}} + \mathbf{b_{2n/2n}}\right) + 2\mathbf{b_t^{30}} + 2\left(\mathbf{b_t^{90}} + \mathbf{b_{-2n/-2n}}\right) + (n-1)\mathbf{b_{2/2}}, \quad (16)$$

and Eq. (16) can be regarded as the superposition of Eq. (4) and (11). Under a shear stress of 500 MPa, a same twin and pyramidal ⟨ *c* + *a* ⟩ interaction is found to produce two I_2 faults and one I_1 fault in the twin crystal, Fig. 14c. The resultant I_2 fault connect with $\mathbf{b_{-2n/-2n}}$ disconnection, and the resultant I_1 fault connect with a $\mathbf{b_{1/1}^{SF}}$ disconnection and is bounded by a $\frac{1}{6}[02\bar{2}3]_t$ Frank partial dislocation in the twin crystal. This reaction is described by

$$\mathbf{b_{-3/0}} = \mathbf{b_{1/1}^{SF}} + \frac{1}{6}\left[02\bar{2}3\right]_t + 2\mathbf{b_t^{30}} + 2\left(\mathbf{b_t^{90}} + \mathbf{b_{-2n/-2n}}\right) + 2n\mathbf{b_{2/2}} \quad (17)$$

and Eq. (17) can be regarded as the superposition of Eq. (5) and (11).

It was observed that under simultaneous application of shear and tensile stresses [112], the I_2 faults generated from the interaction between the $(10\bar{1}2)$ twin and a negative pyramidal ⟨ *c* + *a* ⟩ dislocation, as those shown in Figs. 14a-b, can detach away. This results in two basal ⟨ *a* ⟩ mixed dislocations in the twin and one basal ⟨ *a* ⟩ mixed dislocation in the matrix, and such reaction can be expressed by

$$\mathbf{b_{-3/0}} = \mathbf{b_{-1/0}} + 2\mathbf{b_{0/1}} + \mathbf{b_{-2/-2}}. \quad (18)$$

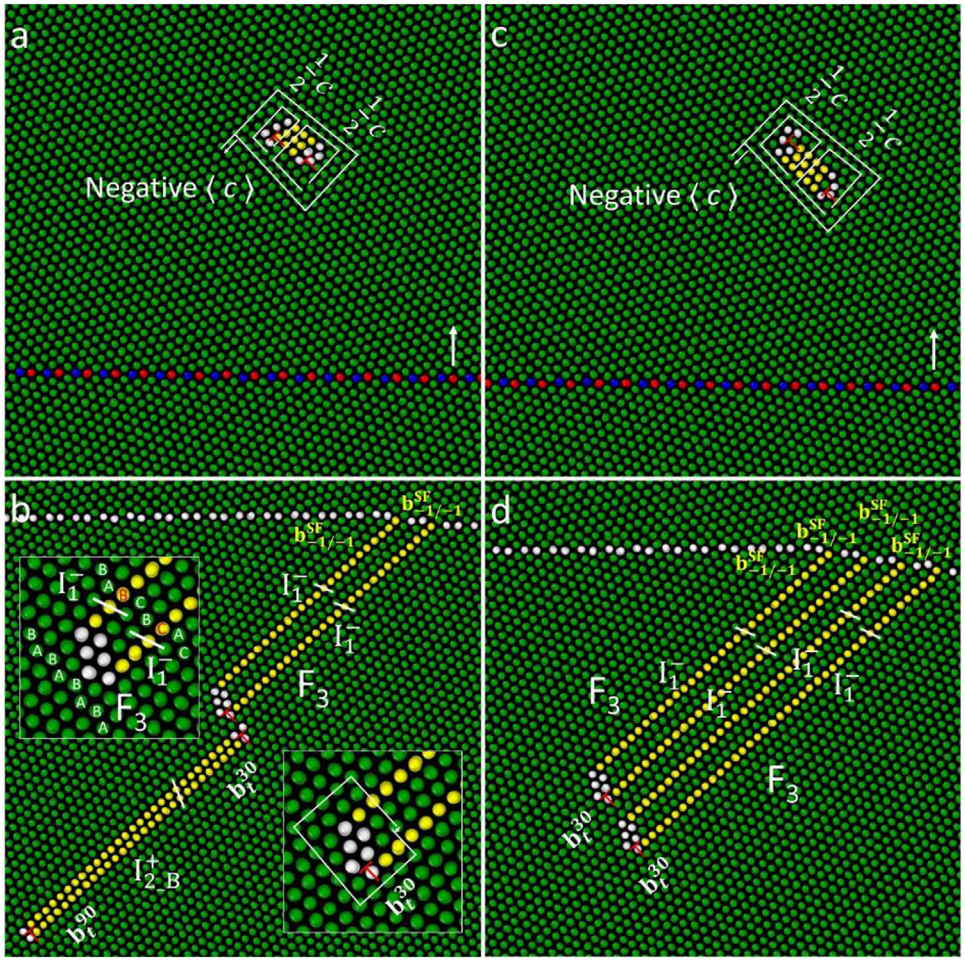

Fig. 11. Interaction between a migrating $(10\bar{1}2)$ twin boundary and two $\frac{1}{2}\langle\ c\ \rangle$ partials of a negative prismatic $\langle\ c\ \rangle$ edge dislocation gives rise to (a-b) a F_3 fault and a positive basal $\langle\ a\ \rangle$ mixed dislocation in the twin or (c-d) two F_3 faults, under a shear stress of 200 MPa along $[\bar{1}011]$ at 300 K.

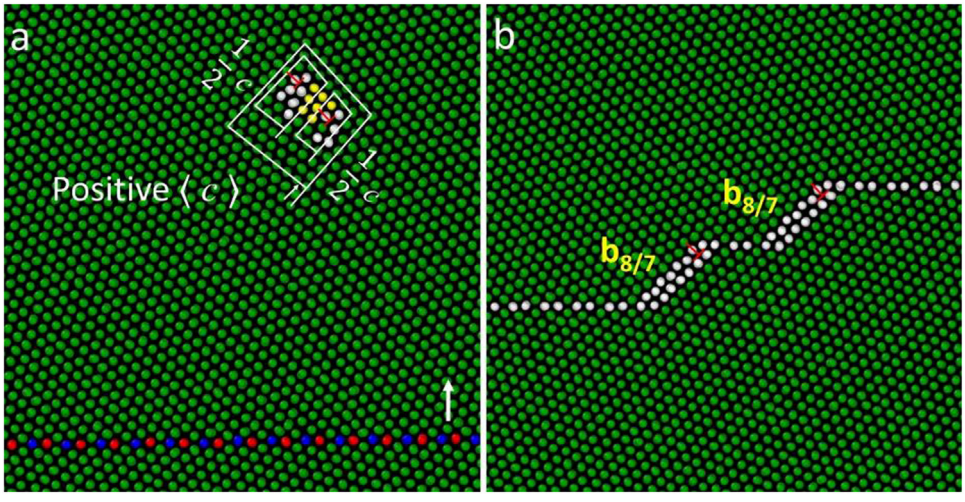

Fig. 12. Interaction between a migrating $(10\bar{1}2)$ twin boundary and two $\frac{1}{2}\langle\ c\ \rangle$ partials of a positive prismatic $\langle\ c\ \rangle$ edge dislocation produce two PB $\mathbf{b_{8/7}}$ disconnections under a shear stress of 200 MPa along $[\bar{1}011]$ at 300 K.

Please cite this article as: Y. Yue, J. Wang and J.-F. Nie, Twin-solute, twin-dislocation and twin-twin interactions in magnesium, Journal of Magnesium and Alloys, https://doi.org/10.1016/j.jma.2023.07.015

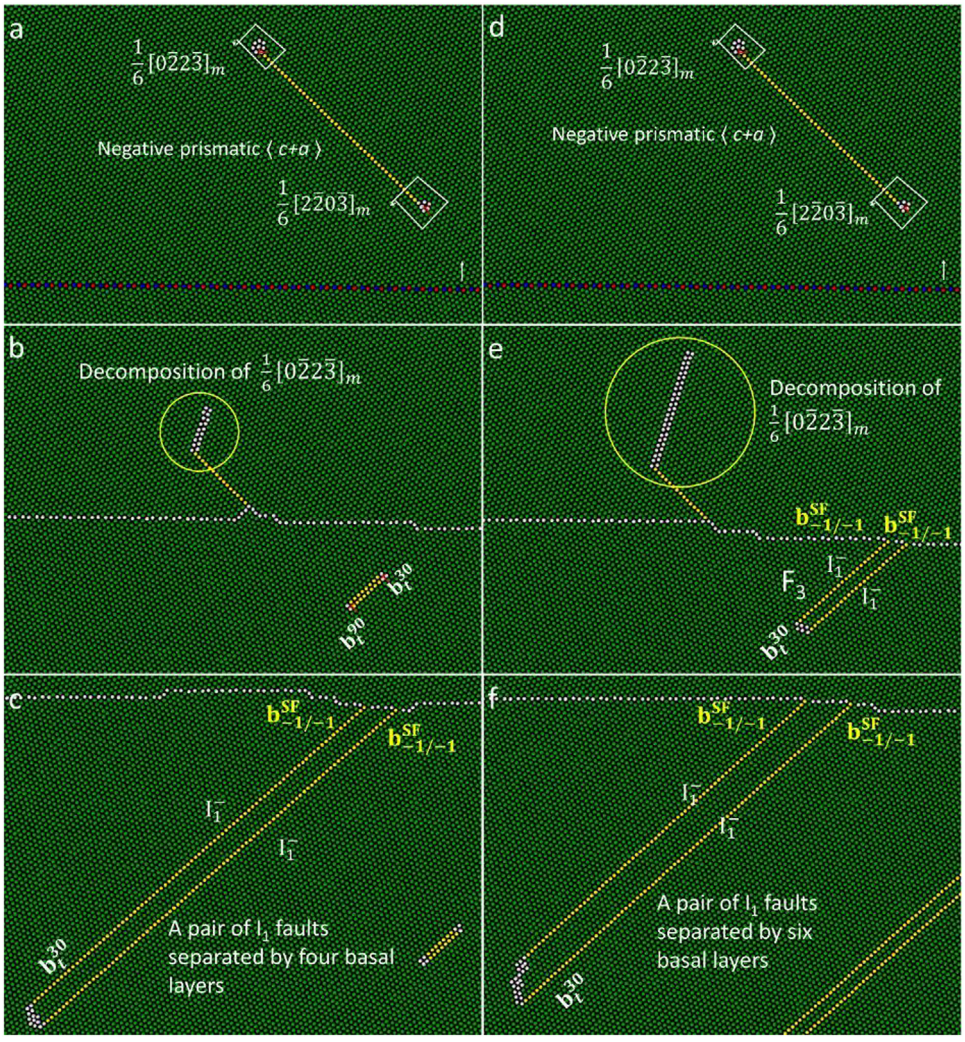

Fig. 13. Interaction between a migrating $(10\bar{1}2)$ twin boundary and a negative prismatic ⟨ $c + a$ ⟩ mixed dislocation in the matrix lattice under a shear stress of (a-c) 500 MPa and (d-f) 520 MPa along $[\bar{1}011]$ at 300 K. The ⟨ $c + a$ ⟩ dislocation comprises $\frac{1}{6}[2\bar{2}0\bar{3}]_m$ and $\frac{1}{6}[0\bar{2}2\bar{3}]_m$ Frank partials with an I_1 fault in between. The $\frac{1}{6}[2\bar{2}0\bar{3}]_m$ parital gives rise to either (b) a positive basal ⟨ a ⟩ mixed dislocation or (e) a F_3 fault in the twin lattice after interacting with the twin; while the $\frac{1}{6}[0\bar{2}2\bar{3}]_m$ partial has decomposed before meeting the twin boundary, and the interaction between the decomposed dislocations and the twin produces a pair of I_1 faults that are separated by (c) four or (f) six basal layers.

For a positive pyramidal ⟨ $c + a$ ⟩ dislocation, Figs. 15a-b, it can give rise to two PB $\mathbf{b_{8/7}}$ disconnection and one BP $\mathbf{b_{-7/-8}}$ disconnection on the twin boundary, after its interaction with the twin boundary under a shear stress of 200 MPa along $[\bar{1}011]$. This reaction can be described by

$$\mathbf{b_{3/0}} = \mathbf{b_{-(2n-1)/-2n}} + 2\mathbf{b_{2n/(2n-1)}} + (\mathrm{n}-1)\mathbf{b_{-2/-2}} \tag{19}$$

and Eq. (19) can be regarded as the superposition of Eq. (1) and (15). Under a shear stress of 700 MPa, a same twin and pyramidal ⟨ $c + a$ ⟩ interaction generates two I_2 faults and one I_1 fault in the twin crystal, Fig. 15c. Each of the I_2 fault connects with a $\mathbf{b_{2n/2n}}$ disconnection, and the resultant I_1 fault connects with a $\mathbf{b}^{SF}_{1/1}$disconnection and is bounded by a $\frac{1}{6}[2\bar{2}0\bar{3}]_t$ Frank partial dislocation in the twin crystal. This reaction can be described by

$$\mathbf{b_{3/0}} = \mathbf{b}^{SF}_{1/1} + \frac{1}{6}\left[2\bar{2}0\bar{3}\right]_t + 2\left(-\mathbf{b}_t^{30}\right) + 2\left(-\mathbf{b}_t^{90} + \mathbf{b_{2n/2n}}\right) + (2\mathrm{n}-1)\mathbf{b_{-2/-2}} \tag{20}$$

and Eq. (20) can be regarded as the superposition of Eq. (2) and (12).

It was observed that under simultaneous application of shear and compressive stresses [112], the disconnections generated from the interaction between the $(10\bar{1}2)$ twin and a positive pyramidal ⟨ $c + a$ ⟩ dislocation, as those shown in Figs. 15a-b, were able to emit basal ⟨ a ⟩ mixed dislocations by further reacting with TDs. As a result, two ⟨ a ⟩ mixed dislocations in the twin and one ⟨ a ⟩ mixed dislocation in the matrix can be produced through the twin and a positive pyramidal ⟨ $c + a$ ⟩ interaction, with this reaction expressed as

$$\mathbf{b_{3/0}} = \mathbf{b_{1/0}} + 2\mathbf{b_{0/-1}} + \mathbf{b_{2/2}} \tag{21}$$

It should be further noted that a pyramidal ⟨ $c + a$ ⟩ dislocation has one of its partial dislocations, i.e., $\frac{1}{6}[02\bar{2}3]_m$ or $\frac{1}{6}[0\bar{2}2\bar{3}]_m$, same to that of a prismatic ⟨ $c + a$ ⟩ dislocation. Therefore, product such as the F_3 fault or a pair of I_1 faults,

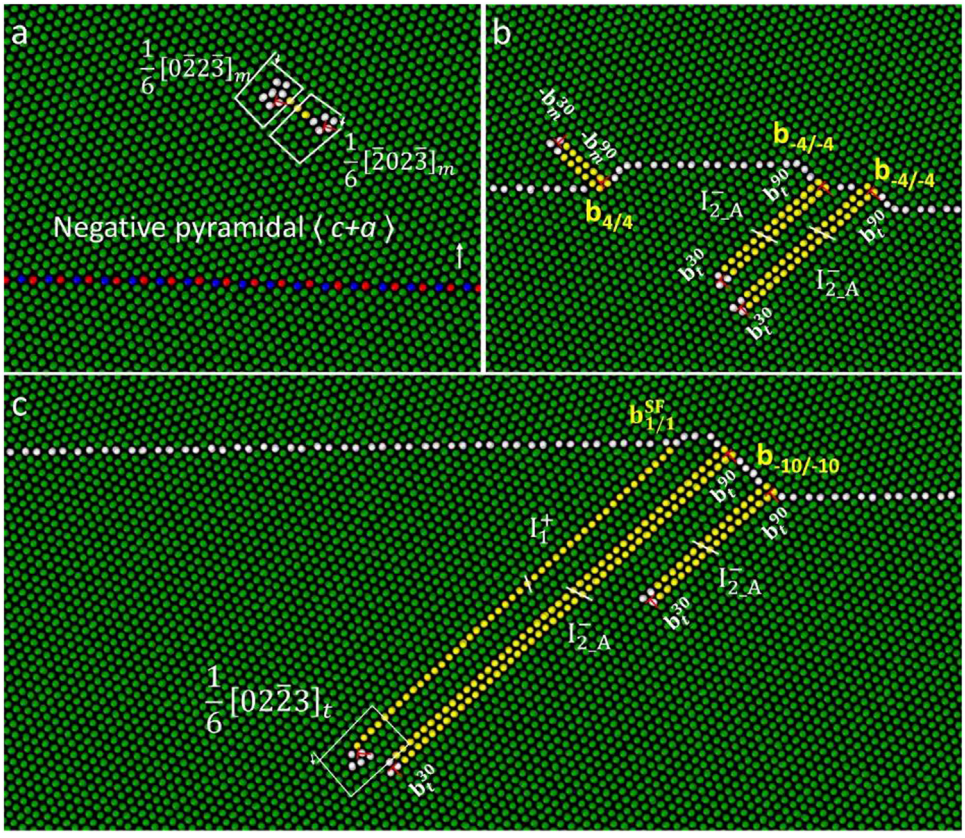

Fig. 14. Interaction between a migrating $(10\bar{1}2)$ twin boundary and a negative pyramidal $\langle\, c+a \,\rangle$ mixed dislocation in the matrix lattice under a shear stress of (a-b) 200 MPa and (a-c) 500 MPa along $[\bar{1}011]$ at 300 K. The $\langle\, c+a \,\rangle$ dislocation comprises $\frac{1}{6}[\bar{2}023]_m$ and $\frac{1}{6}[0\bar{2}\bar{2}3]_m$ Frank partials with an I_1 fault in between. Products for (a-b) include two $I_{2\_A}^{-}$ faults in the twin that are connected respectively to two BP $\mathbf{b_{-4/-4}}$ disconnections, and one I_2 fault in the matrix that is connected with a PB $\mathbf{b_{4/4}}$ disconnection. Products for (a-c) are two $I_{2\_A}^{-}$ faults in the twin that are connected with a BP $\mathbf{b_{-10/-10}}$ disconnection, and one I_1^+ fault in the twin that is connected with a $\mathbf{b_{1/1}^{SF}}$ disconnection and bounded by a $\frac{1}{6}[02\bar{2}3]_t$ Frank partial dislocation.

generated from the twin-$\frac{1}{6}[02\bar{2}3]_m$ or twin-$\frac{1}{6}[0\bar{2}\bar{2}3]_m$ interaction, is expected to be observed when a pyramidal $\langle\, c+a \,\rangle$ dislocation interacts with a $(10\bar{1}2)$ twin.

The products generated from the $(10\bar{1}2)$ twin and a pyramidal $\langle\, c+a \,\rangle$ interaction and shown in MD simulations above, are found to be always multiple. This is different from that was predicted by Niewczas [108] based on the lattice correspondence relationship, in which a slip system $(10\bar{1}1)[2\bar{1}\bar{1}3]_m$ was suggested to transform to a slip system of $(\bar{1}01\bar{4})[52\bar{7}3]_t$ after crossing a $(10\bar{1}2)$ twin boundary.

3.1.3. *Effect of* $\{10\bar{1}2\}$ *twin and dislocation interactions on plastic deformation*

Interaction between the $(10\bar{1}2)$ twin and basal $\langle\, a \,\rangle$ mixed dislocations can produce BP/PB disconnection in which TDs are able to spontaneously cross over. This enables the twin boundary to progress through a forest of basal dislocations with no apparent loss of mobility, and thus is believed to be responsible for the high growth rates associated with the $\{10\bar{1}2\}$ twinning mode in Mg [106]. Besides, it was reported by Serra and Bacon [69] that the BP $\mathbf{b_{-(2n-1)/-2n}}$ type disconnection can be the source of a pair of TDs with opposites sign, which assists the twinning process and explains the low stress required for the growth of a $(10\bar{1}2)$ twin.

The transmutation of basal $\langle\, a \,\rangle$ mixed dislocations across the $(10\bar{1}2)$ twin boundary explains the experimental observation of abundant $\langle\, c+a \,\rangle$ dislocations and basal SFs in the vicinity of the twin boundary in Mg [31,34,114-118]. The transmutation products are mostly sessile and thus can contribute to forest hardening mechnism against other slip within the twin [34]. In addition, transmutation of $\langle\, a \,\rangle$ dislocations provides a source mechanism for $\langle\, c+a \,\rangle$ dislocation. This gives a suitable route to introduce $\langle\, c+a \,\rangle$ dislocations at a low external applied stress since $\langle\, a \,\rangle$ dislocations can be easily activated. However, in the work of Chen et al. [119], it was suggested that the hardening caused by the transmutation of basal $\langle\, a \,\rangle$ dislocation across the $(10\bar{1}2)$ twin boundary is ineffective in Mg, where the twin boundary was considered to migrate through a "pure shuffling" mechanism. In their simulations, a free surface boundary condition was adopted for the three principal axes of their simulation box, with the boundary between the parent and the twin being either a $(10\bar{1}2)$ CTB or a macroscopic long BP interface. They observed that transmutation only occurred for dislocations with a Burgers vector parallel to the $\lceil 1\bar{2}10 \rceil$ zone axis of the twin, while basal $\langle\, a \,\rangle$

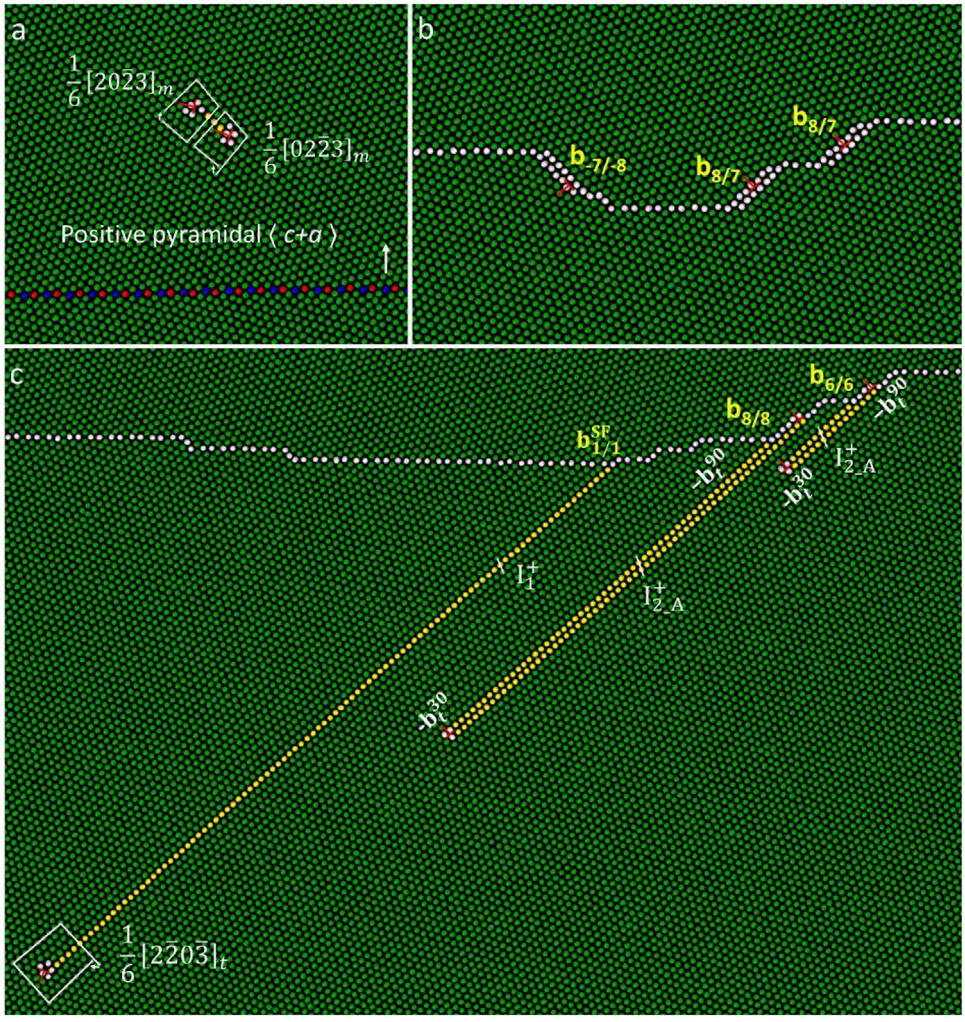

Fig. 15. Interaction between a migrating $(10\bar{1}2)$ twin boundary and a positive pyramidal $\langle c+a \rangle$ mixed dislocation in the matrix lattice under a shear stress of (a-b) 200 MPa and (a-c) 700 MPa along $[\bar{1}011]$ at 300 K. The $\langle c+a \rangle$ dislocation comprises $\frac{1}{6}[02\bar{2}3]_m$ and $\frac{1}{6}[20\bar{2}3]_m$ Frank partials with an I_1 fault in between. Products for (a-b) include two PB $\mathbf{b_{8/7}}$ disconnections and one BP $\mathbf{b_{.7/-8}}$ disconnection on the twin boundary. Products for (a-c) are two $I_{2\_A}^{+}$ faults in the twin that are connected respectively with a PB $\mathbf{b_{8/8}}$ and a PB $\mathbf{b_{6/6}}$ disconnection, and one I_1^{+} fault in the twin that is connected with a $\mathbf{b_{1/1}^{SF}}$ disconnection and bounded by a $\frac{1}{6}[2\bar{2}0\bar{3}]_t$ Frank partial dislocation.

mixed dislocation with a Burgers vector not parallel to$[1\bar{2}10]$ could only be absorbed by the twin boundary. In contrast, the interactions between basal $\langle a \rangle$ mixed dislocations and a coherent $(10\bar{1}2)$ twin boundary that migrates through glide of TDs, which is the focus of this review paper, lead to both absorption and transmutation of a basal $\langle a \rangle$ mixed dislocation, but under different stress states, consistent with previous simulations made by Barrett et al. [29] and Wang et al. [31]. This suggests that the different migration mechanisms of $(10\bar{1}2)$ CTB and a long BP/PB interface (comprising only BP/PB segments) may affect the twin-dislocation interaction. In addition, variations in the boundary conditions and external stresses applied in the simulations can also impact the simulation results.

A $\langle c \rangle$ or $\langle c+a \rangle$ type dislocation is easily to dissociate into two Frank partial dislocations that has a basal stacking fault connecting between them. The basal-dissociated $\langle c \rangle$ or $\langle c+a \rangle$ type dislocations are immobile, and unable to accommodate the plastic strain, thus impairing the ductility of Mg [85]. After interacting with a $(10\bar{1}2)$ twin, the immobile basal-dissociated $\langle c \rangle$ or $\langle c+a \rangle$ dislocations are eliminated. This means that interactions between the twin and $\langle c \rangle$ or $\langle c+a \rangle$ enable to refresh the plastic deformation capability of Mg [112].

The $(10\bar{1}2)$ twin and $\langle c \rangle$ or $\langle c+a \rangle$ interaction can produce disconnections on the twin boundary or I_2 faults (either in the matrix or twin crystal) that connect with the twin boundary. The resultant disconnections are able to emit basal $\langle a \rangle$ mixed dislocations by further reacting with TDs, and the resultant I_2 faults can detach away from the twin boundary to produce $\langle a \rangle$ mixed dislocations when sufficient stresses are applied externally. This suggests that transformation of sessile $\langle c \rangle$ or $\langle c+a \rangle$ type dislocation to glissle $\langle a \rangle$ dislocations by $(10\bar{1}2)[\bar{1}011]$ twinning can be accomplished,

Please cite this article as: Y. Yue, J. Wang and J.-F. Nie, Twin-solute, twin-dislocation and twin-twin interactions in magnesium, Journal of Magnesium and Alloys, https://doi.org/10.1016/j.jma.2023.07.015

and this gives a possible way to further improve the ductility of Mg.

Apart from I_2 faults that connect with the twin boundary, I_1 or a pair of I_1 faults that connect with the twin boundary are also observed from $(10\bar{1}2)$ twin and $\langle c \rangle$ or $\langle c+a \rangle$ interactions. These SFs connect with sessile $\mathbf{b}^{SF}_{\pm 1/\pm 1}$ interfacial defects in which TDs can move through conservatively [110,111]. As a result, the migration of the twin boundary will not be impeded by $\mathbf{b}^{SF}_{\pm 1/\pm 1}$, and SFs can be extended concomitantly with the twin growth. The elongation of the length of SFs can increase the total fault energy, and the basal SFs can be barriers for dislocations gliding on non-basal planes, resulting in strain hardening.

3.2. Interaction between $\{10\bar{1}1\}$ contraction twin and different types of dislocations

3.2.1. Interaction with $\langle a \rangle$ type dislocations

MD simulation for Mg shows that a basal $\langle a \rangle$ screw dislocation can be absorbed by a $(10\bar{1}1)$ twin boundary, leading to its decomposition into two TDs with a step height of two atomic layers [120]. The two TDs have the same screw components and opposite edge components, and they can glide along the $(10\bar{1}1)$ twin boundary. The interaction behavior is also observed in MD simulations for Ti [97,121].

Under sole application of shear stress along the twin plane, a basal $\langle a \rangle$ mixed dislocation can dissociate into a glissile TD with a height of two atomic layers and an immobile $\mathbf{b_{1/2}}$ disconnection at the $(10\bar{1}1)$ twin boundary, as observed in MD simulations for Mg in the work of Wang et al. [122]. Su et al. [123] have proposed a similar interaction behavior, in which a $\mathbf{b_{3/2}}$ or $\mathbf{b_{-3/-2}}$ interfacial defect on the $(10\bar{1}1)$ twin boundary was suggested to produced from the interaction between a twin and a basal $\langle a \rangle$ mixed dislocation, based on the analysis of atomic-resolution images obtained. This type reaction can be expressed as :

$$\mathbf{b_{1/0}} = \mathbf{b_{2n+1/2n}} + n\mathbf{b_{-2/-2}} \tag{22}$$

or

$$\mathbf{b_{-1/0}} = \mathbf{b_{-(2n+1)/-2n}} + n\mathbf{b_{2/2}} \tag{23}$$

for twin and a positive or negative $\langle a \rangle$ interaction, respectively.

In additional to decomposing into an interfacial defect and TDs, a basal $\langle a \rangle$ mixed dislocation was also suggested by Su et al. [123] to produce a SALH disconnection on the twin boundary after its interaction with a $(10\bar{1}1)$ twin. The resultant SALH disconnection does not connect any stacking fault, and this process is accompanied by the emission or absoprtion of another basal $\langle a \rangle$ mixed dislocation into the twin crystal. This reaction is predicted based on the theory of interfacial defect [88,124-128] and crystallographic analysis and can be described as :

$$\mathbf{b_{1/0}} = \mathbf{b_{1/1}} + \mathbf{b_{0/-1}} \tag{24}$$

or

$$\mathbf{b_{1/0}} + \mathbf{b_{0/1}} = \mathbf{b_{1/1}} \tag{25}$$

for the twin and positive $\langle a \rangle$ interaction, and

$$\mathbf{b_{-1/0}} = \mathbf{b_{-1/-1}} + \mathbf{b_{0/1}} \tag{26}$$

or

$$\mathbf{b_{-1/0}} + \mathbf{b_{0/-1}} = \mathbf{b_{-1/-1}} \tag{27}$$

for the twin and negative $\langle a \rangle$ interaction. Su et al. [123] suggested that the resultant $\mathbf{b_{1/1}}$ or $\mathbf{b_{-1/-1}}$ can relax to a step-SF intersection with a $\mathbf{b}^{SF}_{\mathbf{1/1}}$ or $\mathbf{b}^{SF}_{\mathbf{-1/-1}}$ disconnection that connects to an I_1 fault by absorbing or emitting a Frank partial dislocation in the form of $\frac{1}{6}\langle 20\bar{2}3\rangle$.

In contrast to the formation of a SALH disconnection that does not connect to any stacking faut, MD simulations in Mg condcuted by Li et al. [129] showed that a basal $\langle a \rangle$ mixed dislocation generated a stacking fault on the $(\bar{1}011)$ pyramidal plane and connected to a one-layer step on the twin boundary after interacting with a $(10\bar{1}1)$ twin, under simultanous application of shear and normal strains. Li et al. [129] subsequently observed that the fault region was erased when a second basal $\langle a \rangle$ mixed dislocation entered the same twin boundary, with the formation of two Frank partial dislocations in the twin and a two-atomic-layer-height TD on the twin boundary. The resultant Frank partials have a sum of their Burgers vectors equal to a pyramidal $\langle c+a \rangle$ dislocation. The overall reaction can be expressed as:

$$2\mathbf{b_{1/0}} = \frac{1}{6}\left[\bar{2}02\bar{3}\right]_t + \frac{1}{6}\left[0\bar{2}2\bar{3}\right]_t + \mathbf{b_{2/2}} \tag{28}$$

or

$$2\mathbf{b_{-1/0}} = \frac{1}{6}\left[20\bar{2}3\right]_t + \frac{1}{6}\left[02\bar{2}3\right]_t + \mathbf{b_{-2/-2}} \tag{29}$$

for twin and a positive or negative $\langle a \rangle$ interaction, respectively. It is noteworthy that the transmutation of basal $\langle a \rangle$ mixed dislocations to a pyramidal $\langle c+a \rangle$ dislocation, as shown in the above simulation, is different from what was predicted by Niewczas [108]. Niewczas suggested that the slip system of a basal $\langle a \rangle$ mixed dislocation in the matrix, i.e., $(0001)[2\bar{1}\bar{1}0]_m$, transformed to $(10\bar{1}\bar{1})[14\bar{5}6]_t$ in the $(10\bar{1}1)$ twin crsytal.

In addition to gliding on the basal plane, $\langle a \rangle$ type dislocations can also gilde on $\{10\bar{1}0\}$ prismatic plane, referred to as prismatic $\langle a \rangle$ dislocations. The slip system of a prismatic $\langle a \rangle$ in the matrix can be $(10\bar{1}0)[\bar{1}2\bar{1}0]_m$,$(0\bar{1}10)[2\bar{1}\bar{1}0]_m$and $(1\bar{1}00)[\bar{1}\bar{1}20]_m$. Chen et al. [107] conducted MD simulations and found that the $(10\bar{1}0)[\bar{1}2\bar{1}0]_m$ slip system in Mg transformed to the $(10\bar{1}3)[\bar{1}2\bar{1}0]_t$ slip system in the $(10\bar{1}1)$ twin, in agreement with the calculations based on lattice correspondence transformation made by Niewczas [108]. The $(0\bar{1}10)[2\bar{1}\bar{1}0]_m$ transforms to $(1\bar{1}01)[01\bar{1}1]_t$, which is close to the result of $(3\bar{4}13)[14\bar{5}6]_t$ in the mathematical calculation [108]. However, the $(1\bar{1}00)[\bar{1}\bar{1}20]_m$ slip system transforms to $(2\bar{1}\bar{1}1)[\bar{1}2\bar{1}3]_t$, which largely deviates from the calculation result of $(\bar{3}4\bar{1}\bar{3})[14\bar{5}6]_t$ [108]. The transformation process of $(1\bar{1}00)[\bar{1}\bar{1}20]_m$ to $(2\bar{1}\bar{1}1)[\bar{1}2\bar{1}3]_t$ in the work of Chen et al. [107] is shown in Fig. 16. In this process, a prismatic $\langle a \rangle$

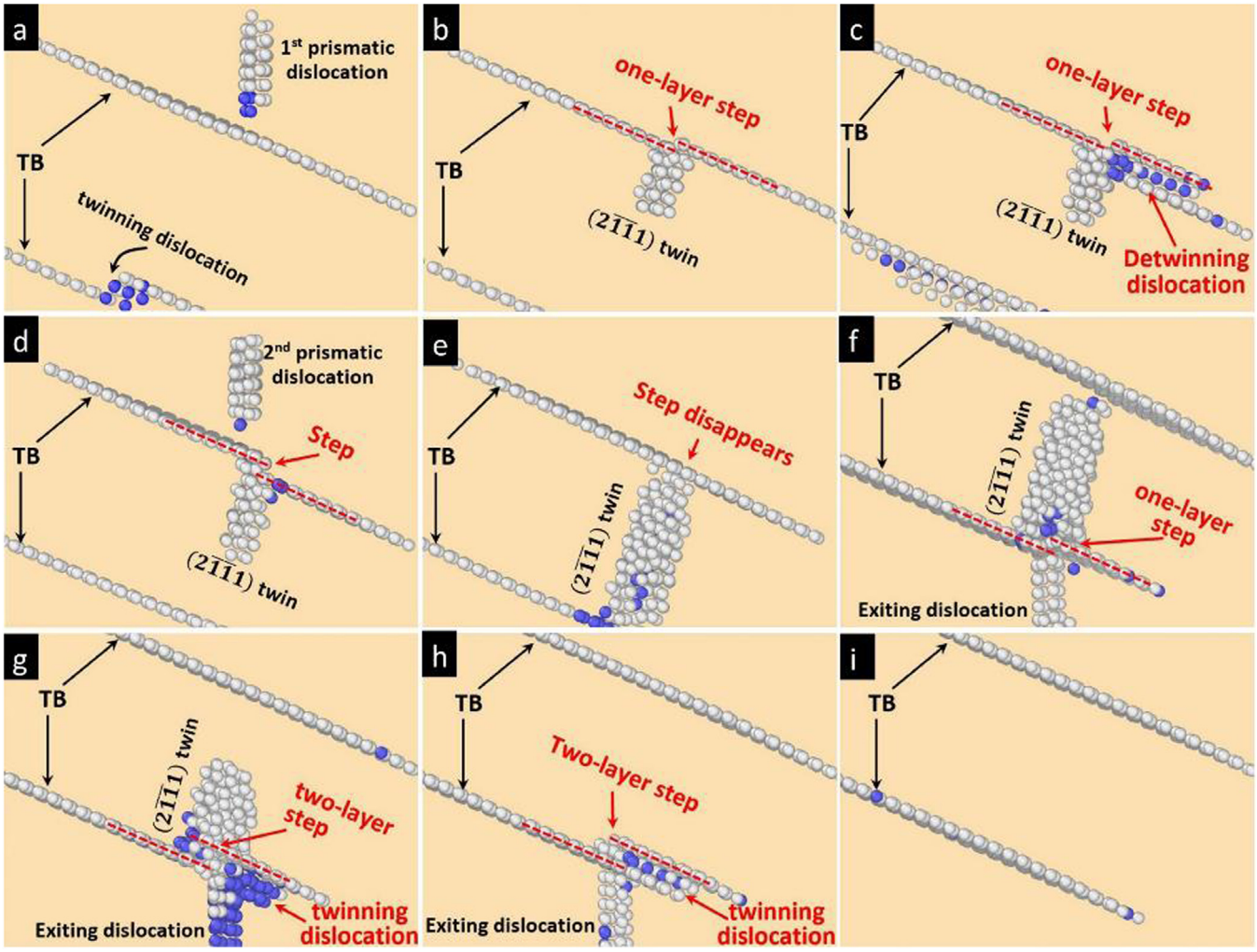

Fig. 16. (a) Interaction between the 1st prismatic dislocation and the upper (10$\bar{1}$1) twin boundary, produces (b) a one-layer step on the twin boundary and (2$\bar{1}\bar{1}$1) twin inside the (10$\bar{1}$1) twin. (c) A double layered detwinning dislocation glides toward the one-layer step. (d) The 2nd prismatic dislocation is approaching the upper twin boundary and (e) its interaction with the twin boundary erases the steps on the upper twin boundary. (f) The (2$\bar{1}\bar{1}$1) twin is approaching the lower (10$\bar{1}$1) twin boundary, and a one-layer step is generated at the lower twin boundary as the (2$\bar{1}\bar{1}$1) twin is transmuted into a prismatic dislocation that exists from the (10$\bar{1}$1) twin. (g-i) When the (2$\bar{1}\bar{1}$1) twin is transmuted into a 2nd prismatic dislocation, the step height on the lower twin boundary increases to two layers. Meanwhile, a double-layered twinning dislocation nucleates at the intersection, and removes the two-layer step on the lower twin boundary. The simulation is conducted under a tensile strain along the [2$\bar{1}\bar{1}$0] direction at 100 K [107].

dislocation transmutes into a (2$\bar{1}\bar{1}$1) twin inside a (10$\bar{1}$1) twin. The resultant (2$\bar{1}\bar{1}$1) twin grows towards the opposite (10$\bar{1}$1) twin boundary when a second same type $\langle a \rangle$ is impinged on the same location at the twin boundary as the first $\langle a \rangle$. The (2$\bar{1}\bar{1}$1) twin eventually reaches the opposite twin boundary and transmutes back into prismatic dislocations in the matrix after exitting the (10$\bar{1}$1) twin. The net effect is that the matrix prismatic dislocations are transmitted across a (10$\bar{1}$1) twin, and the transformation between prismatic $\langle a \rangle$ dislocations and (2$\bar{1}\bar{1}$1) twin across the (10$\bar{1}$1) twin boundary is proved to be feasible based on the lattice correspondence analysis.

3.2.2. *Interaction with* $\langle c \rangle$ *or* $\langle c + a \rangle$ *type dislocations*

Previous MD simulations on a matrix prismatic $\langle c \rangle$ edge dislocation in Ti [121] have shown that its interaction with a (10$\bar{1}$1) twin results in the formation of two glissile TDs each with two-atomic-layer height, a sessile residual defect at the twin boundary and a basal $\langle a \rangle$ mixed dislocation in the twin crystal, under simultaneous application of shear and normal strains. The resultant two TDs have opposite signs, and the basal $\langle a \rangle$ mixed dislocation has its 30° Shockley connected to the twin boundary and its 90° Shockley seperated by the twin boundary by an I_2 fault. However, Yoo [36] proposed a different interaction mechanism, in which a matrix prismatic $\langle c \rangle$ edge dislocation can transform to a dislocation with a Burgers vector of $[\bar{3}032]_t$ in the twin crystal, together with the formation of glissile two-atomic-layer-height TDs on the twin boundary. The resultant $[\bar{3}032]_t$ dislocation can further decompose into a combination of $\langle a \rangle$ and $\langle c \rangle$ type dislocations, through the reaction $[\bar{3}032]_t \rightarrow 3 \cdot \frac{1}{3}[\bar{2}110]_t + 3 \cdot \frac{1}{3}[\bar{1}\bar{1}20]_t + 2 \cdot [0001]_t$, generat-

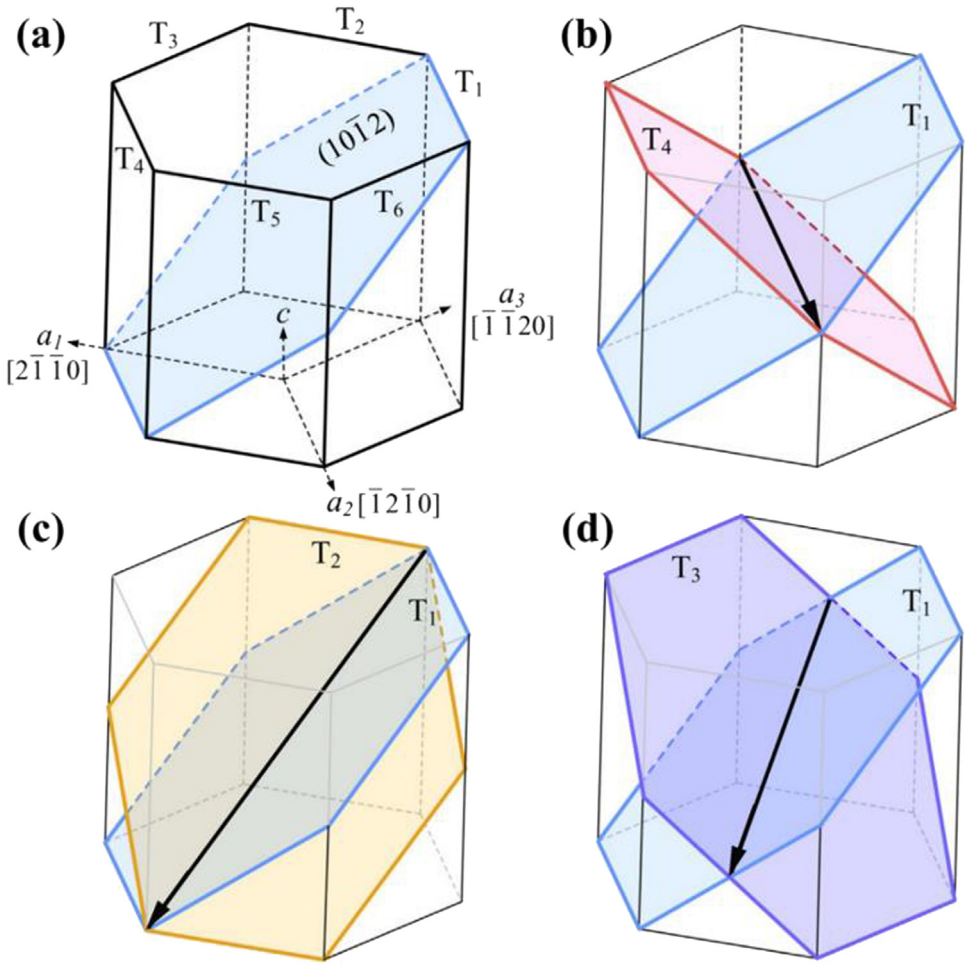

Fig. 17. (a) Six crystallographically equivalent {10$\bar{1}$2}⟨$\bar{1}$011⟩ twin variants T_i (i = 1–6) in a hcp crystal produce three different types of twin-twin interactions, including (b) Type I co-zone twin-twin interaction between T_1 and T_4, (c) Type II(a) non-co-zone twin-twin interaction between T_1 and T_2, and (d) Type II(b) non-co-zone twin-twin interaction between T_1 and T_3 [39].

ing six basal ⟨ a ⟩ mixed and two prismatic ⟨ c ⟩ edge dislocations inside the twin.

Su et al. [123] have suggested that when a prismatic ⟨ $c + a$ ⟩ mixed dislocation in the matrix crystal interacts with a (10$\bar{1}$1) twin, the resulting configuration can be similar to that between a matrix basal ⟨ a ⟩ mixed dislocation and the same twin. This interaction produces a $\mathbf{b_{1/1}}$ or $\mathbf{b_{-1/-1}}$ SALH disconnection on the twin boundary, and is accompanied by the emission or absoprtion of a basal ⟨ a ⟩ mixed dislocation into the twin crystal. The resultant $\mathbf{b_{1/1}}$ or $\mathbf{b_{-1/-1}}$ can then evolve into a step-SF intersection with a $\mathbf{b}^{SF}_{1/1}$ or $\mathbf{b}^{SF}_{-1/-1}$ disconnection that connects with an I_1 fault, after absorbing or emitting a Frank partial dislocation of the type $\frac{1}{6}\langle 20\bar{2}3\rangle$.

When a pyramidal ⟨ $c + a$ ⟩ mixed dislocation interacts with a (10$\bar{1}$1) twin, it produces products similar to that for a prismatic ⟨ c ⟩ edge dislocation, as shown in MD simulations in Ti conducted by Hooshmand et al. [121]. This interaction gives rise to a glissile TD, a sessile residual interfacial defect, and a basal ⟨ a ⟩ mixed dislocation, under sole shear strain. However, accroding to crystallographic relationship between the matrix and a (10$\bar{1}$1) twin, Yoo [36] and Niewczas [108] suggested that a pyramidal ⟨ $c + a$ ⟩ dislocation in the matrix, with its slip plane of (10$\bar{1}$1) that is same to the twinning plane, can cross-slip to the (10$\bar{1}$1) pyramidal plane in the twin crystal without producing any defect on the lattice or twin boundary.

3.2.3. *Effect of* {10$\bar{1}$1} *twin and dislocation interactions on plastic deformation*

In Mg, c-axis compression can be partially relieved by the activation of (10$\bar{1}$1) twins. Under this loading condition, secondary (10$\bar{1}$2) extension twins can immediately nucleate inside a resultant (10$\bar{1}$1) twin, forming a (10$\bar{1}$1)-(10$\bar{1}$2) double twin structure [10-12,43]. The double-twinned region is favorably orientated for basal slip, leading to intensive basal slip activity within the contraction twins and the double twins. This localized shear can make the twin-matrix interface be a potential crack initiation site, eventually leading to fracture failure [46,47,49,50,130]. Different types of dislocations interacting with a (10$\bar{1}$1) twin always produce glissile two-atomic-layer-height TDs, which facilitate the twin boundary migration and effectively release local stress concentrations on the twin boundary, thus retard twin boundary cracking. In addition, the interactions can produce different types of dis-

connections, which can release local lattice strain by further reacting with other lattice dislocations [123], thus contributing to the plastic deformation. Similar to the $(10\bar{1}2)$ twin-dislocation interactions, the $(10\bar{1}1)$ twin-dislocation interactions can also generate different types of stacking faults inside the twin, these stacking faults can act as obstacles against dislocations gliding other slip systems and therefore provide strain hardening in Mg.

4. Twin-twin interactions

4.1. $\{10\bar{1}2\}$ *twin-twin interaction*

There are six equivalent variants of $\{10\bar{1}2\}$ twin, denoted as T_i with subscript i changing from 1 to 6 following a counter-clockwise rotation about the c-axis, as shown in Fig. 17a. The interaction between an incoming T_i and an encountering T_j is denoted as $T_i \rightarrow T_j$. Three crystallographically different twin-twin interactions can occur, including $T_1 \rightarrow T_2$, $T_1 \rightarrow T_3$ and $T_1 \rightarrow T_4$ as illustrated in Figs. 17b-d. The $T_1 \rightarrow T_4$ interaction is termed Type I co-zone twin-twin interaction, as T_1 and T_4 share the same a-axis of $[1\bar{2}10]$. In contrast, T_1 and T_2 or T_1 and T_3 interactions are referred to as Type II non-co-zone twin-twin interaction, with Type II(a) for $T_1 \rightarrow T_2$, and Type II(b) for $T_1 \rightarrow T_3$ [39].

TTBs form when one twin encounters another twin. Fig. 18 shows three possible mechanisms: impinging, zipping, and dissociating corresponding to the motion, and reactions of TDs. In the impinging mechanism, the front tip of T_i is blocked at the boundary of T_j. In the zipping mechanism, TDs associated with T_i and T_j react to form TTJs. In the dissociating mechanism, a TD of one twin dissociates into a TD of the other twin and leaves a junction. TTBs are classified into three types: TTB_A, TTB_O, and TTB_I according to the angle between two twin planes. As shown in Fig. 18, TTB_A refers to a TTB with an acute angle between the twinning planes of T_i and T_j. TTB_O refers to a TTB with an obtuse angle between the twinning planes of T_i and T_j. TTB_I is parallel to the twinning plane of the encountering twin [39].

For Type I twin-twin interaction, TTBs generally share low-index close packed planes. Corresponding to the near 90° rotation associated with $\{10\bar{1}2\}$ twinning, two co-zone twin variants share a near 180° rotation, forming two tilt boundaries, a basal‖basal (BB) boundary bonding the basal planes in the incoming and encountering twins (referred to as TTB_O in Mg), and a prismatic‖prismatic (PP) boundary bonding the prismatic planes in the two twins (referred to as TTB_A in Mg) [39]. Misfit dislocations form along the BB or PP boundaries to compensate the misorientation of two twin variants, for example 7.4° in Mg. The Burgers vector content of misfit dislocations along the formed PP or BB boundary is equal to the sum of the Burgers vectors of the two twinning dislocations ($\mathbf{b_t}$) of the interacting two twins. The BB or PP boundaries have frequently been observed in experiments, as shown in Fig. 19, [131,132] and their formation mechanisms are examined in detail using MD simulation in Mg [133].

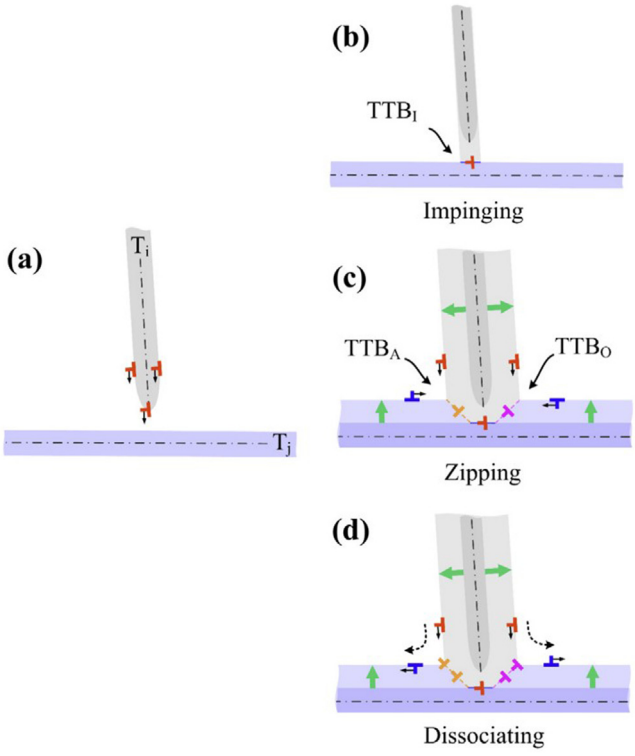

Fig. 18. Approach of T_i to the pre-existing T_j twin in (a) gives rise to the formation of TTBs through three mechanisms, including (b) the impinging mechanism, (c) the zipping mechanism and (d) the dissociating mechanism. The TDs are drawn in red and blue for T_i and T_j twins, and the TTB dislocations are drawn in orange and pink colors. TTB_I in (a) refers to a TTB parallel to the twinning plane of the T_j. TTB_A or TTB_O in (c) refers to a TTB with an acute or obtuse angle between the twinning planes of T_i and T_j [39].

TTBs resulting from Type II twin-twin interactions often adopt a high-index crystallographic plane. In a Type II(a) interaction, the TTB_O plane bonds $(\bar{9}\ 19\ \overline{10}\ 18)_{T1}$ plane in T_1 and $(\overline{19}\ 9\ 10\ \overline{18}\ )_{T2}$ plane in T_2, parallel to $(1\bar{1}00)_M$ plane in matrix; the TTB_A plane bonds $(31\ 20\ \overline{51}\ 62\ )_{T1}$ and $(20\ 30\ \overline{51}\ 62)_{T2}$, parallel to $(\bar{1}\bar{1}24)_M$ in matrix; and the TTB_I plane bonds $(\bar{1}012)_{T1}$ and $(15\ 8\ \overline{23}\ \overline{16})_{T2}$, parallel to $(\bar{1}012)_M$ in matrix. In a Type II(b) interaction, the TTB_O plane bonds $(\bar{2}\ 5\ \bar{3}\ 14)_{T1}$ and $(\bar{2}\ \bar{3}\ 5\ \overline{14}\ )_{T3}$, parallel to $(2\bar{1}\bar{1}0)_M$ in matrix; the TTB_A plane bonds $(8\ 8\ \overline{13}\ \bar{6}\ )_{T1}$ and $(\bar{8}\ 13\ \bar{5}\ \bar{6}\ )_{T3}$, parallel to $(0\bar{1}14)_M$ in matrix; and the TTB_I plane bonds $(\bar{1}012)_{T1}$ and $(\bar{3}\bar{8}54)_{T3}$ plane, parallel to $(\bar{1}012)_M$ plane in matrix [40]. The boundary dislocations for TTB_O, TTB_A and TTB_I are donated $\mathbf{b_O}$, $\mathbf{b_A}$, and $\mathbf{b_I}$. $\mathbf{b_O}$ or $\mathbf{b_A}$ is equal to the sum of the Burgers vectors of the two TDs ($\mathbf{b_t}$) of the two interacting twins, and $\mathbf{b_I}$ is equal to the Burgers vector of the TD of the incoming twin. For Type II(a) or Type II(b) interaction, $|\mathbf{b_O}|^2 < 2|\mathbf{b_t}|^2$, $|\mathbf{b_A}|^2 > 2|\mathbf{b_t}|^2$, and $|\mathbf{b_I}|^2 = 2|\mathbf{b_t}|^2$, indicating that the formation of TTB_O is energetically favored while TTB_A is unfavored in Type II(a) or Type II(b) interaction. However, the experimental observations made by Gong et al. [40] showed that neither TTB_O nor TTB_A can form for Type II(b) interaction. MD simulations were used to explain this observation, showing that the local

Please cite this article as: Y. Yue, J. Wang and J.-F. Nie, Twin-solute, twin-dislocation and twin-twin interactions in magnesium, Journal of Magnesium and Alloys, https://doi.org/10.1016/j.jma.2023.07.015

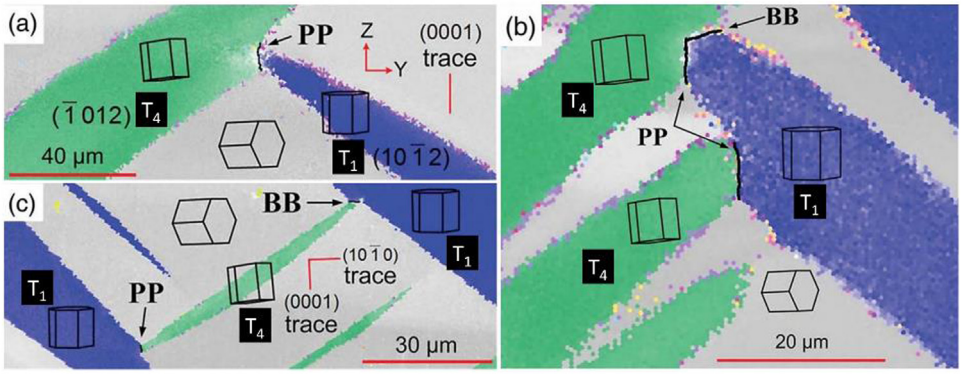

Fig. 19. High-magnification crystal orientation maps showing low-angle PP and BB twin-twin boundaries formed between T_1 and T_4 twins. The gray, blue and green regions indicate the parent, T_1 and T_4 domains, respectively. The wire-frame unit cell depicted in (a-c) indicates the crystal orientation [41].

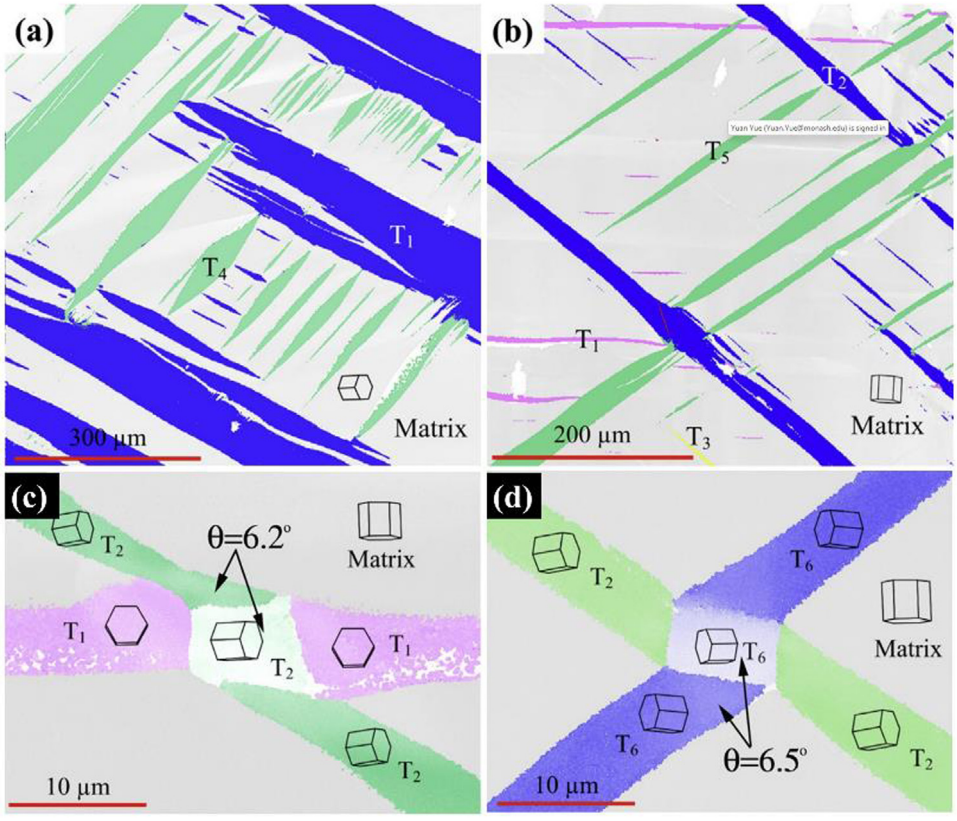

Fig. 20. (a-b) Quilted-looking twin structures in samples loading along (a) $[\bar{1}011]$ and (b) [0001] directions. (c-d) "Apparent crossing" twin structures in samples loading along [0001] direction [39].

stress field does not favor the formation of TTB_O or TTB_A for Type II(b) interaction. In this case, the growth of incoming and encountering twins is impeded on both obtuse and acute sides [40]. The observation of the twin growth behavior for a Type II(b) interaction in Gong et al. [40] is inconsistent with that in the work of Chen et al. [134], in which both twins are found to continue to migrate on the acute side but cease to migrate on the obtuse side. This disagreement is attributed to the difference in the 2D cross-section applied in the two studies, which was subsequently explained in the 3D atomic simulations work of Dang et al. [135].

Due to cyclic loading or strain path change during material forming, multiple $\{10\bar{1}2\}$ twin variants are activated and interact with each other, consequently forming twin-twin structures. These twin-twin structures can be classified into three types based on microstructural features: quilted-looking twin structure, "apparent crossing" twin structure, and double extension twin structure [39]. The quilted-looking twin structure, as shown in Figs. 20a and b, forms due to the propagation and blocking of multiple twin variants. The "apparent crossing" twin structure, as shown in Figs. 20c and d, is different from the crossing twin structure that has an impinging twin

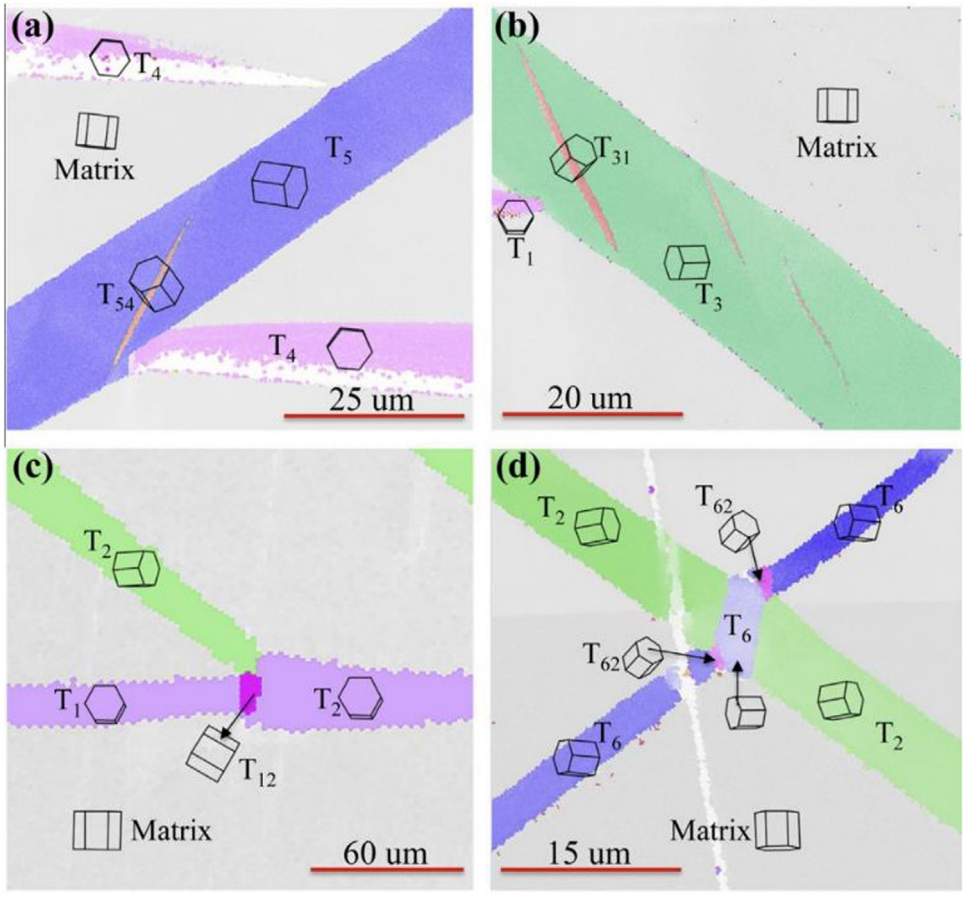

Fig. 21. Double extension twin structures in the sample loading along [0001] direction, with secondary twin in (c) not connected to an incoming twin and in (d) connected to TTBs [39].

crossing the encountering twin through a secondary twinning path. Experimental observations and theoretical analyses have shown that $\{10\bar{1}2\}$ twins cannot transmit into one another. In the "apparent crossing" twin structure, the crystal in the intersection region actually belongs to one of the variants of the interacting twins but experiences a small tilt due to the formation of dislocations at the TTBs. The double extension twin structure, Fig. 21, has a secondary twin forming inside a primary twin, and this secondary twin may or may not connect to another twin that has interacted with the primary twin. In this case, the secondary twin forms due to either a change in the loading condition, or the local stresses induced by the twin that interacts with the primary twin.

Once a twin is blocked by the other twin, TDs associated with the incoming twin are blocked at the pre-existing twin boundary, and boundary dislocations form and pile up at TTBs. The back-stress associated with the dislocations pile-up at TTBs hinders the motion of TDs towards the TTB, requiring a high stress for further growth and propagation of twins and thus giving rise to strain hardening [39]. Upon detwinning, TTB dislocations are expected to dissociate into TDs. However, the dissociation is energetically unfavorable, hindering detwinning. Additionally, the reverse loading promotes the formation of secondary twins from TTBs, which suppresses detwinning of the primary twin. Therefore, higher stress and strain hardening rate are observed during detwinning than those during twinning. With the increasing loading cycles, more TTBs form, and both twinning and detwinning become harder. This causes an increase in flow stresses for tension and compression, resulting in cyclic hardening [39].

The TTBs that form in Type I twin-twin interactions have a low misorientation angle, which facilitates easy slip transmission between the nearly parallel glide planes of the two twins [39]. This is especially true for the easily activated basal slip, which can cross the PP boundary between the two twin variants, forming basal slip bands with emission of basal dislocation from the PP boundary [41]. In contrast, TTBs that form in Type II twin-twin interactions have a large misorientation angle. The glide planes of the two twins are not parallel, making slip transmission between them difficult.

4.2. $\{10\bar{1}1\}$ *twin-twin interactions*

$\{10\bar{1}1\}$ twin has six equivalent variants, designated C_{1-6}, with subscript i changing from 1 to 6 following a counter-clockwise rotation about the c-axis, as shows in Fig. 22a. Correspondingly, three types of twin-twin interaction can occur between an incoming C_i and an encountering C_j, denoted as $C_1 \rightarrow C_2$, $C_1 \rightarrow C_3$ and $C_1 \rightarrow C_4$. The $C_1 \rightarrow C_4$ inter-

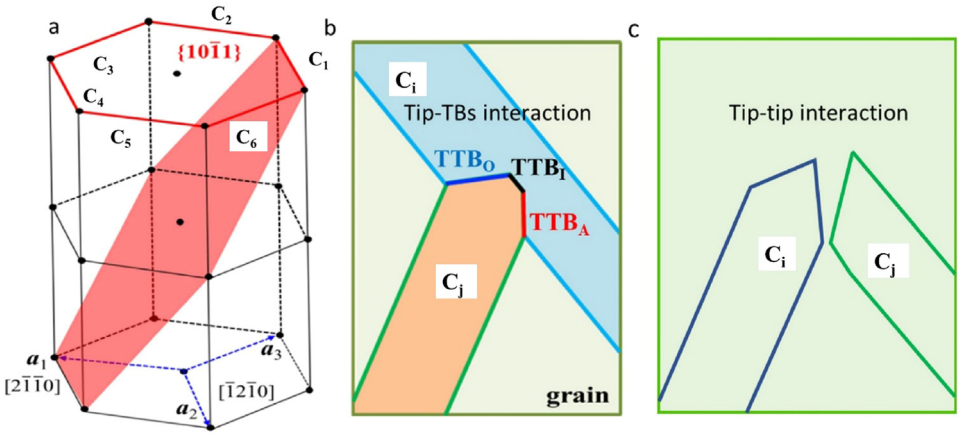

Fig. 22. (a) Six crystallographically equivalent $\{10\bar{1}1\}\langle\bar{1}012\rangle$ twin variants C_i (i = 1–6) in a hcp crystal. Schematic illustration of (b) tip-twin boundaries and (c) tip-tip interactions. TTB_A (marked by red) and TTB_O (marked by blue) in (b) forms on acute and obtuse sides on twin-twin junctions [136].

action is a co-zone twin-twin interaction, while $C_1 \rightarrow C_2$ or $C_1 \rightarrow C_3$ is a non-co-zone twin-twin interaction [136].

Three types of TTBs can form associated with $\{10\bar{1}1\}$ twins interactions, including TTB_A, TTB_O and TTB_I. TTB dislocations on TTB_O, TTB_A and TTB_I are designated $\mathbf{b_O}$, $\mathbf{b_A}$, and $\mathbf{b_I}$, respectively, where $\mathbf{b_O}$ or $\mathbf{b_A}$ is equal to the sum of the Burgers vector of the two TDs ($\mathbf{b_t}$) of the two intersected twins, $\mathbf{b_I}$ is equal to the Burgers vector of the TD of the incoming twin. For all three types of $\{10\bar{1}1\}$ twins interactions, $|\mathbf{b_O}|^2 > 2|\mathbf{b_t}|^2$ and $|\mathbf{b_A}|^2 < 2|\mathbf{b_t}|^2$ in Mg implies the preferable formation of TTB_A than that of TTB_O [136].

Peng et al. [136] investigated two interaction modes for $C_1 \rightarrow C_4$ co-zone twin-twin interactions in Mg. The first interaction mode is the acute collision between the tip of the incoming twin and the twin boundary of the encountering twin (Fig. 22b), with three stages observed in MD simulations shown in Fig. 23. The first stage corresponded to the impingement of the front tip of C_4 at the boundaries of C_1. The second stage was the zipping process with two twins reacting to form TTBs, in which TTB_A related to the $\{10\bar{1}3\}$ TB and TTB_O mainly composed of $\{10\bar{1}1\}$ TB formed. The third stage was the transverse crossing of C_4 through the C_1, which is different from the "apparent crossing" (no transmission of one twin into the other) observed in $\{10\bar{1}2\}$ and $\{10\bar{1}2\}$ twin-twin interactions. The second interaction mode is the acute tip-tip interaction (Fig. 22c) between two twin variants. With the tip-tip collision, steps on the twin boundaries and a large number of basal SFs inside the twins were generated, and $\{10\bar{1}3\}$ discontinuous interfaces were detected in the junction of the two twin variants, as shown in Fig. 24. The simulation result was then confirmed in the TEM observation, in which smooth $\{10\bar{1}1\}$ TB along TTB_A direction and multi-layer steps along TTB_O direction were found for tip-twin boundary interaction, and a new $\{10\bar{1}3\}$ TB interface between the tips of two interacting $\{10\bar{1}1\}$ twins was observed for tip-tip interaction, Fig. 25.

The contact and reaction of two $\{10\bar{1}1\}$ twin variants impede the twin boundary migration through the formation of TTBs and pile-up of boundary dislocations, leading to increased flow stress and strain hardening. Besides, $\{10\bar{1}1\}$ TTBs always show complex structures that comprise multi-layer steps or discontinuous interfacial defects [136]. Localized strain created around these interfacial defects can produce severe strain zone, which may induce the nucleation of cracks at TTBs, causing crack failure along the boundaries [137].

Dense basal SFs are observed during $\{10\bar{1}1\}$ and $\{10\bar{1}1\}$ twin-twin interactions. The formation of these SFs can relax the un-equilibrium boundary structures or release the strain at the interfacial defects [136]. These SFs always cut through the twin lamer, which is identical to divide a grain to smaller sizes and thus give a strengthening effect. Besides, the sessile basal SFs can be obstacles to other slip systems inside the twin, contributing to strain hardening during the further deformation.

4.3. $\{10\bar{1}2\}$-$\{10\bar{1}2\}$ *double twin*

The $\{10\bar{1}2\}$-$\{10\bar{1}2\}$ double twin structures refer to a $\{10\bar{1}2\}$ twin forming inside a primary $\{10\bar{1}2\}$ twin. The $\{10\bar{1}2\}$ secondary twins are always located at the intersections of two $\{10\bar{1}2\}$ twin variants, and the formation of secondary twins can minimize the strain incompatibility caused by different twin variants [13,138,139]. The primary twin within which the secondary twin (ST) forms is termed recipient primary twin (RPT), the twin that intersects with the RPT and connects the ST at the RPT boundary is called intersecting primary twin (IPT). The IPT, RPT and ST twin variants compose an IPT-RPT-ST configuration, as shown in Fig. 26, in which IPT and ST form an adjoining twin pair.

The nucleation of secondary twin can be attributed to the local stress concentration induced by twin-twin interaction. Since twin-twin interactions can occur between T_2 and T_1, T_3 and T_1, or T_4 and T_1, there are three types of IPT-RPT intersections. For each type of intersection, only one ST variant has its twin plane intersecting twin planes of IPT and RPT at a common line, so three possible IPT-RPT-ST configurations can form [140]. Define the secondary twin vari-

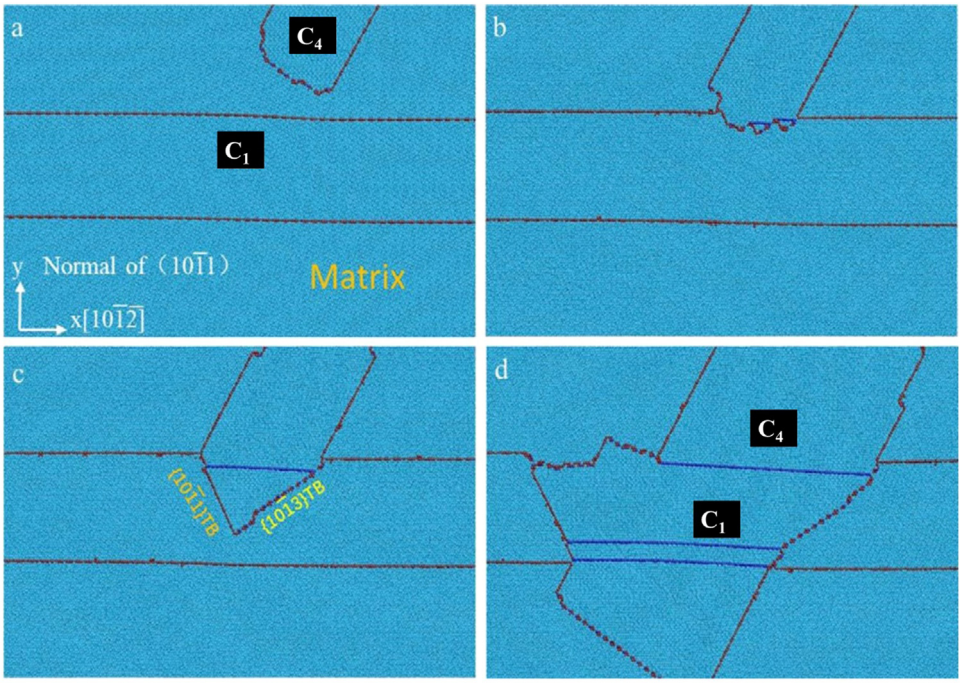

Fig. 23. Interaction between the tip of C_4 and the twin boundary of C_1 in MD simulations. The interfaces associated with both {10$\bar{1}$1} and {10$\bar{1}$3} TBs are formed during the twin-twin reaction [136].

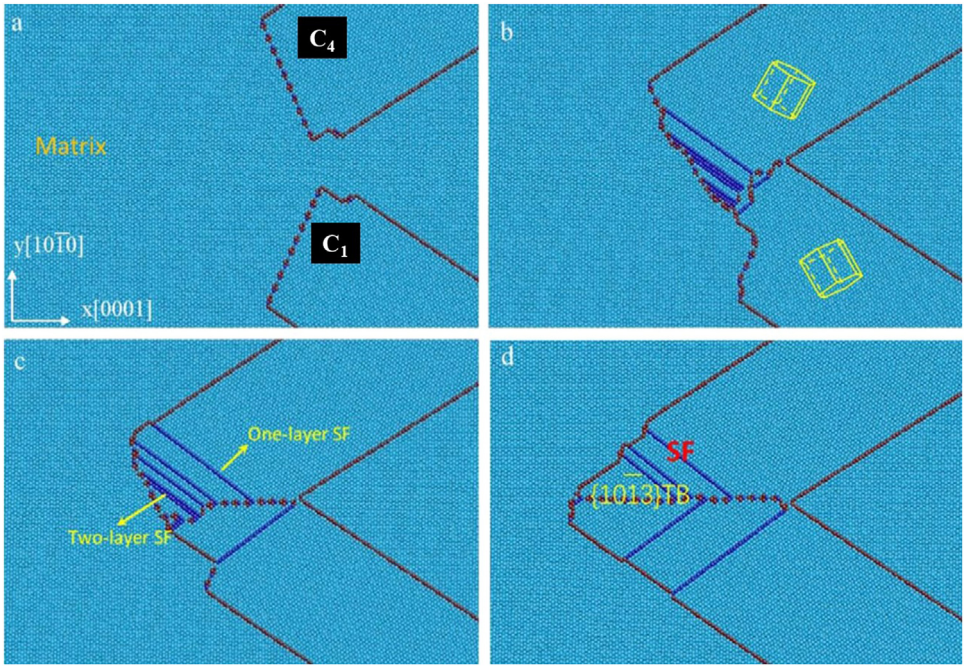

Fig. 24. Tip-tip interaction between C_1 and C_4 twins in MD simulations. The SFs are formed inside twins during the twin-twin reaction [136].

ant that forms in RPT T_i as T_{ij}, the three possible configurations are T_2-T_1-T_{12} (Type I), T_3-T_1-T_{13} (Type II) and T_4-T_1-T_{14} (Type III). Characters associated with the three types of IPT-RPT-ST configurations, such as misorientation angles between IPT and RPT, IPT and ST, are listed in Table 2. Liu et al. [140] observed that most of the IPT-ST pairs in deformed Mg (single crystal pure Mg or polycrystalline AZ31) samples are Type I, which agrees well with the previous experimental observations in the work of Xin et al.[138], Shi et al. [141], and Roberts and Partridge [142].

The stress field generated by the pre-existing twin of IPT or ST and mainly concentrated at the rim of the twin, was suggested by Liu et al. [140] to play the most important role in determining the formation of ST or IPT to generate a twin

Please cite this article as: Y. Yue, J. Wang and J.-F. Nie, Twin-solute, twin-dislocation and twin-twin interactions in magnesium, Journal of Magnesium and Alloys, https://doi.org/10.1016/j.jma.2023.07.015

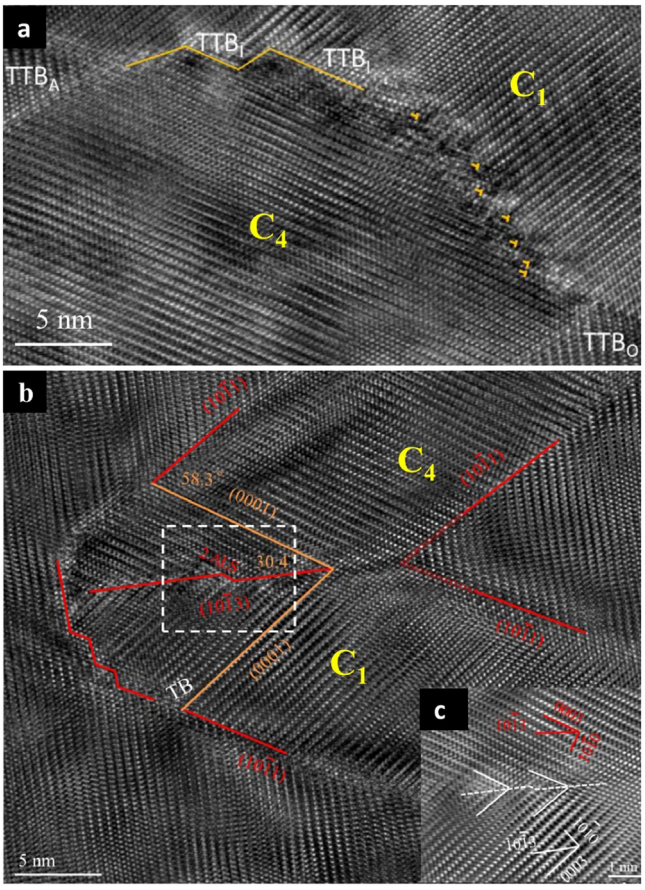

Fig. 25. High magnification TEM image of (a) twin-twin transverse crossing structure formed from the tip-twin boundary interaction, and (b) tip-tip structure formed from the tip-tip interaction. The FFT image of twin-twin interface in (b) is shown in (c) [136].

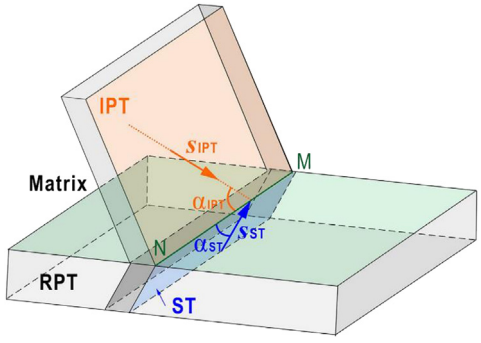

Fig. 26. Schematic diagram showing the IPT-RPT-ST configuration. The twin planes of the intersecting primary twin (IPT), recipient primary twin (RPT) and secondary twin (ST) are coloured in orange, green and blue, respectively [140].

pair. The influence of the stress field of IPT/ST on nucleation of ST/IPT is tiny when the intersection line between twin planes of IPT and RPT is different from that between twin planes of RPT and ST, in which situation twin planes of IPT-ST pairs only have a point contact, e.g., T_2-T_{14} pairs shown in Fig. 27a. The influence of the stress field is much more effective when twin planes of IPT, RPT and ST intersect at the same line, and can be evaluated by calculating the interaction energy between the stress field induced by the pre-existing twin and the stress-free transformation strain (SFTS) of the to-be-formed twin [140]. It was found that the stress field induced by IPT T_2 or ST T_{12} favored the formation of ST T_{12} or IPT T_2, with negative interaction energy value calculated, Fig. 27b. In this case, the pre-existing stress was relaxed, and T_2-T_{12} pair formed favorably with the decrease of the total elastic strain energy. In contrast, the interaction energy between the stress field of T_3 and SFTS of T_{13}, and between the stress field of T_4 and SFTS of T_{14} were both positive, Figs. 27c and d. This means that T_{13} or T_{14} cannot relax the pre-existing stress induced by T_3 or T_4, and the formation of T_3-T_{13} or T_4-T_{14} pair was not favored. The situation is the same when T_{13} or T_{14} form prior to T_3 or T_4. These calculations suggest that the Type II T_3-T_1-T_{13} and Type III T_4-T_1-T_{14} configuration are unfavored to form, and well explain the frequent observation of the Type I T_2-T_1-T_{12} structure in experiments. Liu et al. [140] suggested that the back-stress inside RPT and the external applied stress also affect the variant selection for the formation of IPT-ST twin pairs. However, their influence is less significant than the pre-existing stress field concentrated at the rim of IPT. In contrast to the pre-existing stress concentrated only on a local region, the back-stress or external stress is uniformly distributed in the whole RPT or whole sample, thus they play important roles in influencing the growth of secondary and primary twins. Besides, it was found that the external stress could affect the appearance frequency of a specific IPT-ST pair after the ST variant is determined.

Table 2
Crystallographic features of the three IPT-RPT-ST configurations including Types I, II and III, with examples T_2-T_1-T_{12}, T_3-T_1-T_{13} and T_4-T_1-T_{14}, respectively [140].

Configuration	I	II	III
IPT-RPT-ST	T_2-T_1-T_{12}	T_3-T_1-T_{13}	T_4-T_1-T_{14}
Intersection line	$[4\bar{2}\bar{2}3]$	$[\bar{2}201]$	$[1\bar{2}10]$
Misorientation IPT-RPT	$60.0°\langle\bar{1}2\ 12\ 0\ 1\rangle$	$60.4°\langle\bar{7}8\bar{1}0\rangle$	$7.4°\langle\bar{2}110\rangle$
Misorientation IPT-ST	$49.6°\langle\bar{9}904\rangle$	$37.9°\langle\bar{2}201\rangle$	$78.9°\langle\bar{1}2\bar{1}0\rangle$
m' (IPT-ST)	−0.1525	−0.0988	−0.9832

Secondary extension twins in a $\{10\bar{1}2\}$-$\{10\bar{1}2\}$ double twin structure are very fine, and the growth of the secondary twins is appearing to be limited [13]. Since the thickness of a twin lamella plays a similar role as that of the grain size, smaller size of $\{10\bar{1}2\}$ secondary twins are beneficial to enhance the strength [42]. However, thin secondary twin laminas may relate to the fracture failure, as they are observed to occur with a large number density in the crack initiation and propagation regions after the cyclic deformation of a Mg alloy [139]. The macrocrack surfaces usually orient along the secondary twin boundaries, and the associated fracture mechanism was explained by Tan and Zhang et al. [143] as follow: the primary $\{10\bar{1}2\}$ twin boundaries were smooth and long while the secondary $\{10\bar{1}2\}$ twin boundaries were short and fragmented, therefore, the growth of the secondary twins inside a primary twin causes severe deformation incompatibility as the num-

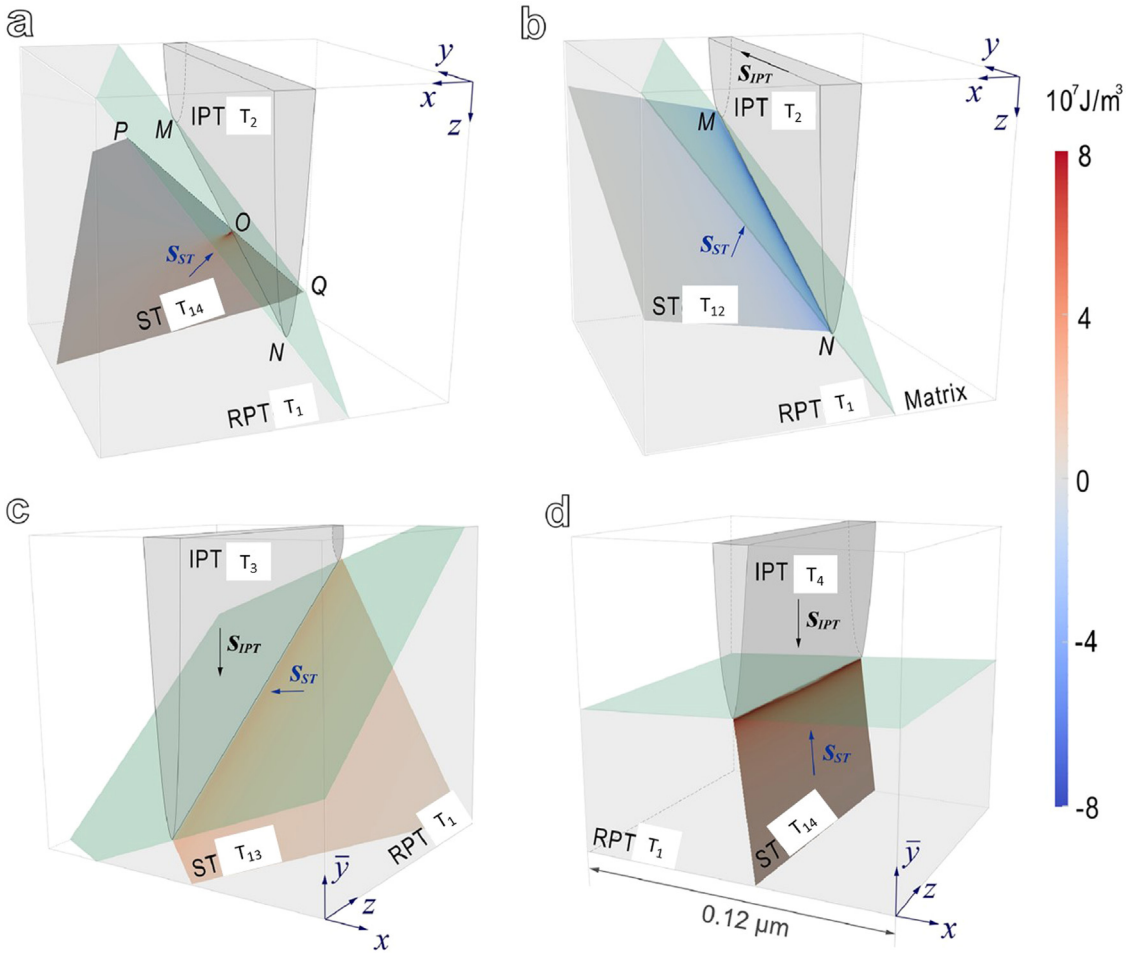

Fig. 27. Distribution of the interaction energy between IPT and ST on the twin plane of ST in the twin-twin intersection region of IPT and RPT. The IPT, RPT and ST are T_2, T_1 and T_{14} in (a); T_2, T_1 and T_{12} in (b); T_3, T_1 and T_{13} in (c) and T_4, T_1 and T_{14} in (d). Both IPT and RPT crystals are in gray color and the twin plane of RPT is coloured in light green. Values of the interaction energy are represented by the scale bar on the right. s_{IPT} and s_{ST} are twin shear directions of IPT and ST respectively [140].

ber of deformation cycles increases, and cracks initiate and develop along the $\{10\bar{1}2\}$-$\{10\bar{1}2\}$ secondary twin boundaries when the twin boundaries no longer accommodated the localized stress concentrations. Apart from enhancing strength or inducing fracture, secondary twinning can compete with the detwinning of the primary extension twin, and it was reported that a secondary twin can serve as the barrier to suppress the detwinning if it has separated the primary twin from the matrix [42].

4.4. $\{10\bar{1}1\}$-$\{10\bar{1}2\}$ *double twin*

The $\{10\bar{1}1\}$-$\{10\bar{1}2\}$ double twin structure refers to the formation of $\{10\bar{1}2\}$ extension twin inside the primary $\{10\bar{1}1\}$ twin This is the most frequently observed double twin mode in Mg and is often activated upon compression along the *c*-axis of Mg crystal. For six $\{10\bar{1}2\}$ secondary twin variants, four types $\{10\bar{1}1\}$-$\{10\bar{1}2\}$ double twin structures can be defined because secondary twinning on planes B and F, or C and E cause equivalent misorientations between the matrix and the $\{10\bar{1}2\}$ twin [44], as illustrated in a pole figure in Fig. 28. Type 1–4 correspond to the labelled letters D, A, B(F), and C(E), respectively. The misorientation relationships between the secondary twin variant and the matrix are illus-

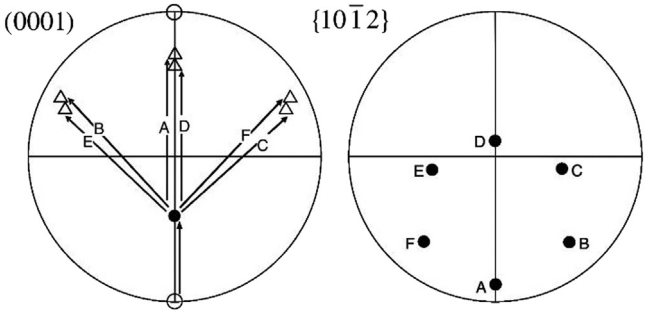

Fig. 28. (a) Reorientation of the basal poles during $\{10\bar{1}1\}$-$\{10\bar{1}2\}$ double twinning, the open circles represent the original orientation, the closed circles refer to the reoriented basal poles produced after a given primary $\{10\bar{1}1\}$ twinning and the triangles represent the reoriented basal poles produced by secondary $\{10\bar{1}2\}$ twinning that have six variants. (b) The orientations caused by six $\{10\bar{1}2\}$ twinning variants after primary $\{10\bar{1}1\}$ twinning are tracked with the letters A-F [44].

Table 3
Illustration of four misorientation relations between the matrix and six secondary twin variants (A-F labelled in Fig. 2 in Ref. [44]) after $\{10\bar{1}1\}$-$\{10\bar{1}2\}$ double twinning [44].

Double twin type	1	2	3	4
Secondary twin variants	D	A	B and F	C and E
Misorientation relation	37.5° $\langle 1\bar{2}10\rangle$	30.1° $\langle 1\bar{2}10\rangle$	66.5° $\langle 5\bar{9}43\rangle$	69.9° $\langle 2\bar{4}21\rangle$

Table 4
Angles between primary $\{10\bar{1}1\}$ and secondary $\{10\bar{1}2\}$ twins for four types of $\{10\bar{1}1\}$-$\{10\bar{1}2\}$ double twin structures [44].

Double twin type	1	2	3	4
Angle between primary and secondary twins	18.8°	74.9°	87.6°	49.9°

trated in Table 3, it is seen that secondary twin in Type 1 and 2 structure share the same zone axis $\langle 1\bar{2}10\rangle$ with the primary twin, while in Type 3 and 4 structure does not [144]. Experimental observations showed that Type 1 double twin structure that involves a crystallographic rotation of 37.5° around $\langle 1\bar{2}10\rangle$ is much more favored to form than the other three types [44,46,49,145].

The predominant occurrence of Type 1 double twin structure can be explained based on strain accommodation [44,45,145]. It is noted that the lateral growth of secondary $\{10\bar{1}2\}$ twins is restricted by the shape of the primary $\{10\bar{1}1\}$ twin, and the compatibility strain is increased with the growth of the secondary twin. As a result, the greater the angle between the secondary and primary twin planes, the greater the additional compatibility strain; and the higher the compatibility strain, the higher the impediment to secondary twin growth [44,145]. Since the primary and secondary twin planes are significantly closer in Type 1 structure than in other three types, as illustrated in Table 4, Type 1 structure shows the least accommodation strain and the greatest potential for growth of the secondary twin, therefore it is optimal to occur.

The criteria for variant selection based on strain accommodation requires secondary twin to already grow to an appreciable size. Beyerlein et al. [144] explained the predominance of Type 1 structure with considerations of both nucleation and growth, and proposed that nucleation and growth of a secondary twin were achieved through the dissociation of slip dislocations into $\{10\bar{1}2\}$ TDs at the primary $\{10\bar{1}1\}$ twin boundary. Since the intersection line $\langle 1\bar{2}10\rangle$ between primary twin plane and Type 1 or 2 secondary twin plane has only $\langle a \rangle$ component, it is possible for basal $\langle a \rangle$ dislocations to dissociate into Type 1 or 2 secondary TDs. In contrast, the intersection line between primary twin plane and Type 3 or 4 secondary twin plane has both $\langle a \rangle$ and $\langle c \rangle$ components, thus dissociation of properly orientated pyramidal $\langle c + a \rangle$ dislocations is required to form Type 3 or 4 secondary TDs. Since activation and migration of pyramidal $\langle c + a \rangle$ is much more difficult than that of basal $\langle a \rangle$ dislocations, formation of a stable secondary twin nucleus, and later expansion of this twin nucleus through successive dissociation reactions, are much harder for Type 3 and 4 structure, than that for Type 1 and 2 structure. Among four double twin structures, Type 1 secondary twin has twin plane and twinning direction aligned most closely with those of the primary twin. Therefore, the same local stress can support both the growth of the primary and Type 1 secondary twin. In contrast, Type 2–4 must arise from a stress state that does not favor the growth of the primary twin, which could be encouraged if a pile-up of dislocations has formed at the primary twin boundary. The additional requirement for pile-up of basal dislocations may explain the preferable occurrence of Type 1 over the Type 2 structure. When a secondary twin grows to a sizable volume, the favourability of Type 1 over Type 2 structure may also be attributed to the smaller rotation and the larger twin shear involved in Type 1. As for rotation, Type 1 structure leads to a misorientation of 18.8° between the basal planes of the primary and secondary twins, while Type 2 structure leads to a significantly larger misorientation of ~75° As for twin shear, a same-sized double twin band containing a Type 1 secondary twin is able to accommodate the strain as twice as that containing a Type 2 secondary twin. The above advantages taken by the formation of the Type 1 double twin account for its overwhelming occurrence among different structures.

The $\{10\bar{1}1\}$-$\{10\bar{1}2\}$ double twin involving a rotation of 37.5° around $\langle 1\bar{2}10\rangle$ was observed most frequently, and this twin mode was recognized to be closely related to the fracture failure of Mg. Reed-Hill and co-authors firstly reported the $\{30\bar{3}4\}$ twins in relation to fracture planes [10], and later confirmed that this was the $\{10\bar{1}1\}$-$\{10\bar{1}2\}$ double twins to be a fracture initiation site and cause micro-voids form at the twin interfaces [12]. Barnett et al. [44] suggested that $\{10\bar{1}1\}$-$\{10\bar{1}2\}$ double twin in polycrystalline Mg might cause premature shear failure due to the combined effects of strain softening and localized void formation. Ando and Koike [46] observed large surface steps accompanied by the narrow double twin bands, and these steps were suggested to be induced by the localized deformation inside the double twin and could develop to form crack. It is explained that the double-twinned region is re-orientated for easy basal-slip and the enhanced activity of basal slip causes highly localized shear deformation within the double twin [46,47,49,50,130]. The localized shear deformation creates a "soft" region that is inside the twinned volume and surrounded by the "hard" matrix [48]. The severe localized shear is manifested as a large surface relief [46,47] and causes nucleation of cracks within the shear band region [48] or the $\{10\bar{1}1\}$-$\{10\bar{1}2\}$ twin-matrix interface [12,45,46]. These cracks can propagate either intragranular or along the $\{10\bar{1}2\}$ twin-matrix interface, causing premature failure. The sensitivity to fracture failure due to the formation of $\{10\bar{1}1\}$-$\{10\bar{1}2\}$ double twin was suggested to limit the cold formability of Mg and its alloys.

Please cite this article as: Y. Yue, J. Wang and J.-F. Nie, Twin-solute, twin-dislocation and twin-twin interactions in magnesium, Journal of Magnesium and Alloys, https://doi.org/10.1016/j.jma.2023.07.015

4.5. Other double twins

In addition to the frequently reported {10$\bar{1}$2}-{10$\bar{1}$2} and {10$\bar{1}$1}-{10$\bar{1}$2} double twins, there are other double twins in Mg, such as {10$\bar{1}$3}-{10$\bar{1}$2} [10] or {11$\bar{2}$1}-{10$\bar{1}$2} [146] that have been less observed and studied. The reason for the less variety of double twin modes in Mg, than in other hexagonal metals, is that only {10$\bar{1}$2}⟨$\bar{1}$011⟩ twinning can be easily activated, and other types of twinning processes always require specific loading conditions thus are more difficult to occur. Unlike only one active twin mode ({10$\bar{1}$2} twin) in Mg, there are more twinning modes available and occurring in Ti, including {10$\bar{1}$2}, {11$\bar{2}$1} and {11$\bar{2}$3} tension twins, {10$\bar{1}$1}, {11$\bar{2}$2} and {11$\bar{2}$4} compression twins [147–150], which results in the formation of more types of double twin modes. The investigation on the variant selection of secondary twin for different double twin modes in Ti is expected to provide useful guidance for the similar study in Mg. For example, four types of double twin modes have been observed in deformed Ti by Xu et al. [151], which can be classified into co-family double twins include {11$\bar{2}$2}-{11$\bar{2}$1} and {11$\bar{2}$1}-{11$\bar{2}$4} that share the same zone axis, and non-family double twins include {11$\bar{2}$2}-{10$\bar{1}$2} and {11$\bar{2}$4}-{10$\bar{1}$2} that have different zone axes. For convenience, T_i^I and T_i^{II} are used to denote the six {10$\bar{1}$2} and the six {11$\bar{2}$1} tension twin variants, C_i^I and C_i^{II} are used to denote the six {11$\bar{2}$2} and the six {11$\bar{2}$4} contraction twin variants, with i equal to 1–6. According to the misorientation between the secondary twin and the parent, co-family {11$\bar{2}$2}-{11$\bar{2}$1} (C_i^I-T_j^{II}) and {11$\bar{2}$1}-{11$\bar{2}$4} (T_i^{II}- C_j^{II}) double twins can be further categorized into four groups denoted as Group I, II, III, IV; non-family {11$\bar{2}$2}-{10$\bar{1}$2} (C_i^I- T_j^I) and {11$\bar{2}$4}-{10$\bar{1}$2} (C_i^{II}- T_j^I) double twins can be further classified into three groups denoted as Group I, II, III. The geometric characteristics of each of the groups for the four types of double twins are summarized in Table 5. It was shown by Xu et al. [151] that the dominant double twins are C_i^I-T_i^{II} (Group I) and T_i^{II}- C_i^{II} (Group III) for co-family {11$\bar{2}$2}-{11$\bar{2}$1} and {11$\bar{2}$1}-{11$\bar{2}$4} double twins, respectively; and the preferred double twins are C_i^I-T_i^I or T_{i+1}^I (Group II) and C_i^{II}- T_i^I or T_{i+1}^I(Group I) for non-family {11$\bar{2}$2}-{10$\bar{1}$2} and {11$\bar{2}$4}-{10$\bar{1}$2} double twins, respectively.

The selection of the secondary twin variant among the four double twin modes mentioned above can be potentially predicted using the Schmid factor (SF). This factor determines the variant with the highest resolved shear stress by assuming that the local stress is the same as the externally applied stress [152]. However, it is important to note that the local stresses within a grain may differ from the applied stress [153,154]. To address this, an apparent-SF (a-SF) [155] has been proposed to improve the SF rule by considering the local stresses. As mentioned in Section 4.4, Beyerlein et al. [144] assumed that the nucleation of a secondary twin is facilitated by the dissociation of a gliding dislocation at the primary twin boundary. This mechanism can be called the nucleation criterion for secondary twinning based on dislocation dissociation (NDD) and could judge whether a specific secondary twin variant prefer to form from a certain primary twin boundary. Jonas et al. [153] and Shi et al. [156] proposed a displacement gradient accommodation (DGA) criterion, which suggested that a twin variant prefers to nucleate when its deformation can be readily accommodated by slip in the vicinity of the twin domain. In DGA analysis, the displacement gradients induced by the secondary twin variant are resolved into the crystal frame of the parent grain. When considering the minimization of plastic deformation associated with double twinning, a modified DGA (m-DGA) [155] can be applied by transforming the displacement gradients into the twinning reference frame of the primary twin.

In the case of the dominant double twins C_i^I-T_i^{II} or T_i^{II}- C_i^{II} in the co-family {11$\bar{2}$2}-{11$\bar{2}$1} or {11$\bar{2}$1}-{11$\bar{2}$4}, the NDD and m-DGA analysis conducted by Xu et al. [151] suggested that only one secondary twin variant prevails over others for a given primary twin. In contrast, a-SF and DGA analyses can only provide the information about the relative possibilities among the six variants, without predicting a preferred one. For the preferred double twins C_i^I-T_i^I or T_{i+1}^I and C_i^{II}-T_i^I or T_{i+1}^I in the non-family {11$\bar{2}$2}-{10$\bar{1}$2} and {11$\bar{2}$4}-{10$\bar{1}$2}, Xu et al. [151] reported that the selection between the two variants follows the SF rule. Both the NDD and m-DGA criteria can effectively predict the prevailing secondary twin variants. The a-SF could help determine the competition of the two prevailing double twin variants, while the DGA fails to pre-

Table 5
Geometric characters for different variants for four types of double twin modes observed in Ti [151].

Secondary twin	Misorientation	Group	Nomination
(11$\bar{2}$2)[11$\bar{2}\bar{3}$]-{11$\bar{2}$1} double twins (Co-family)			
(11$\bar{2}$1)[$\bar{1}\bar{1}$26]	29.5° ⟨1$\bar{1}$00⟩	I	C_i^I-T_i^{II}
($\bar{1}$2$\bar{1}$1)[1$\bar{2}$16]	55° ⟨$\bar{1}$0 5 5 $\bar{3}$⟩	II	C_i^I-T_{i+1}^{II}
($\bar{2}$111)[2$\bar{1}\bar{1}$6]	86.8° ⟨$\bar{1}$5 10 5 $\bar{3}$⟩	IV	C_i^I-T_{i+2}^{II}
($\bar{1}\bar{1}$21)[$\bar{1}\bar{1}$26]	80.6° ⟨1$\bar{1}$00⟩	III	C_i^I-T_{i+3}^{II}
(12$\bar{1}$1)[$\bar{1}$2$\bar{1}$6]	86.8° ⟨$\bar{1}$5 10 5 $\bar{3}$⟩	IV	C_i^I-T_{i+4}^{II}
(2$\bar{1}\bar{1}$1)[$\bar{2}$116]	55° ⟨$\bar{1}$0 5 5 $\bar{3}$⟩	II	C_i^I-T_{i+5}^{II}
(11$\bar{2}$1)[$\bar{1}\bar{1}$26]-{11$\bar{2}$4} double twins (Co-family)			
(11$\bar{2}$4)[22$\bar{4}\bar{3}$]	68.2° ⟨1$\bar{1}$00⟩	III	T_i^{II}-C_i^{II}
($\bar{1}$2$\bar{1}$4)[2$\bar{4}\bar{2}\bar{3}$]	88.3° ⟨$\bar{3}\bar{5}$ 10 25 9⟩	IV	T_i^{II}-C_{i+1}^{II}
($\bar{2}$114)[$\bar{4}$22$\bar{3}$]	65.6° ⟨6 $\bar{1}\bar{0}$ 4 3⟩	II	T_i^{II}-C_{i+2}^{II}
($\bar{1}\bar{1}$24)[$\bar{2}\bar{2}\bar{4}\bar{3}$]	41.9° ⟨1$\bar{1}$00⟩	I	T_i^{II}-C_{i+3}^{II}
(12$\bar{1}$4)[24$\bar{2}\bar{3}$]	65.6° ⟨6 $\bar{1}\bar{0}$ 4 3⟩	II	T_i^{II}-C_{i+4}^{II}
(2$\bar{1}\bar{1}$4)[4$\bar{2}\bar{2}\bar{3}$]	88.3° ⟨$\bar{3}\bar{5}$ 10 25 9⟩	IV	T_i^{II}-C_{i+5}^{II}
(11$\bar{2}$2)[11$\bar{2}\bar{3}$]-{10$\bar{1}$2} double twins (Non-family)			
(10$\bar{1}$2)[$\bar{1}$011]	48.4° ⟨$\bar{5}$503⟩	II	C_i^I-T_i^I
(01$\bar{1}$2)[0$\bar{1}$11]	48.4° ⟨$\bar{5}$503⟩	II	C_i^I-T_{i+1}^I
($\bar{1}$102)[1$\bar{1}$01]	87.9° ⟨7$\bar{4}\bar{3}$0⟩	III	C_i^I-T_{i+2}^I
($\bar{1}$012)[10$\bar{1}$1]	41.3° ⟨5$\bar{1}\bar{4}\bar{3}$⟩	I	C_i^I-T_{i+3}^I
(0$\bar{1}$12)[01$\bar{1}$1]	41.3° ⟨5$\bar{1}\bar{4}\bar{3}$⟩	I	C_i^I-T_{i+4}^I
(1$\bar{1}$02)[$\bar{1}$101]	87.9° ⟨7$\bar{4}\bar{3}$0⟩	III	C_i^I-T_{i+5}^I
(11$\bar{2}$4)[11$\bar{4}\bar{3}$]-{10$\bar{1}$2} double twins (Non-family)			
(10$\bar{1}$2)[$\bar{1}$011]	39.5° ⟨11$\bar{2}\bar{3}$⟩	I	C_i^{II}-T_i^I
(01$\bar{1}$2)[0$\bar{1}$11]	39.5° ⟨11$\bar{2}\bar{3}$⟩	I	C_i^{II}-T_{i+1}^I
($\bar{1}$102)[1$\bar{1}$01]	44.3° ⟨7 20 $\overline{27}$ $\overline{20}$⟩	II	C_i^{II}-T_{i+2}^I
($\bar{1}$012)[10$\bar{1}$1]	89.5° ⟨ $\overline{13}$ $\overline{26}$ 39 4⟩	III	C_i^{II}-T_{i+3}^I
(0$\bar{1}$12)[01$\bar{1}$1]	89.5° ⟨ $\overline{13}$ $\overline{26}$ 39 4⟩	III	C_i^{II}-T_{i+4}^I
(1$\bar{1}$02)[$\bar{1}$101]	44.3° ⟨7 20 $\overline{27}$ $\overline{20}$⟩	II	C_i^{II}-T_{i+5}^I

Table 6
The misorientations (angle/axis) for different types of structures for $\{11\bar{2}1\} \Rightarrow P \rightarrow \{10\bar{1}2\}$ ($T_i^{II} \Rightarrow P \rightarrow T_j^I$) and $\{11\bar{2}2\} \Rightarrow \{11\bar{2}4\} \rightarrow \{10\bar{1}2\}$ ($C_i^I \Rightarrow C_j^{II} \rightarrow T_k^I$) sequential twinning in Ti [157].

Six $\{10\bar{1}2\}$	$\{11\bar{2}1\} \Rightarrow P \rightarrow \{10\bar{1}2\}$		$\{11\bar{2}2\} \Rightarrow \{11\bar{2}4\} \rightarrow \{10\bar{1}2\}$	
	Type	Angle/axis	Type	Angle/axis
$(10\bar{1}2)[\bar{1}011]$	$T_i^{II} \Rightarrow P \rightarrow T_i^I$ (Type A)	66.5° ⟨15 $\bar{5}$ $\overline{10}$ 3⟩	$C_i^I \Rightarrow C_{i+3}^{II} \rightarrow T_i^I$ (Type A)	33.6° ⟨$\bar{9}$546⟩
$(01\bar{1}2)[0\bar{1}11]$	$T_i^{II} \Rightarrow P \rightarrow T_{i+1}^I$ (Type A)	66.5° ⟨15 $\bar{5}$ $\overline{10}$ 3⟩	$C_i^I \Rightarrow C_{i+3}^{II} \rightarrow T_{i+1}^I$ (Type A)	33.6° ⟨45$\bar{9}\bar{6}$⟩
$(\bar{1}102)[1\bar{1}01]$	$T_i^{II} \Rightarrow P \rightarrow T_{i+2}^I$ (Type B)	89.5° ⟨ $\bar{8}$ $\bar{4}$ 12 3⟩	$C_i^I \Rightarrow C_{i+3}^{II} \rightarrow T_{i+2}^I$ (Type B)	67.1° ⟨ $\overline{14}$ 9 5 1⟩
$(\bar{1}012)[10\bar{1}1]$	$T_i^{II} \Rightarrow P \rightarrow T_{i+3}^I$ (Type C)	60.0° ⟨ 66 $\overline{19}$ $\overline{47}$ 14⟩	$C_i^I \Rightarrow C_{i+3}^{II} \rightarrow T_{i+3}^I$ (Type C)	84.3° ⟨3 $\overline{19}$ 16 $\bar{1}$⟩
$(0\bar{1}12)[01\bar{1}1]$	$T_i^{II} \Rightarrow P \rightarrow T_{i+4}^I$ (Type C)	60.0° ⟨ 66 $\overline{19}$ $\overline{47}$ 14⟩	$C_i^I \Rightarrow C_{i+3}^{II} \rightarrow T_{i+4}^I$ (Type C)	84.3° ⟨16 $\overline{19}$ 3 1 ⟩
$(1\bar{1}02)[\bar{1}101]$	$T_i^{II} \Rightarrow P \rightarrow T_{i+5}^I$ (Type B)	89.5° ⟨ $\bar{8}$ $\bar{4}$ 12 3⟩	$C_i^I \Rightarrow C_{i+3}^{II} \rightarrow T_{i+5}^I$ (Type B)	67.1° ⟨5 9 $\overline{14}$ 1⟩

dict the preferred secondary twin variants. The successful predictions made by m-DGA and NDD criteria indicate that the preferred secondary twin variant helps relax the plastic deformation associated with the primary twinning, and the nucleation of the secondary twin is facilitated by the accumulation of gliding dislocations at the primary twin boundary.

4.6. Sequential twinning

In addition to the twin-twin structures discussed in Sections 4.1-4.5, other structures associated with $\{10\bar{1}2\}$ sequential twinning, resulting from the interaction between different types of twins, have also been observed. Xu et al. [157] reported the occurrence of $\{10\bar{1}2\}$ sequential twins that are in the parent (P) grain and along the $\{11\bar{2}1\}$ primary twin boundary, and $\{10\bar{1}2\}$ sequential twins within a $\{11\bar{2}4\}$ primary twin and simulated by the interactions between co-zone $\{11\bar{2}2\}$ twins, both of which were observed in Ti under shock loading. Referring to the $\{10\bar{1}2\}$, $\{11\bar{2}1\}$ and $\{11\bar{2}3\}$ extension twins as T_i^I, T_i^{II} and T_i^{III}, and the $\{11\bar{2}2\}$, $\{11\bar{2}4\}$ and $\{10\bar{1}1\}$ contraction twins as C_i^I, C_i^{II} and C_i^{III} in Ti, the first sequential twinning process can be described as $\{11\bar{2}1\} \Rightarrow P \rightarrow \{10\bar{1}2\}$ or $T_i^{II} \Rightarrow P \rightarrow T_j^I$, and the second sequential twinning process can be described as $\{11\bar{2}2\} \Rightarrow \{11\bar{2}4\} \rightarrow \{10\bar{1}2\}$ or $C_i^I \Rightarrow C_j^{II} \rightarrow T_k^I$. Here, the symbol "⇒" represents the former incoming twin "interacting" with the later primary twin, and "→" represents the former crystal "is twinned" into the later twin. The subscript "i" (or "j", "k") represents the six variants for each twinning mode. The other variants are obtained by rotating the 1st variant (i-1) by 60° about the [0001] axis.

$T_i^{II} \Rightarrow P \rightarrow T_j^I$ twin structures are classified into three types according to the misorientation between T_i^{II} and T_j^I, including Type A $T_i^{II} \Rightarrow P \rightarrow T_i^I$ or T_{i+1}^I, Type B $T_i^{II} \Rightarrow P \rightarrow T_{i+2}^I$ or T_{i+5}^I and Type C $T_i^{II} \Rightarrow P \rightarrow T_{i+3}^I$ or T_{i+4}^I sequential twins. Similarly, $C_i^I \Rightarrow C_j^{II} \rightarrow T_k^I$ twin structures are also categorized into three types, including Type A $C_i^I \Rightarrow C_{i+3}^{II} \rightarrow T_i^I$ or T_{i+1}^I, Type B $C_i^I \Rightarrow C_{i+3}^{II} \rightarrow T_{i+2}^I$ or T_{i+5}^I, and Type C $C_i^I \Rightarrow C_{i+3}^{II} \rightarrow T_{i+3}^I$ or T_{i+4}^I sequential twins. The misorientations (angle/axis) for different sequential twinning modes are listed in Table 6. Experiment photos taken by Xu et al. [157] showed that Type A $T_i^{II} \Rightarrow P \rightarrow T_i^I$ or T_{i+1}^Itwins are most prevailed for $T_i^{II} \Rightarrow P \rightarrow T_j^I$ twin structures; and Type A $C_i^I \Rightarrow C_{i+3}^{II} \rightarrow T_i^I$ or T_{i+1}^I are most predominant for $C_i^I \Rightarrow C_j^{II} \rightarrow T_k^I$ twin structures.

Regarding Type A $T_i^{II} \Rightarrow P \rightarrow T_i^I$ or T_{i+1}^I sequential twins, Xu et al. [157] proposed that their occurrence can be attributed to the presence of twinning disconnections at steps along the twin boundary. In this case, the $\{11\bar{2}1\}$ (T_i^{II}) primary twinning disconnections pile up to form steps along the twin boundaries. Since T_i^I and T_{i+1}^I have the highest resolved shear stress (RSS) in the local stress field associated with the pileup of T_i^{II} TDs, they are most favorably activated by the dissociation of the T_i^{II} TDs at the primary twin boundary. For Type A $C_i^I \Rightarrow C_{i+3}^{II} \rightarrow T_i^I$ or T_{i+1}^Isequential twining, Xu et al. [157] suggested that the nucleation of the $\{10\bar{1}2\}$ sequential twins occurs via slip transformation of the incoming $\{11\bar{2}2\}$ (C_i^I) TDs into the primary $\{11\bar{2}4\}$ (C_{i+3}^{II}) twin. In this case, the T_i^I or T_{i+1}^I $\{10\bar{1}2\}$ variants have the largest RSS in the local stress field associated with the pileup of C_i^I at the C_{i+3}^{II} twin boundaries. These results indicate that the preferred sequential twin variant has the maximum RSS among the six variants, and that the sequential twinning processes obey crystallographic relations based on the ability to accommodate deformation. These results are expected to provide insights for similar studies in Mg.

5. Critical issues remaining to be solved

Extensive research has been conducted on twin-solute interactions in Mg alloys, focusing primarily on those between twin boundary and substitutional solutes. However, there is a lack of studies on interactions between twin boundary and interstitial solutes. A recent DFT [55] work examined the interaction between a $\{10\bar{1}2\}$ twin boundary and H atoms, revealing that H atoms tend to occupy specific tetrahedral sites on the $\{10\bar{1}2\}$ twin boundary. Moreover, they can gather around certain substitutional solutes, leading to hydrogen embrittlement. Nevertheless, other types of interactions, such as

Please cite this article as: Y. Yue, J. Wang and J.-F. Nie, Twin-solute, twin-dislocation and twin-twin interactions in magnesium, Journal of Magnesium and Alloys, https://doi.org/10.1016/j.jma.2023.07.015

those between H atoms and different types of twins (for example, $\{10\bar{1}1\}$), or between twins and other interstitial solutes like O, remain unexplored. Therefore, it is suggested that future work should focus on investigating the various types of twin and interstitial solutes interactions in Mg alloys. This research should delve into the interaction behavior, the preferred atom occupation on the twin boundary, and the influence of these interactions on plastic deformation and mechanical properties.

Previous research on twin-dislocation interactions in Mg has focused primarily on the interactions between the $\{10\bar{1}2\}$ twin and various types of dislocations through experiments and simulations. However, there is a significant lack of studies on the interactions between the $\{10\bar{1}1\}$ twin and dislocations. Atomic-resolution experimental results [123] have proposed some possible reaction routes between the $\{10\bar{1}1\}$ twin and basal $\langle a \rangle$ mixed or prismatic $\langle c+a \rangle$ mixed dislocations. These routes suggest the production of residual dislocations of either $\mathbf{b}_{\pm 3/\pm 2}$-type or $\mathbf{b}_{\pm 1/\pm 1}$-type. Some simulations have been conducted to investigate interactions between the $\{10\bar{1}1\}$ twin and basal $\langle a \rangle$ dislocations [120,122,129], but there is a lack of research on the interactions between the $(10\bar{1}1)$ twin and $\langle c \rangle$ or $\langle c+a \rangle$ dislocations. The mechanisms, characteristics, and formation conditions of the interaction products, as well as the influence of simulation conditions on the behavior of twin-dislocation interaction for the $\{10\bar{1}1\}$ twin are not well understood. These aspects require systematic and comprehensive investigations in future research.

Additionally, most of the existing literature on twin-dislocation interactions assumes that the twin boundary is fully coherent. However, the experimental observations suggest the presence of incoherent interfaces on twin boundaries. For instance, BP or PB interfaces have been observed in the $\{10\bar{1}2\}$ twin boundary [72,158-160], and basal-pyramidal (BPy) or pyramidal-basal (PyB) interfaces in the $\{10\bar{1}1\}$ twin boundary [16]. An early simulation study [92] demonstrated that a basal $\langle a \rangle$ screw dislocation can be absorbed into a BP interface through reactions with interfacial screw dipoles. A basal $\langle a \rangle$ mixed dislocation was either attracted to or repelled from the BP interface depending on the position of its 30° Shockley partial dislocation. Furthermore, a prismatic $\langle c \rangle$ edge dislocation decomposed into an interfacial defect connected to a partial dislocation in the "twin' crystal by a basal stacking fault under zero applied stress. However, there is a lack of research on the interaction behavior between a migrating BP interface and different types of dislocations, as well as the interactions between dislocations and incoherent interfaces for the $\{10\bar{1}1\}$ twin boundary. It is therefore suggested that future work shhould focus on systematic investigating the interactions between dislocations and incoherent interfaces. This research should explore the interaction mechanisms, and products formed during these interactions, and the influence on the further migration of twin boundaries. The findings from studying the interaction behavior at incoherent interfaces can be compared with those at coherent twin boundaries, providing insights into the plastic deformation and mechanical behavior of Mg alloys.

For twin-twin interactions in Mg, it has been suggested that they can occur between two different variants of the same type of twin, such as $\{10\bar{1}2\}$ or $\{10\bar{1}1\}$. Based on the crystallographic orientation relationship, these interactions can be categorized as co-zone or non-con-zone interactions, depending on whether the interacting twins share the same a-axis or not, respectively. The co-zone and non-co-zone interactions between $\{10\bar{1}2\}$ twins have been extensively studied in previous research [39-41,131-133,135,142]. However, when it comes to $\{10\bar{1}1\}$ twin-twin interactions, only co-zone interactions have been well investigated through both experiments and simulations [136]. There is limited research on non-co-zone $\{10\bar{1}1\}$ twins interactions, with only some theoretical analyses demonstrating the geometrical relationship between two interacting variants and the possible resultant twin-twin boundary type [136]. To further our understanding of the non-co-zone $\{10\bar{1}1\}$ twin-twin interactions, it is recommended to conduct relevant simulations that explore the interaction conditions and mechanisms, examine the resulting structures, and investigate their influence on plastic deformation. Additionally, conducting experiments to validate the observations made through simulations would be valuable. By expanding research efforts in this area, we can gain insights into the behavior of non-co-zone $\{10\bar{1}1\}$ twin-twin interactions and their impact on the mechanical properties of Mg alloys.

Interactions between twins in Mg have been reported to give rise to twin-twin junctions and boundaries, double tension-tension twin and double compression-tension twin. There are other two types of structures resulted from twin-twin interactions have not been reported for Mg, which were observed in titanium [157] and associated with the sequential twinning mechanism. One is the formation of sequential twins in the parent crystal and along the primary twin boundary. Another involves sequential twins forming within the primary twin, where the primary twin boundary intersects with two other interacting twins. These two structures were observed in titanium under shock loading condition, during which complex twinning processes can take place. It remains to be seen whether similar structures can be generated in Mg under specific loading conditions. The characteristics, formation conditions, mechanisms, and the influence on plastic deformation associated with such sequential twin structures in Mg and its alloys require further examination.

It has been observed that current research in the literature primarily focuses on the interaction behavior between twins and a single type of lattice defect. Therefore, future studies are encouraged to devote more attention to interactions among twins and multiple types of lattice defects. For instance, it would be valuable to further investigate twin-dislocation interactions in the presence of solutes. Since solutes can interact with both dislocations and twin boundaries, computational simulations can be conducted from two perspectives, one involving solutes segregated to the twin boundary [14,22,51,52], and the other involving solutes segregated to the dislocation [161–164]. Considering that specific types of twin boundaries or dislocation cores process repulsive and attractive sites for particular solute atoms [66], it would be worthwhile to in-

Please cite this article as: Y. Yue, J. Wang and J.-F. Nie, Twin-solute, twin-dislocation and twin-twin interactions in magnesium, Journal of Magnesium and Alloys, https://doi.org/10.1016/j.jma.2023.07.015

troduce solute atoms with atomic sizes larger or smaller than Mg to examine the behavior of twin-solute-dislocation interactions. Similarly, research work can be undertaken to explore twin-twin-solute or twin-twin-dislocation interactions.

6. Summary

Extensive work has been conducted on investigating the interactions between twin and lattice defects, leading to significant progress in understanding twin-solute, twin-dislocation and twin-twin interactions in Mg and its alloys. The key highlights of these studies are as follows:

(1) For twin-solute interactions, a commonly considered factor based on the minimization of elastic strain is that solutes with atomic radii larger than Mg, such as Ag, Al, Ge, Ga, Li, Mn, Sn and Zn, tend to substitute into the compression sites on coherent twin boundaries. On the other hand, solutes with atomic radii smaller than Mg, such as Ca, Ce, Dy, Er, Gd, Ho, La, Lu, Nd, Pb, Pr, Sc, Sm, Y, Yb, Zr, tend to segregate into the extension sites on coherent twin boundaries. However, this criterion fails to explain certain unusual segregation phenomena. For instance, atoms of Bi, Pb, Tl and In with larger atomic size than Mg have been observed to segregate to compression sites of $\{10\bar{1}1\}$ coherent twin boundaries. This segregation is attributed to the strong chemical bonding that develops between the solute atoms and Mg atoms. Therefore, it is suggested that effect of chemical bonding should be combined with elastic strain minimization to gain a more comprehensive understanding of solute segregation behavior on coherent twin boundaries.

(2) Periodic segregation of solutes on coherent twin boundaries can have significant strengthening effect on Mg alloys by impeding the migration of twin boundary. Moreover, solute segregation on twin boundaries has an impact on the fracture toughness of Mg alloys. On one hand, fracture toughness can be improved by enhancing the cohesion of twin boundaries through strong electronic interactions between Mg atoms and segregated solutes such as Zr, Mn, Al or rate-earth element such as Y, La, Pr, Nd, Sm, Gd, Tb, Dy, Ho. On the other hand, the fracture toughness can be impaired by solute segregation that weakens the cohesion of twin boundaries. Solute segregation of elements like Li, Ca, Sn and Bi can lead to a decrease in fracture toughness. Additionally, solute segregation can reduce the damping capacity of Mg alloys, as solute atoms can stabilize the twin boundary and thereby inhibit the shrinkage and growth of deformation twin.

(3) In interactions between $\{10\bar{1}2\}$ extension twins and $\langle\ a\ \rangle$ type dislocations in Mg, a basal $\langle\ a\ \rangle$ screw dislocation can propagate directly across the twin boundary. A basal $\langle\ a\ \rangle$ mixed dislocation is either absorbed by or connected to the twin boundary under low shear stress, forming a BP or PB interface. However, under high shear stress, it transmutes across the twin boundary, forming an I_1 stacking fault (SF) connected with a single-atomic-layer-height (SALH) disconnection on the twin boundary and a Frank partial dislocation in the twin. The transmutation of two basal $\langle\ a\ \rangle$ mixed dislocations can generate a prismatic $\langle\ c+a\ \rangle$ dislocation. The resulting BP/PB disconnection, arising from interactions between $\{10\bar{1}2\}$ twin and $\langle\ a\ \rangle$ dislocations, does not hinder the migration of the twin boundary. Therefore, it is likely to be responsible for the high growth rates associated with the $\{10\bar{1}2\}$ twinning mode. The transmutation products of basal $\langle\ a\ \rangle$ mixed dislocations, such as $\langle\ c+a\ \rangle$ dislocations or I_1 basal SFs, are mostly sessile, thereby serving as a mechanism for forest hardening against other slip.

(4) Interactions between $\{10\bar{1}2\}$ twin and immobile basal-dissociated $\langle\ c\ \rangle$ or $\langle\ c+a\ \rangle$ type dislocations in Mg can also lead to the formation of BP/PB interface on the twin boundary. In addition, the transmutation of $\langle\ c\ \rangle$ or $\langle\ c+a\ \rangle$ type dislocations can generate basal $\langle\ a\ \rangle$ mixed dislocations in the twin. Basal SFs in the form of I_2, I_1 or a pair of I_1 faults are commonly observed in twin and $\langle\ c\ \rangle$ or $\langle\ c+a\ \rangle$ dislocation interactions. The resulting I_2 stacking fault is connected to $\mathbf{b_{\pm 2n/\pm 2n}}$ type disconnections on the twin boundary and bounded by a 30° Shockley partial dislocation in the twin. The resulting I_1 stacking fault is connected to a SALH disconnection and bounded by a Frank partial dislocation. A pair of I_1 faults has one end connected two separate SALH disconnections on the twin boundary and the other end bounded by a defect with a Burgers vector equal to that of a 30° Shockley. These interactions eliminate the immobile $\langle\ c\ \rangle$ or $\langle\ c+a\ \rangle$ dislocations and can generate mobile basal $\langle\ a\ \rangle$ mixed dislocations, thereby enhancing the material's plastic deformation capacity. Furthermore, basal SFs resulting from $\{10\bar{1}2\}$ twin and $\langle\ c\ \rangle$ or $\langle\ c+a\ \rangle$ interactions can act as barriers to dislocation motion on non-basal planes, leading to strain hardening.

(5) In interactions between $\{10\bar{1}1\}$ contraction twin and $\langle\ a\ \rangle$ type dislocations in Mg, a basal $\langle\ a\ \rangle$ screw dislocation decomposes into two glissile two-atomic-layer-height TDs. A basal $\langle\ a\ \rangle$ mixed dislocation dissociates into a glissile TD and a residual sessile disconnection. Alternatively, it can give rise to a pyramidal-I stacking fault that connects to a SALH disconnection on the twin boundary. The interaction between $\{10\bar{1}1\}$ twin and a prismatic $\langle\ c+a\ \rangle$ mixed dislocation can result in a one-layer step, accompanied by the emission or absoprtion of another basal $\langle\ a\ \rangle$ mixed dislocation into the twin crystal. This interaction behavior may also occur between $\{10\bar{1}1\}$ twin and a basal $\langle\ a\ \rangle$ mixed dislocation. The resulting one-layer step can further evolve into a step-SF intersection that connects with an I_1 SF, following the absorption or emission of a Frank partial dislocation. It is noteworthy that interactions between $\{10\bar{1}1\}$ twin and different types of

Please cite this article as: Y. Yue, J. Wang and J.-F. Nie, Twin-solute, twin-dislocation and twin-twin interactions in magnesium, Journal of Magnesium and Alloys, https://doi.org/10.1016/j.jma.2023.07.015

dislocations always produce glissile two-atomic-layer-height TDs. These TDs facilitate the migration of twin boundary and effectively alleviate local stress concentrations on the twin boundary, thereby retarding twin boundary cracking that is commonly associated with $\{10\bar{1}1\}$ contraction twins. In addition, these interactions generate disconnections that can further react with other lattice dislocations to release local lattice strain, thereby contributing to the plasticity of the material.

(6) $\{10\bar{1}2\}$ or $\{10\bar{1}1\}$ twin-twin interactions in Mg can occur between any two of the six variants of the twin. According to the crystallographic orientation relationship, these interactions can be categorized into co-zone and non-co-zone interactions, where two interacting variants either share or do not share the same *a*-axis. The contact and reaction of the two twin variants lead to the formation of twin-twin junctions, creating twin-twin boundaries including TTB_A (twin-twin boundary acute) and TTB_O (twin-twin boundary obtuse), and TTB_I (twin-twin boundary interface) that is parallel to the twinning plane of the encountering twin. In TTB_O or TTB_A interactions of $\{10\bar{1}2\}$ co-zone twins, the basal planes or the prismatic planes in the incoming and encountering twins bond together, forming what is referred to as BB (basal-basal) or PP (prismatic-prismatic) boundary. These boundaries consist of low-index close-packed planes, facilitating their formation. The PP boundary enable the transmission of basal slip between the intersecting twins, resulting in the formation of a basal slip band through the emission of basal dislocations. In contrast, the TTB_O or TTB_A interactions for $\{10\bar{1}2\}$ non-co-zone twins often involve high-index crystallographic planes. The preferred formation of TTB_O or TTB_A varies depending on the orientation relationship between the two variants . In all types of twin-twin interactions, boundary dislocations always form and accumulate at the twin-twin boundaries. High stress is required for the further growth and propagation of twins, giving rise to strain hardening. Moreover, the unfavorable dissociation of TTB dislocations into TDs hinders detwinning upon reverse loading, resulting cyclic hardening as the number of loading cycles increases.

(7) The $\{10\bar{1}2\}$-$\{10\bar{1}2\}$ double twin in Mg involves the formation of a secondary $\{10\bar{1}2\}$ twin inside a primary $\{10\bar{1}2\}$ twin, with the secondary twin always located at the intersections of two primary twin variants. This configuration can be referred to as an IPT-RPT-ST configuration, where IPT stands for the intersecting primary twin and RPT represents the recipient primary twin within which the secondary twin (ST) forms. Among different IPT-RPT-ST configurations, the T_1-T_2-T_{12} configuration is found to be the most favorable. In this configuration, T_1 and T_2 correspond to two $\{10\bar{1}2\}$ variants with 60° misorientation about the [0001] axis, and T_{12} is the variant of the secondary twin that forms within the primary twin T_1. The selection of variants for the IPT-RPT-ST configuration is influenced by various stresses, including pre-existing stress concentrated at the rims of the IPT and ST, back-stress within the RPT, and applied stress. Pre-existing stress plays the most dominant role in determining the variant selection, while the other two types of stresses primarily affect the growth of secondary and primary twins.

(8) The $\{10\bar{1}1\}$-$\{10\bar{1}2\}$ double twin in Mg involves the formation of a secondary $\{10\bar{1}2\}$ twin inside a primary $\{10\bar{1}1\}$ twin. The most frequently observed structure in this case is the Type I double twin structure, where the misorientation between the secondary twin and the matrix is approximately 37.5° around $\langle 1\bar{2}10\rangle$. The predominant occurrence of the Type I double twin can be attributed to several factors. First, the Type I structure has the primary and secondary twin planes closest to each other, resulting in minimal accommodation strain. Additionally, the close alignment of the twin plane and twinning direction in the Type I secondary twin with those of the primary twin allows the same local stress to support the growth of both primary and secondary twins. This facilitates the easier growth of the secondary twin in the Type I structure. Moreover, the intersection line $\langle 1\bar{2}10\rangle$ between the primary twin and Type 1 secondary twin planes has only $\langle\ a\ \rangle$ component. This makes it possible for basal $\langle\ a\ \rangle$ dislocations, which are easily activated, to dissociate into Type 1 secondary TDs at the primary twin boundary. This process further facilitates the nucleation and growth of the secondary twin. The Type I $\{10\bar{1}1\}$-$\{10\bar{1}2\}$ double twin is closely associated with the fracture failure of Mg. The double-twinned region is re-orientated for easy basal slip, leadin to enhanced localized shear deformation within the double twin. This severe localized shear promotes crack nucleation within the shear band region or along the $\{10\bar{1}1\}$-$\{10\bar{1}2\}$ twin-matrix interface, eventually causing intragranular or intergranular crack failure. The sensitivity to fracture failure associated with the $\{10\bar{1}1\}$-$\{10\bar{1}2\}$ double twin limits cold formability of Mg and its alloys.

Declaration of Competing Interest

The authors declare that they have no known competing financial interests or personal relationships that could have appeared to influence the work reported in this paper.

Acknowledgements

JFN gratefully acknowledges the support from the Australian Research Council (DP200102985 and DP180100048). This work was supported by computational resources provided by the Australian Government through National Computational Infrastructure (Raijin) and Pawsey supercomputing centre (Magnus) under the National Computational Merit Allocation Scheme (NCMAS).

References

[1] M. Easton, A. Beer, M. Barnett, C. Davies, G. Dunlop, Y. Durandet, S. Blacket, T. Hilditch, P. Beggs, JOM 60 (11) (2008) 57–62.
[2] M.K. Kulekci, Int. J. Adv. Manuf. Technol. 39 (9) (2008) 851–865.
[3] T.M. Pollock, Science 328 (5981) (2010) 986–987.
[4] C. Bettles, M. Barnett, Advances in Wrought Magnesium alloys: Fundamentals of processing, Properties and Applications, Elsevier, 2012.
[5] J.W. Christian, S. Mahajan, Prog. Mater Sci. 39 (1–2) (1995) 1–157.
[6] H. Yoshinaga, R. Horiuchi, Trans. Japan Inst. Metals 4 (1) (1963) 1–8.
[7] P. Partridge, Metallur. Rev. 12 (1) (1967) 169–194.
[8] S. Mahajan, D. Williams, Int. Metallur. Rev. 18 (2) (1973) 43–61.
[9] M. Yoo, Metall. Trans. A 12 (1981) 409–418.
[10] R. Reedhill, Trans. Am. Inst. Mining Metallur. Eng. 218 (3) (1960) 554–558.
[11] A. Crocker, Philos. Mag. 7 (83) (1962) 1901–1924.
[12] W. Hartt, R. Reed-Hill, Trans. Metall. Soc. AIME 242 (1968) 1127.
[13] J. Jain, J. Zou, C.W. Sinclair, W.J. Poole, J. Microsc. 242 (2011).
[14] J.F. Nie, Y. Zhu, J. Liu, X.Y. Fang, Science 340 (6135) (2013) 957–960.
[15] H. Zhou, G. Cheng, X. Ma, W. Xu, S. Mathaudhu, Q. Wang, Y. Zhu, Acta Mater. 95 (2015) 20–29.
[16] Y. Zhu, S. Xu, J.F. Nie, Acta Mater. 143 (2018) 1–12.
[17] X. Zhao, H. Chen, N. Wilson, Q. Liu, J.F. Nie, Nat. Commun. 10 (1) (2019) 1–7.
[18] X. Chen, L. Xiao, Z. Ding, W. Liu, Y. Zhu, X. Wu, Scr. Mater. 178 (2020) 193–197.
[19] M. Ghazisaeidi, L. Hector Jr, W. Curtin, Acta Mater. 80 (2014) 278–287.
[20] H. Somekawa, T. Tsuru, Scr. Mater. 130 (2017) 114–118.
[21] H. Somekawa, H. Watanabe, D.A. Basha, A. Singh, T. Inoue, Scr. Mater. 129 (2017) 35–38.
[22] T. Tsuru, H. Somekawa, D. Chrzan, Acta Mater. 151 (2018) 78–86.
[23] S.R. Kalidindi, A.A. Salem, R.D. Doherty, Adv. Eng. Mater. 5 (4) (2003) 229–232.
[24] M. Knezevic, A. Levinson, R. Harris, R.K. Mishra, R.D. Doherty, S.R. Kalidindi, Acta Mater. 58 (19) (2010) 6230–6242.
[25] B. Wang, R. Xin, G. Huang, Q. Liu, Mater. Sci. Eng. 534 (2012) 588–593.
[26] Y. Xin, L. Lv, H. Chen, C. He, H. Yu, Q. Liu, Mater. Sci. Eng. 662 (2016) 95–99.
[27] A. Serra, D. Bacon, R. Pond, Metall. Mater. Trans. A 33 (3) (2002) 809–812.
[28] G. Proust, C.N. Tomé, A. Jain, S.R. Agnew, Int. J. Plast. 25 (5) (2009) 861–880.
[29] C. Barrett, F. Wang, S. Agnew, H.E. Kadiri, Magnes. Technol. (2017) 147–152 Springer2017.
[30] F. Wang, K. Hazeli, K. Molodov, C. Barrett, T. Al-Samman, D. Molodov, A. Kontsos, K. Ramesh, H. El Kadiri, S. Agnew, Scr. Mater. 143 (2018) 81–85.
[31] F. Wang, C.D. Barrett, R.J. McCabe, H. El Kadiri, L. Capolungo, S.R. Agnew, Acta Mater. 165 (2019) 471–485.
[32] F. Wang, Y. Gu, R.J. McCabe, L. Capolungo, J.A. El-Awady, S.R. Agnew, Acta Mater. 195 (2020) 13–24.
[33] H. El Kadiri, A. Oppedal, J. Mech. Phys. Solids 58 (4) (2010) 613–624.
[34] F. Wang, S.R. Agnew, Int. J. Plast. 81 (2016) 63–86.
[35] N. Thompson, D. Millard XXXVIII, J. Sci. 43 (339) (1952) 422–440.
[36] M. Yoo, Trans. Metall. Soc. AIME 245 (9) (1969) 2051–2060.
[37] Y. Yue, J.F. Nie, Scr. Mater. 218 (2022) 114842.
[38] H. El Kadiri, J. Kapil, A. Oppedal, L. Hector Jr, S.R. Agnew, M. Cherkaoui, S. Vogel, Acta Mater. 61 (10) (2013) 3549–3563.
[39] Q. Yu, J. Wang, Y. Jiang, R.J. McCabe, N. Li, C.N. Tomé, Acta Mater. 77 (2014) 28–42.
[40] M. Gong, S. Xu, Y. Jiang, Y. Liu, J. Wang, Acta Mater. 159 (2018) 65–76.
[41] Q. Yu, J. Wang, Y. Jiang, R.J. McCabe, C.N. Tomé, Mater. Res. Lett. 2 (2) (2014) 82–88.
[42] Y. Xin, X. Zhou, L. Lv, Q. Liu, Mater. Sci. Eng. 606 (2014) 81–91.
[43] M. Barnett, Mater. Sci. Eng. 464 (1–2) (2007) 8–16.
[44] M. Barnett, Z. Keshavarz, A. Beer, X. Ma, Acta Mater. 56 (1) (2008) 5–15.
[45] P. Cizek, M. Barnett, Scr. Mater. 59 (9) (2008) 959–962.
[46] D. Ando, J. Koike, Y. Sutou, Acta Mater. 58 (13) (2010) 4316–4324.
[47] D. Ando, J. Koike, Y. Sutou, Mater. Sci. Eng. 600 (2014) 145–152.
[48] A. Chakkedath, C. Boehlert, JOM 67 (2015) 1748–1760.
[49] S. Niknejad, S. Esmaeili, N.Y. Zhou, Acta Mater. 102 (2016) 1–16.
[50] A. Chakkedath, T. Maiti, J. Bohlen, S. Yi, D. Letzig, P. Eisenlohr, C. Boehlert, Metall. Mater. Trans. A 49 (2018) 2441–2454.
[51] J. Zhang, Y. Dou, Y. Zheng, Scr. Mater. 80 (2014) 17–20.
[52] A. Kumar, J. Wang, C.N. Tomé, Acta Mater. 85 (2015) 144–154.
[53] C. He, Z. Li, H. Chen, N. Wilson, J.F. Nie, Nat. Commun. 12 (1) (2021) 722.
[54] Z. Pei, R. Li, J.F. Nie, J.R. Morris, Mater. Des. 165 (2019) 107574.
[55] Z. Huang, J.F. Nie, Acta Mater. 214 (2021) 117009.
[56] Y. Cui, Y. Li, Z. Wang, Q. Lei, Y. Koizumi, A. Chiba, Int. J. Plast. 99 (2017) 1–18.
[57] J. Wang, J.M. Molina-Aldareguía, J. LLorca, Acta Mater. 188 (2020) 215–227.
[58] H. Somekawa, A. Singh, T. Mukai, Philos. Mag. Lett. 89 (1) (2009) 2–10.
[59] K. Nishiyama, R. Matsui, Y. Ikeda, S. Niwa, T. Sakaguchi, J. Alloys Compd. 355 (1–2) (2003) 22–25.
[60] M.H. Tsai, M.S. Chen, L.H. Lin, M.H. Lin, C.Z. Wu, K.L. Ou, C.H. Yu, J. Alloys Compd. 509 (3) (2011) 813–819.
[61] Y. Cui, Y. Li, S. Sun, H. Bian, H. Huang, Z. Wang, Y. Koizumi, A. Chiba, Scr. Mater. 101 (2015) 8–11.
[62] H. Watanabe, Y. Sasakura, N. Ikeo, T. Mukai, J. Alloys Compd. 626 (2015) 60–64.
[63] M. Ghazisaeidi, D. Trinkle, Acta Mater. 76 (2014) 82–86.
[64] W.J. Joost, S. Ankem, M.M. Kuklja, Acta Mater. 105 (2016) 44–51.
[65] M. Hooshmand, C. Niu, D. Trinkle, M. Ghazisaeidi, Acta Mater. 156 (2018) 11–19.
[66] M. Hooshmand, M. Ghazisaeidi, Acta Mater. 188 (2020) 711–719.
[67] A. Akhtar, Metall. Trans. A 6 (1975) 1105–1113.
[68] M. Bevis, A. Crocker, Proc. R. Soc. London. A. Math. Phys. Sci. 313 (1969) (1515) 509–529.
[69] A. Serra, D. Bacon, Philos. Mag. A 73 (2) (1996) 333–343.
[70] P.M. Anderson, J.P. Hirth, J. Lothe, Theory of Dislocations, Cambridge University Press, 2017.
[71] B. Li, E. Ma, Phys. Rev. Lett. 103 (3) (2009) 035503.
[72] X. Zhang, B. Li, X. Wu, Y. Zhu, Q. Ma, Q. Liu, P. Wang, M. Horstemeyer, Scr. Mater. 67 (10) (2012) 862–865.
[73] B. Li, X. Zhang, Scr. Mater. 71 (2014) 45–48.
[74] B. Li, X. Zhang, Scr. Mater. 125 (2016) 73–79.
[75] X. Zhang, B. Li, Q. Sun, Scr. Mater. 159 (2019) 133–136.
[76] J. Wang, L. Liu, C. Tomé, S. Mao, S. Gong, Mater. Res. Lett. 1 (2) (2013) 81–88.
[77] B. Xu, L. Capolungo, D. Rodney, Scr. Mater. 68 (11) (2013) 901–904.
[78] A. Ostapovets, R. Gröger, Modell. Simul. Mater. Sci. Eng. 22 (2) (2014) 025015.
[79] A. Ostapovets, A. Serra, Metals (Basel) 10 (9) (2020) 1134.
[80] B.Y. Liu, J. Wang, B. Li, L. Lu, X.Y. Zhang, Z.W. Shan, J. Li, C.L. Jia, J. Sun, E. Ma, Nat. Commun. 5 (1) (2014) 1–6.
[81] J. Hirth, J. Wang, C. Tomé, Prog. Mater Sci. 83 (2016) 417–471.
[82] M. Gong, J.P. Hirth, Y. Liu, Y. Shen, J. Wang, Mater. Res. Lett. 5 (7) (2017) 449–464.
[83] L. Jiang, M. Gong, J. Wang, Z. Pan, X. Wang, D. Zhang, Y.M. Wang, J. Ciston, A.M. Minor, M. Xu, Nat. Commun. 13 (1) (2022) 20.
[84] C.D. Barrett, H. El Kadiri, Acta Mater. 63 (2014) 1–15.
[85] Z. Wu, W. Curtin, Nature 526 (7571) (2015) 62–67.
[86] Z. Wu, W. Curtin, Scr. Mater. 116 (2016) 104–107.
[87] H. Fan, J. Tang, X. Tian, Q. Wang, X. Tian, J.A. El-Awady, Scr. Mater. 135 (2017) 37–40.
[88] J. Hirth, R. Pond, Acta Mater. 44 (12) (1996) 4749–4763.
[89] R. Pond, A. Serra, D. Bacon, Acta Mater. 47 (5) (1999) 1441–1453.
[90] R. Pond, S. Celotto, Metall. Mater. Trans. A 33 (3) (2002) 801–807.

Please cite this article as: Y. Yue, J. Wang and J.-F. Nie, Twin-solute, twin-dislocation and twin-twin interactions in magnesium, Journal of Magnesium and Alloys, https://doi.org/10.1016/j.jma.2023.07.015

[91] A. Serra, D. Bacon, R. Pond, Acta Metall. 36 (12) (1988) 3183–3203.
[92] A. Serra, D. Bacon, R. Pond, Acta Mater. 47 (5) (1999) 1425–1439.
[93] A. Serra, D.J. Bacon, Philos. Mag. 90 (7–8) (2010) 845–861.
[94] A. Serra, R. Pond, D. Bacon, Acta Metall. Mater. 39 (7) (1991) 1469–1480.
[95] D. Vallance, M. Bevis, Scr. Metall. 4 (9) (1970) 681–684.
[96] S. Lay, G. Nouet, Philos. Mag. A 70 (6) (1994) 1027–1044.
[97] A. Serra, D. Bacon, Acta Metall. Mater. 43 (12) (1995) 4465–4481.
[98] M. Yuasa, K. Masunaga, M. Mabuchi, Y. Chino, Philos. Mag. 94 (3) (2014) 285–305.
[99] K.D. Molodov, T. Al-Samman, D.A. Molodov, Acta Mater. 124 (2017) 397–409.
[100] M. Gong, G. Liu, J. Wang, L. Capolungo, C.N. Tomé, Acta Mater. 155 (2018) 187–198.
[101] J. Dickson, C. Robin, Mater. Sci. Eng. 11 (5) (1973) 299–302.
[102] M. Hyong Yoo, C.T. Wei, Philos. Mag. 14 (129) (1966) 573–587.
[103] D. Tomsett, M. Bevis, Philos. Mag. 19 (157) (1969) 129–140.
[104] J. Wang, I. Beyerlein, C. Tomé, Int. J. Plast. 56 (2014) 156–172.
[105] J. Wang, Q. Yu, Y. Jiang, I.J. Beyerlein, JOM 66 (1) (2014) 95–101.
[106] H. El Kadiri, C.D. Barrett, J. Wang, C.N. Tomé, Acta Mater. 85 (2015) 354–361.
[107] P. Chen, J. Ombogo, B. Li, Acta Mater. 186 (2020) 291–307.
[108] M. Niewczas, Acta Mater. 58 (17) (2010) 5848–5857.
[109] M.H. Yoo, C.T. Wei, J. Appl. Phys. 38 (11) (1967) 4317–4322.
[110] A. Ostapovets, A. Serra, R.C. Pond, Scr. Mater. 172 (2019) 149–153.
[111] Y. Yue, Y. Zhang, J. Nie, Scr. Mater. 209 (2022) 114407.
[112] X. Zhou, H. Su, H. Ye, Z. Yang, Acta Mater. 217 (2021) 117170.
[113] J. Han, X. Su, Z.H. Jin, Y. Zhu, Scr. Mater. 64 (8) (2011) 693–696.
[114] B. Li, P. Yan, M. Sui, E. Ma, Acta Mater. 58 (1) (2010) 173–179.
[115] X. Zhang, B. Li, Q. Liu, Acta Mater. 90 (2015) 140–150.
[116] Q. Sun, X. Zhang, Y. Shu, L. Tan, Q. Liu, Mater. Lett. 185 (2016) 355–358.
[117] S. Zhu, S.P. Ringer, Acta Mater. 144 (2018) 365–375.
[118] C. He, Y. Zhang, C. Liu, Y. Yue, H. Chen, J. Nie, Acta Mater. 188 (2020) 328–343.
[119] P. Chen, F. Wang, B. Li, Acta Mater. 164 (2019) 440–453.
[120] T. Yoshida, M. Yuasa, M. Mabuchi, Y. Chino, J. Appl. Phys. 118 (3) (2015) 034304.
[121] M. Hooshmand, M. Mills, M. Ghazisaeidi, Mater. Sci. Eng. 25 (4) (2017) 045003.
[122] J. Wang, I. Beyerlein, J. Hirth, Modell. Simul. Mater. Sci. Eng. 20 (2) (2012) 024001.
[123] H. Su, X. Zhou, M. Zhang, S. Zheng, H. Ye, Z. Yang, Acta Mater. 206 (2021) 116622.
[124] R. Pond, W. Bollmann, Philosoph. Trans. R. Soc. London. Series A, Math. Phys. Sci. 292 (1395) (1979) 449–472.
[125] R. Pond, D. Vlachavas, Proc. R. Soc. London. A. Math. Phys. Sci. 386 (1790) (1983) 95–143.
[126] R. Pond, Philos. Mag. A 63 (5) (1991) 973–985.
[127] R. Pond, J. Hirth, Elsevier (1994) 287–365.
[128] J. Hirth, R. Pond, R. Hoagland, X.-Y. Liu, J. Wang, Prog. Mater Sci. 58 (5) (2013) 749–823.
[129] Z. Li, J. Wang, W. Liu, Comput. Mater. Sci. 155 (2018) 11–16.
[130] J. Koike, Metall. Mater. Trans. A 36 (7) (2005) 1689–1696.
[131] B. Morrow, E.K. Cerreta, R.J. Mccabe, C.N. Tomé, Mater. Sci. Eng. A-struct. Mater. Properties Microstruct. Process. 613 (2014) 365–371.
[132] Q. Sun, X. Zhang, Y. Ren, L. Tan, J. Tu, Mater. Charact. 109 (2015) 160–163.
[133] Q. Sun, A. Ostapovets, X.Y. Zhang, L. Tan, Q. Liu, Philos. Mag. 98 (2018) 741–751.
[134] H. Chen, T. Liu, S. Xiang, Y. Liang, J. Alloys Compd. 690 (2017) 376–380.
[135] K. Dang, C.N. Tomé, L. Capolungo, Scr. Mater. (2021).
[136] Q. Peng, Y. Sun, J. Wang, Q. Zu, M. Yang, H. Fu, Acta Mater. 192 (2020) 60–66.
[137] B. Zhou, M. Sui, J. Mater. Sci. Technol. (2019).
[138] R. Xin, C. Guo, J.J. Jonas, G. Chen, Q. Liu, Mater. Sci. Eng. A-struct. Mater. Properties Microstruct. Process. 700 (2017) 226–233.
[139] L. Tan, X.Y. Zhang, T. Xia, Q. Sun, G.j. Huang, R. Xin, Q. Liu, Mater. Sci. Eng. A-struct. Mater. Properties Microstruct. Process. 711 (2018) 205–211.
[140] H. Liu, F. Lin, P.Y. Liu, Y. Yue, K.S. Shin, L.M. Peng, L. Delannay, J.F. Nie, N. Moelans, Acta Mater. (2021).
[141] Z.Z. Shi, J. Xu, J. Yu, X.F. Liu, J. Alloys Compd. (2018).
[142] E. Roberts, P.G. Partridge, Acta Metall. 14 (1966) 513–527.
[143] L. Tan, X.Y. Zhang, T. Xia, G.J. Huang, Q. Liu, Rare Met. 39 (2) (2020) 162–168.
[144] I.J. Beyerlein, J. Wang, M.R. Barnett, C.N. Tomé, Proc. R. Soc. A 468 (2012) 1496–1520.
[145] Ė. Martin, L. Capolungo, L. Jiang, J.J. Jonas, Acta Mater. 58 (2010) 3970–3983.
[146] R. Aghababaei, S.P. Joshi, Acta Mater. 69 (2014) 326–342.
[147] E. Anderson, D. Jillson, S. Dunbar, Trans. Am. Inst. Mining Metallur. Eng. 197 (9) (1953) 1191–1197.
[148] F. Xu, X. Zhang, H. Ni, Q. Liu, Mater. Sci. Eng. 541 (2012) 190–195.
[149] Y. Ren, X. Zhang, T. Xia, Q. Sun, Q. Liu, Mater. Des. 126 (2017) 123–134.
[150] H. Li, X. Xu, Q. Sun, X. Zhang, X. Fang, M. Zhu, J. Alloys Compd. 788 (2019) 1137–1145.
[151] S. Xu, M. Gong, Y. Jiang, C. Schuman, J.-S. Lecomte, J. Wang, Acta Mater. (2018).
[152] S. Godet, L. Jiang, A.A. Luo, J.J. Jonas, Scr. Mater. 55 (2006) 1055–1058.
[153] J.J. Jonas, S. Mu, T. Al-Samman, G. Gottstein, L. Jiang, Ė. Martin, Acta Mater. 59 (2011) 2046–2056.
[154] C. Gu, L.S. Toth, M. Hoffman, Acta Mater. 62 (2014) 212–224.
[155] S. Xu, M. Gong, C. Schuman, J.-S. Lecomte, X. Xie, J. Wang, Acta Mater. 132 (2017) 57–68.
[156] Z.Z. Shi, Y. Zhang, F. Wagner, P.A. Juan, S. Berbenni, L. Capolungo, J.S. Lecomte, T. Richeton, Acta Mater. 83 (2015) 17–28.
[157] S. Xu, P. Zhou, G. Liu, D.W. Xiao, M. Gong, J. Wang, Acta Mater. (2019).
[158] Q. Sun, X. Zhang, Y. Ren, J. Tu, Q. Liu, Scr. Mater. 90 (2014) 41–44.
[159] J. Tu, X. Zhang, Y. Ren, Q. Sun, Q. Liu, Mater. Charact. 106 (2015) 240–244.
[160] J. Tu, X. Zhang, Z. Zhou, C. Huang, Mater. Charact. 110 (2015) 39–43.
[161] F. Nabarro, 75, 1948, p. 590.
[162] S. Hu, L. Chen, Acta Mater. 49 (3) (2001) 463–472.
[163] M.K. Miller, J. Mater. Sci. 41 (23) (2006) 7808–7813.
[164] W. Hu, Z. Yang, H. Ye, Scr. Mater. 117 (2016) 77–80.

Please cite this article as: Y. Yue, J. Wang and J.-F. Nie, Twin-solute, twin-dislocation and twin-twin interactions in magnesium, Journal of Magnesium and Alloys, https://doi.org/10.1016/j.jma.2023.07.015